January 2020

Thermal Atomic Layer Deposition Of Silver Metal Films: Synthesis And Characterization Of Thermally Stable Silver Metal Precursors

Harshani Jayabahu Arachchilage
Wayne State University

THERMAL ATOMIC LAYER DEPOSITION OF SILVER METAL FILMS: SYNTHESIS AND CHARACTERIZATION OF THERMALLY STABLE SILVER METAL PRECURSORS

by

HARSHANI JAYABAHU ARACHCHILAGE

DISSERTATION

Submitted to the Graduate School

of Wayne State University,

Detroit, Michigan

in partial fulfillment of the requirements

for the degree of

DOCTOR OF PHILOSOPHY

2020

MAJOR: CHEMISTRY (Inorganic)

Approved By:

_____

Advisor Date

_____

_____

_____

_____

DEDICATION

I dedicate this dissertation to my beautiful daughter Nuvini Haseli Perera.

ACKNOWLEDGMENTS

Pursuing a Ph.D. is one of the most challenging tasks I have encountered in my life. It has been a challenging yet rewarding journey for me to make my dreams come true. I acknowledge those who gave me this strength and support to come so far. Firstly, I would like to thank Professor Charles H. Winter for giving me the wonderful opportunity to complete my Ph.D. thesis under his supervision, and it is truly an honor. I would like to express my sincere gratitude for his continuous support, patience, motivation, and immense knowledge.

Besides my advisor, I would like to thank the rest of my thesis committee: Professor Stanislav Groysman, Professor Young-Hoon Ahn, and Dr. Thomas Knisley for their comments, guidance, and helpful suggestions on my thesis. A very special thank goes to Dr. Thomas Knisley from Applied Materials for his continuous support and encouragement.

This project would never have been possible without the support and guidance of various people in the Department of Chemistry at Wayne State University. I thank the personnel of the Lumigen Instrument Center, Wayne State University Grid, Science and Engineering Library, and Science Storeroom for their technical assistance, Dr. Cassie Ward, Mr. Dennis Anderson, Dr. Zhi "Mike" Mei, Dr. Sameera Perera, Dr. Bashar Ksebati, Dr. Phil Martin, and Nestor Ocampo. Thank you to Jackie Baldyga, Melissa Rochon, and the administrative staff for their continuous support. A very special thank goes to my past and present group members for their friendship. Dr. Wathsala Waduge and Dr. Kyle Blakeney are gratefully acknowledged for sharing their time and expertise with me.

I would like to thank my parents: your devotion, unconditional love and support, patience, optimism, and advice was more valuable than you could ever imagine. I would like to give my endless appreciation to my husband, Nuwan Chinthaka, who is always with me and gives strength

and love to succeed in my journey. Lastly, I would like to mention my former advisors, Professor Richard E. Norman and Professor Janitha A. Liyanage, for being wonderful mentors to guide me this far.

TABLE OF CONTENTS

LIST OF TABLES

LIST OF FIGURES

LIST OF CHARTS

LIST OF ABBREVIATIONS

ABBREVIATION	LONG FORM
ALD	Atomic Layer Deposition
CVD	Chemical Vapor Deposition
fod	1,1,1,2,2,3,3-heptafluoro-7,7-dimethyloctane-4,6-dione
DTA	Differential Thermal Analysis
hfac	1,1,1,5,5,5-hexafluoroacetylacetonato
IR	Infrared Spectroscopy
NHC	N-Heterocyclic carbene
NMR	Nuclear Magnetic Resonance
Pta	1,1,1-trifluoro-5,5-dimethylhexane-2,4-dione
PEALD	Plasma-Enhanced Atomic Layer Deposition
PVD	Physical Vapor Deposition
Pz	Pyrazole
SEM	Scanning Electron Microscopy
TGA	Thermogravimetric Analysis
thd	2,2,6,6-tetramethylheptane-3,5-dionato
tta	1-(2-thienoyl)-3,3,3-trifluoroacetonate
XPS	X-Ray Photoelectron Spectroscopy

CHAPTER 1: INTRODUCTION

1.1 Miniaturization of Microelectronic Devices

In microelectronics devices, thin film growth is an essential step in manufacturing. The first transistor was invented at Bell Laboratories on December 23, 1947.[1] Since then, the transistor has been identified as a key component of modern electronic devices. In the early days of the integrated circuits, Moore predicted that the number of transistors in a single device should double every 18-24 months.[2] The exponential growth of transistor density in microelectronic architecture came to be known as "Moore's Law," which describes the drive towards smaller, faster, and more powerful devices. The *International Technology Roadmap for Semiconductors* (ITRS) predicts transistor technology is shrinking in feature size to 7 nm in 2018.[3] When moving to smaller feature sizes, the materials layer thicknesses are also getting thinner and aspect ratios are increasing. The continuing reduction of the feature dimensions and increasing aspect ratios create limitations in available film deposition techniques and processes. Traditional materials may not maintain optimal device performance at reduced dimensions, and also traditional film deposition techniques may not provide the required thickness control in aspect ratio features. These problems can be addressed by finding high-performance materials and new deposition techniques. Smooth, pinhole free, and highly pure films are required to enhance the performance and efficiency of current devices.[4-6]

In the microelectronics industry, thin metal films are used as conductors in applications such as transistor gates, electrodes, and interconnects, while metal nitrides and metal oxides are used as barriers and high-k dielectrics, respectively. The growth of thin metal films is required in metal-oxide-semiconductor field-effect transistors (MOSFETs) used in microelectronics devices (Figure 1). MOSFETs are fabricated on a silicon substrate and consist of three terminals, named the source, drain, and gate. Thin silicide films of Ni and Co are used as source and drain contact

materials. The NiSi and CoSi are manufactured by thermal annealing of Ni or Co films deposited on silicon contacts.[7-9] The gate is made of highly conductive material and is separated from the semiconductor by a dielectric. The gate dielectric acts as an insulating layer that controls the current flow between the source and drain of the transistor. Silicon dioxide (SiO_2) is traditionally used as the gate dielectric material in the industry. When the transistor size is reduced, quantum tunneling effect prevents effective charge separation. In reduced dimensions, SiO_2 shows poor device performance due to the increased leakage current. Metal oxides such as rare earth oxides,[10-11] HfO_2, ZrO_2, and TiO_2[12] are considered as replacements for SiO_2.

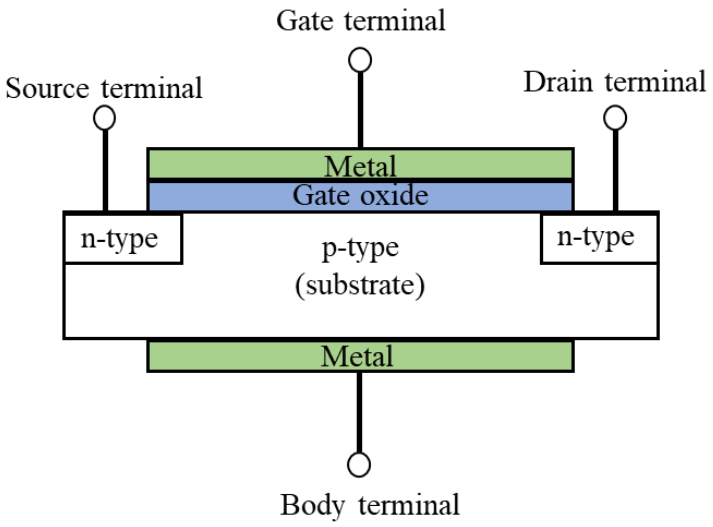

Figure 1. Cross-sectional view of MOSFET structure.

Cu plays a key role as the primary interconnect material in the development of microelectronics due to its low resistivity and better electromigration resistance compared to Al.[13] However, it is difficult to make a continuous Cu layer on the silicon surface. Therefore, seed layer deposition is a crucial step for Cu metallization. Metal seed layers, including Co, Cr, and Ru, have been explored.[14] Additionally, copper diffuses into Si and SiO_2 substrates. Therefore, a diffusion barrier layer is required between copper and the insulating substrate to stop the diffusion of Cu

into the Si substrate. This barrier layer must be unreactive towards both copper and Si and must show excellent adhesion to both copper and Si. Metal nitride films such as TaN and WN_x (x = 0.5-1) have been studied as advanced barrier materials.[15-20] Nevertheless, very thin films (≤ 5 nm) of these metal nitride layers do not act as functional Cu diffusion barriers.[13,21-22] Transition metal thin films of Mn,[23-24] Ru,[25] Cr, and others have developed as alternative barrier materials.[26] A Mn-containing amorphous oxide ($MnSi_xO_y$) layer between the SiO_2 and Cu layers has been prepared by annealing of Cu-Mn alloy deposited on SiO_2 substrates at 450 °C (Figure 2).[27] This self-forming $MnSi_xO_y$ layer functioned as a Cu diffusion barrier at 450 °C up to 100 h.[27] More recently, Winter and coworkers developed a low temperature thermal ALD process for Cu/Mn alloy deposition.[28] This development leads to the formation of conformal and ultrathin Mn-based Cu diffusion barriers.

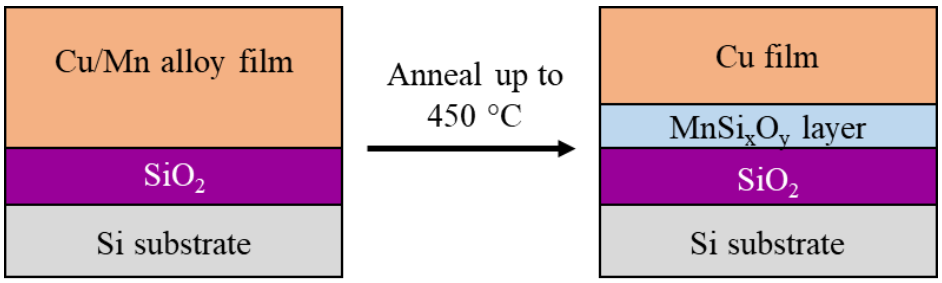

Figure 2. Growth of the $MnSi_xO_y$ diffusion barrier.

1.2 Film Deposition Methods

Three main types of vapor deposition techniques are used in the manufacture of current electronic devices, including physical vapor deposition (PVD), chemical vapor deposition (CVD), and atomic layer deposition (ALD). Traditional film deposition methods, such as PVD[29] and CVD,[30-32] are well established and less expensive than ALD. However, when material thicknesses

are reduced in current microelectronics, PVD and CVD do not offer conformal thin films due to line-of-sight nature and uncontrollable film thicknesses, respectively. Conformality is the ability to deposit material uniformly in high aspect ratio features (Figure 3(b)). Conformal films offer equal thickness and compositions inside the 3D features (trenches and vias). PVD and CVD techniques can not approach the conformality achieved by ALD in high aspect ratio features.[5,33-37]

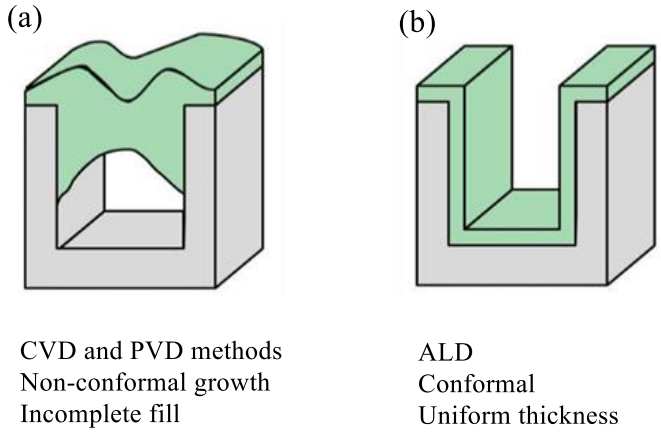

Figure 3. Comparison of film coverage and conformality by (a) CVD, PVD, (b) ALD processes.

1.2.1 Physical Vapor Deposition (PVD)

PVD comprises several vapor deposition techniques, including evaporation, laser ablation-deposition, vacuum-arc deposition, and sputter deposition. In PVD, surface atoms are removed from a source material by thermal heating or high energy particle bombardment using electrons, atoms, or ions in a vacuum and are deposited on the substrate surface.[29] In evaporation, the heating of the material provides sufficient energy for the atoms to enter the vapor phase (Figure 4 (a)). Evaporation can be categorized into two classes: (1) quasi-equilibrium and (2) non-equilibrium.[29] In quasi-equilibrium, liquid material has an equilibrium with its vapor in a closed heated cell, while in the non-equilibrium case, liquid material is evaporated into an open vessel. In both cases, evaporated material is directly transferred to a cooled substrate where the deposition occurs. In

sputtering, energetic particles such as an inert gas ion, neutral atom, molecule, or even photons impact the target (Figure 4 (b)).[29,38] The near-surface atoms are dislodged by these collisions and get sufficient energy to overcome surface binding energies and are emitted from the target.

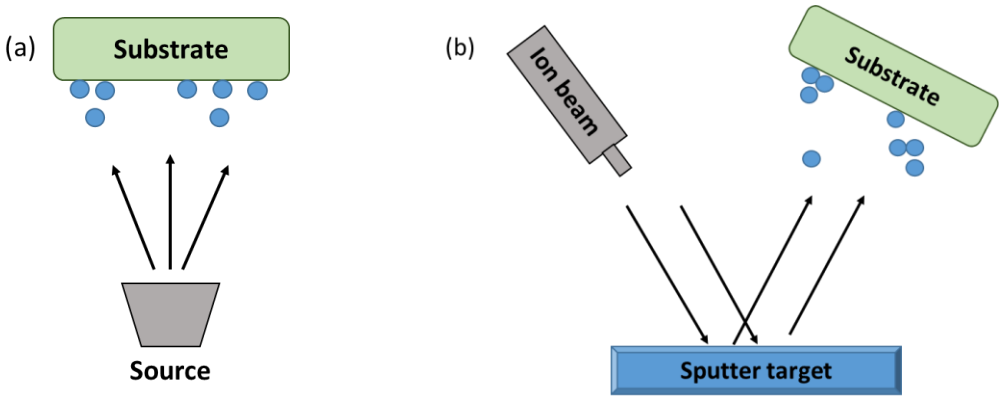

Figure 4. The film deposited by (a) evaporative PVD, (b) sputter PVD.

PVD techniques offer high deposition rates. Due to the simple methodology and low cost of PVD technologies, they are widely used in manufacturing applications. However, these techniques are unable to provide conformal, controlled thickness films in high aspect ratio features due to the intrinsically directional nature of PVD, which limits the number of atoms that can enter a shaped feature.[4,37-39] The lower probability of collisions of in-flight atoms with other gas atoms in evaporative PVD leads to directional and columnar type growth.[29] Nevertheless, sputter PVD occurs at increased gas pressure and allows a non-directional growth. At high pressure due to the collisions, scatter of in-flight atoms offers sufficient step-coverage in 3D features.[29] However, many PVD processes do not provide conformal coverage in high aspect ratio features (> 10:1) in advanced microelectronics devices.[29]

1.2.2 Chemical Vapor Deposition (CVD)

CVD is used to produce most metals, many nonmetallic elements such as carbon, silicon, as well as their compounds such as carbides, nitrides, and oxides.[30-32,38,40-43] In CVD, gaseous precursors are introduced to a heated reaction chamber. Inert gases such as nitrogen, argon, or helium are used as carrier gasses to deliver the precursors to the reaction chamber.[32] Precursors will undergo complex reactions such as oxidation, reduction, and decomposition in the vapor phase or on the substrate surface to make the film material (Figure 5). In some cases, CVD processes are more economical than PVD processes and give high deposition rates and thick coatings as well.

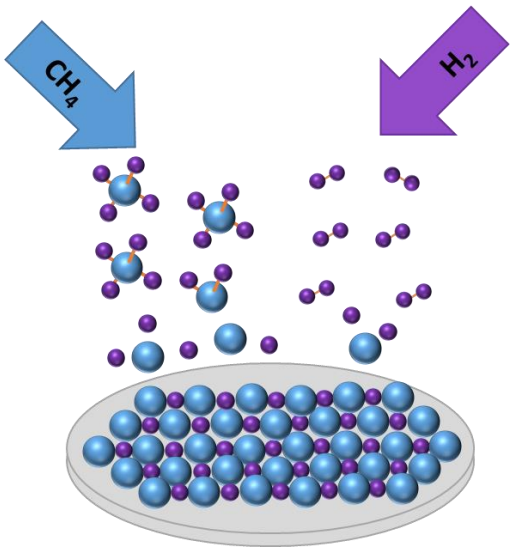

Figure 5. Film growth by CVD.

The CVD precursors must fulfill certain requirements including, volatility, reactivity, and thermal stability at the desired delivery temperatures to obtain proper film growth.[32] Precursors should be sufficiently volatile to vaporize at relatively low temperatures.[32] These precursors must be adequately reactive on the substrate surface. However, precursors could also react in the vapor phase, other than reacting only on the substrate. By decreasing the reaction chamber pressure, gas

phase reactions can be minimized. Reaction chambers with low pressures decrease collisions between gaseous molecules, which reduce gas phase reactions. CVD reactor chambers are typically heated up to >600 °C, and a major disadvantage is that many substrates are not thermally stable at these temperatures.[40] CVD methods are often inappropriate for conformal coatings of high aspect ratio features because thermal decomposition of the precursors often results in nonconformal growth and impurity incorporation to the films.

In the semiconductor industry, PVD- and CVD-based techniques are used to deposit thin film materials. However, it is challenging to obtain conformal coatings in high aspect ratio features using these techniques. A deposition technique that can deposit conformal thin films in high aspect ratio features is required for current microelectronics devices. The ALD technique offers controlled thicknesses and conformal film growth in high aspect ratio features.

1.2.3 Atomic Layer Deposition (ALD)

ALD was developed by Suntola and Antson in the 1970s, was originally introduced to the world as atomic layer epitaxy (ALE).[4,44] The ALD method was first developed to deposit films in thin film electroluminescent (TFEL) flat-panel displays.[45] ALD has developed as a powerful technique for many industrial and research applications because of its reproducibility, exceptional conformality in high aspect ratio features, thickness control at the Angstrom level, and tunable film compositions.[4-6,33-37,46] ALD controls the film thickness and provides conformal film growth due to its sequential and self-limiting reactions.[6,37,46] Miniaturization of microelectronics devices has produced high aspect ratio features that need to be coated uniformly. ALD has achieved the highest conformality in high aspect ratio features. Therefore, ALD is an attractive technique to use in the microelectronics industry.

In contrast to CVD, gas phase reactions in ALD are eliminated by introducing precursors separately to the reaction chamber. ALD follows four steps in a growth cycle: (1) metal precursor is introduced to the substrate surface, (2) reaction chamber is purged with inert gas to remove extra precursor molecules and reaction byproducts, (3) A gaseous stream of the co-reactant is pulsed into the reactor and allowed to react with the adsorbed metal precursor, and (4) reaction chamber is purged with inert gas to remove volatile byproducts. This stepwise process is repeated until the desired film thickness is obtained.[4] The deposition of Al_2O_3 from trimethylaluminum (TMA) and water process is illustrated in Figure 6. In the first step of the Al_2O_3 process, TMA reacts with the Si-OH groups on the surface. Once all of these surface reactive sites are consumed, TMA does not react further with the surface. This process is called self-limited growth. In the second step, an N_2 gas purge removes excess TMA precursor and reaction byproducts from the reaction chamber. The third step is exposure of the co-reactant (water) to react with the Al-CH_3 terminated surface and form desired film material. Once all of the Al-CH_3 sites undergo protonolysis with water, water does not react further with the surface. This reaction is also self-limited. In the fourth step, excess water and reaction byproducts are removed from the chamber by introducing a purge with N_2 gas.

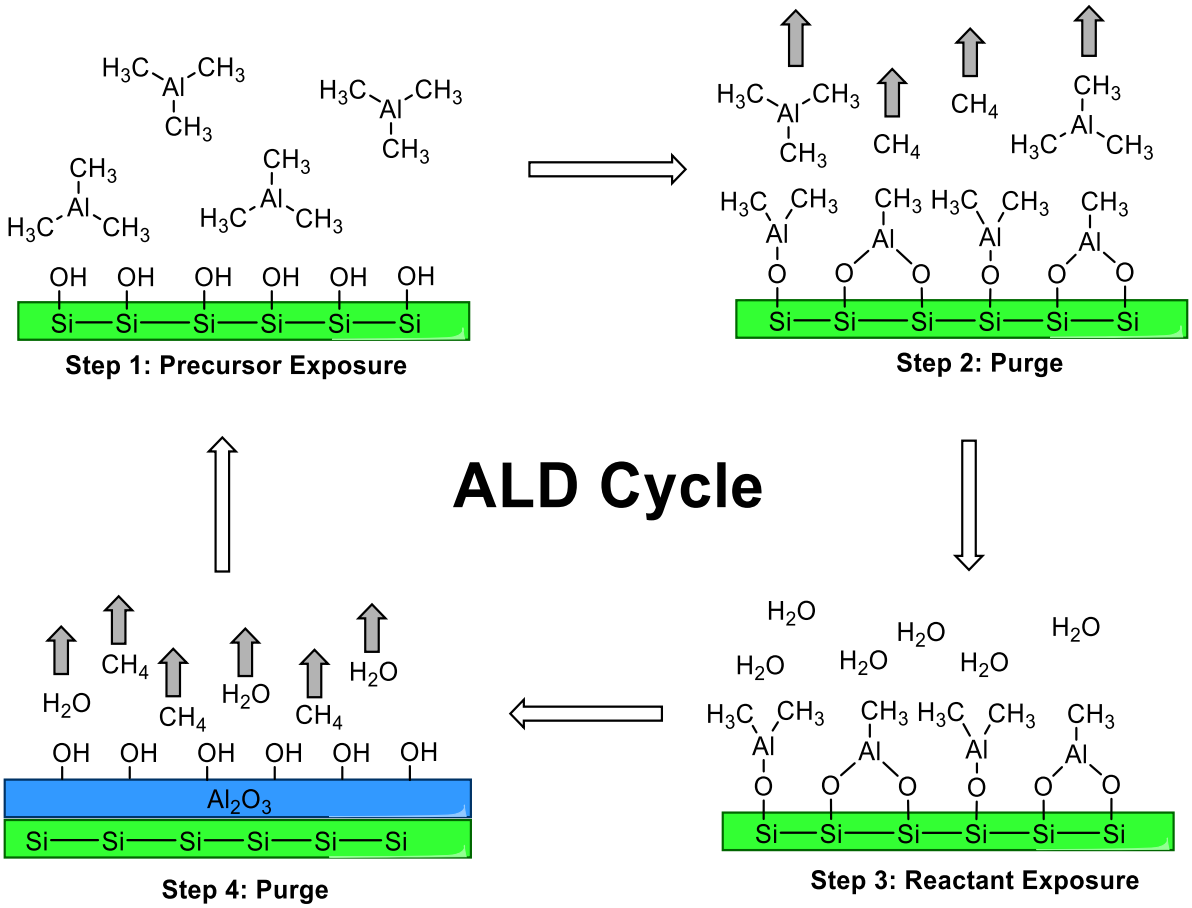

Figure 6. ALD cycle for the deposition of Al_2O_3 from TMA and water.

Self-limiting growth behavior of the precursors can be studied by changing the precursor pulse lengths while keeping all other parameters constant. In ALD, the precursors will react or adsorb with all of the available reactive sites on the surface. Once all the active sites are saturated, excess precursors will not participate in further film growth.[4-6,33-37,47] Therefore, the growth rate is independent of the precursor pulse length once the minimum saturative precursor dose is introduced, as shown in Figure 7.

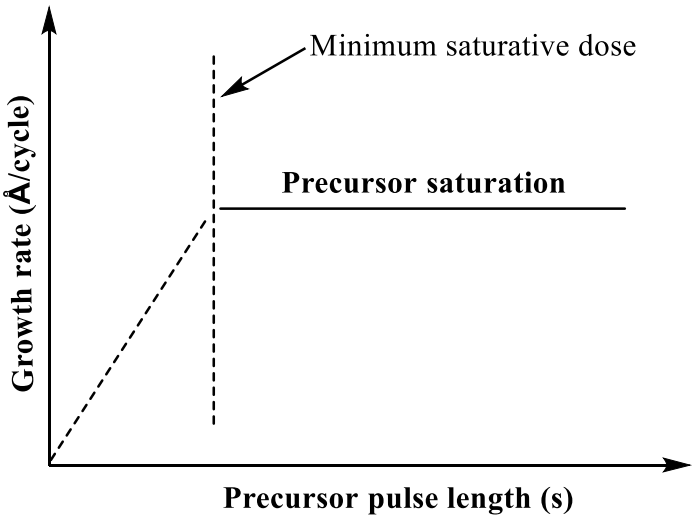

Figure 7. Plot of growth rate versus precursor pulse length.

Once the saturative doses of precursors are determined, the deposition temperature can be varied to determine the temperature dependence of the growth process. Most ALD processes show a constant growth rate over a temperature range in a plot of growth rate versus deposition temperature. This temperature region is called the "ALD window" (Figure 8).[4,37,46,`48-49] At temperatures below the ALD window, (1) the growth rate can be lower due to insufficient reactivity between precursor and the growth surface or second precursor with the first precursor, or (2) the growth rate can be higher due to precursor condensation. At temperatures above the ALD window, (3) the growth rate can be lower due to thermal desorption of the precursors or loss of reactive sites, or (4) higher growth rate may result due to CVD-type growth by precursor self-decomposition. Having a constant growth rate over a broad temperature range is advantageous. In manufacturing, temperature fluctuations during a process can be tolerated by having a large ALD window. Therefore, the process is intrinsically stable, repeatable, and easier to control. The wide ALD window is also essential in coating large areas because constant temperature supply is a challenge.

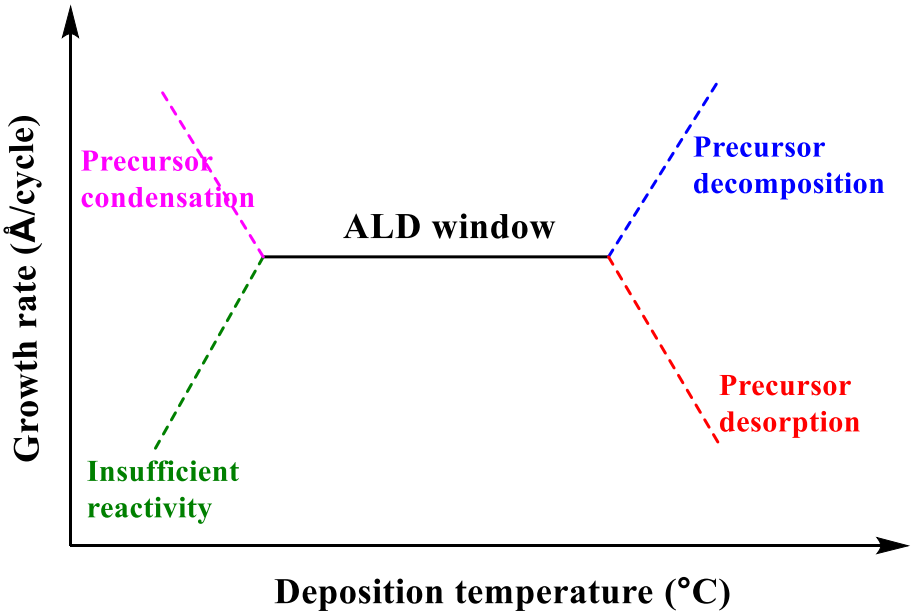

Figure 8. Plot of growth rate versus substrate temperature.

Due to the self-limited growth of ALD, practical advantages such as large area uniformity, excellent conformality, pinhole free films, low deposition temperatures with suitable precursor chemistry, and accurate and simple thickness controllability are obtained. Composition control is another prominent advantage of ALD. Materials such as zinc tin oxide (ZTO),[50] $SrTiO_3$,[51] and others[52] can be deposited and compositionally controlled by introducing multiple ALD processes named "supercycles." However, there are some disadvantages associated with ALD processes. At low deposition temperatures, poorly crystalline or amorphous films may result. Crystalline films with a specific phase strongly affect the properties of oxide films.[53] This crystalline structure often depends on the temperature. Another drawback is that low growth rates lead to long deposition times for ALD processes. Nonetheless, ALD is a well-developed technique used in the semiconductor industry to deposit high-quality thin films even on complex substrates.

Thermal ALD and plasma-enhanced ALD are considered as two different classes of ALD. In thermal ALD, heat is used to drive the reactions thermodynamically. However, in plasma ALD,

high energy radicals are used. Plasma sources such as N_2, NH_3, O_2, H_2, and H_2O vapor have been used in meal depositions. Plasma-enhanced ALD is used to deposit many different materials that are difficult to deposit using thermal ALD.[54] Atomic hydrogen generated in plasma H_2 is a very powerful reducing agent, which has been used to deposit difficult metals such as Ta and Ti by ALD.[39,55-56] Ta and Ti have negative electrochemical potentials, and it is a challenge to grow these metal films by thermal ALD. Usually, highly reactive plasma sources can offer low temperature depositions and high growth rates in plasma ALD processes. However, due to radical recombination reactions, reactive species tend to recombine on the walls of high aspect ratio features, leading to loss of the reducing hydrogen atoms. This loss can lead to non-conformal growth on the sidewalls and at the bottom of high aspect ratio features.[37,54] Plasma ALD can also result in rough films due to the substrate and growing film being damaged by highly reactive plasma species. Therefore thermal ALD is preferred over plasma ALD for many applications.

1.3 ALD Precursor Requirements

Precursors play a key role in ALD. ALD precursors should possess sufficient volatility, thermal stability at the desired deposition temperatures, and high chemical reactivity towards the second reactant in order to deposit the desired thin film material.[4,37] Generally, ALD precursors can be solids, liquids, or gases. Among them, liquid precursors are preferred, due to their constant surface areas, high vapor pressures, and ease of handling. Currently, many available precursors have limitations such as poor thermal stability, low volatility, and poor reactivity. Therefore, the design and development of new precursors are essential. ALD is an advanced modification of CVD. Single metal precursors such as metal carbonyl complexes can be used in CVD processes. At high deposition temperatures, carbonyl ligands are easily removed, and metal can be deposited directly. Due to precursor decomposition, C and O can be incorporated into films. However, in

ALD, high thermal stability of the precursor is essential to avoid unwanted vapor phase reactions (CVD-type) through precursor decomposition.

High vapor pressure is an important factor to achieve effective mass transport. A low melting point is a good property for precursor compounds. Different ligand designs can be used to tune the melting points of the precursors. Variation of the alkyl groups in ligands can alter the symmetry of the metal complexes, decrease the lattice energies, thereby altering the melting points. Metal precursors containing aromatic ligands tend to have low volatility due to π-stacking interactions. Previous reports have shown that magnesium and calcium *β*-diketiminate complexes containing NMe_2 substituents on the ligand nitrogen atoms sublime at lower temperatures than analogous complexes containing *ter*t-butyl or isopropyl substituents.[57-58] The *β*-diketiminate ligands are shown in Chart 1. Intermolecular repulsion of the nitrogen lone pairs on NMe_2 substituents lowers the lattice energies, thereby increasing the volatilities of the metal precursors.[59]

Chart 1. *β*-diketiminate ligands.

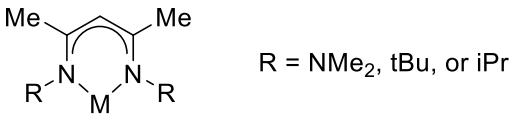

Thermal stability is a very important parameter to consider when designing precursors for ALD. To prevent contaminants (C, N, O, and H) incorporation to the films, highly thermally stable precursors are desired. Precursors must be stable enough during the ALD process to ensure that precursors can be heated at delivery temperatures for an extended amount of time and self-limited growth can be obtained over a wide temperature window. Thermally stable precursor design is based on the steric and electronic structure of the ligand. Generally, anionic ligands afford higher thermal stability, while neutral donor ligands provide low thermal stabilities since neutral ligand

loss provides low temperature decomposition pathways. Many metal carbonyl complexes have sufficient volatility. They are widely used in metal CVD processes because the CO ligands can be easily removed from the metal center at high temperatures. However, CVD-type growth with metal carbonyl precursors can destroy the self-limited behavior of the ALD processes. Thermally stable metal complexes can be designed by avoiding neutral ligands. However, for some metals, neutral ligands saturate the coordination spheres of the metal centers. In such cases, neutral donor ligands that can coordinate strongly with the metal centers are desired.

Precursor reactivity is another crucial factor to consider when designing precursors for ALD. Precursors must show adsorption to substrate surface or reaction with surface reactive sites. Precursors must also demonstrate high reactivity towards co-reactants to obtain desired film materials with reasonable growth rates.[60] Difficulty in reducing metal ions to metal(0) state depends on the electrochemical potential of the metal ion.[5] Therefore, metal ions with positive electrochemical potentials ($E° (Cu^{2+} + 2e^- \leftrightarrow Cu) = 0.3419$ V) show easy reduction into the metal(0) state. When the electrochemical potential becomes more negative, ($E° (Ti^{2+} + 2e^- \leftrightarrow Ti) = -1.630$ V) deposition of these metals by ALD is challenging.[5] Thermal ALD processes of electropositive metal films are limited due to the lack of reactive co-reagents that can reduce the metal ion oxidation state in the precursor to the metal(0) state. When the metal precursors show lower reactivity towards reducing agents, high deposition temperatures or plasma sources should be used to facilitate the film growth by ALD. High deposition temperatures often lead to the incorporation of impurities and the formation of rough films. High energy radicals that are used in plasma-enhanced ALD processes can damage the substrate and participate in radical recombination reactions, thereby limiting the conformal coatings in high aspect ratio features.

There is a limited number of chemical precursors available that have high volatility, thermal stability, and reactivity to use in thermal ALD processes. Still, there are some additional considerations that are also important in selecting a precursor to use in ALD. Byproducts that are formed in film depositions must be volatile to avoid contamination of the films. Additionally, to use in the microelectronics industry, these ALD precursors should be simple to prepare, scalable, and cost-effective.

The selection of a proper co-reactant is also another important factor in thermal ALD.[4-6,33-37,47] In plasma ALD, hydrogen atoms generated by plasma are used as a powerful reducing agent. The type and the dose of the co-reagent affect the film composition and byproduct formation. Cobalt oxide films have been deposited by a low temperature thermal ALD process using $Co(^{tBu}DAD)_2$ (^{tBu}DAD = 1,4-di-*tert*-butyl-1,3-diazabutadienyl) precursor and oxygen co-reagent.[61] However, same Co precursor has been used to deposit cobalt metal films with different reducing agents such as formic acid or *tert*-butylamine.[62-63] Co-reactants such as hydrazine, boranes, formic acid, amines, alcohols, and hydrogen plasma are commonly used in metal film depositions.[62-66] To deposit metal nitride films, ammonia and hydrazine have been used as co-reactants.[22,33,35,37,47] Metal oxide films are deposited using co-reactants such as water, oxygen, ozone, hydrogen peroxide, and oxygen radicals.[49,61,67-68]

1.4 Group 11 Metal ALD Precursors and Processes

1.4.1 Cu Metal

Cu is used as interconnect material in integrated circuits, and it has replaced Al due to its low resistivity and resistance to electromigration.[13] Additionally, Cu has some difficulties to use as a wiring material. Cu can easily diffuse into Si devices or dielectrics, and also Cu has poor adhesion on most of the dielectrics. In order to prevent Cu diffusion, effective barrier layers with

good adhesion properties were introduced.[69] Previously reported Cu precursors are shown in Chart 2.

Chart 2. Copper ALD precursors.

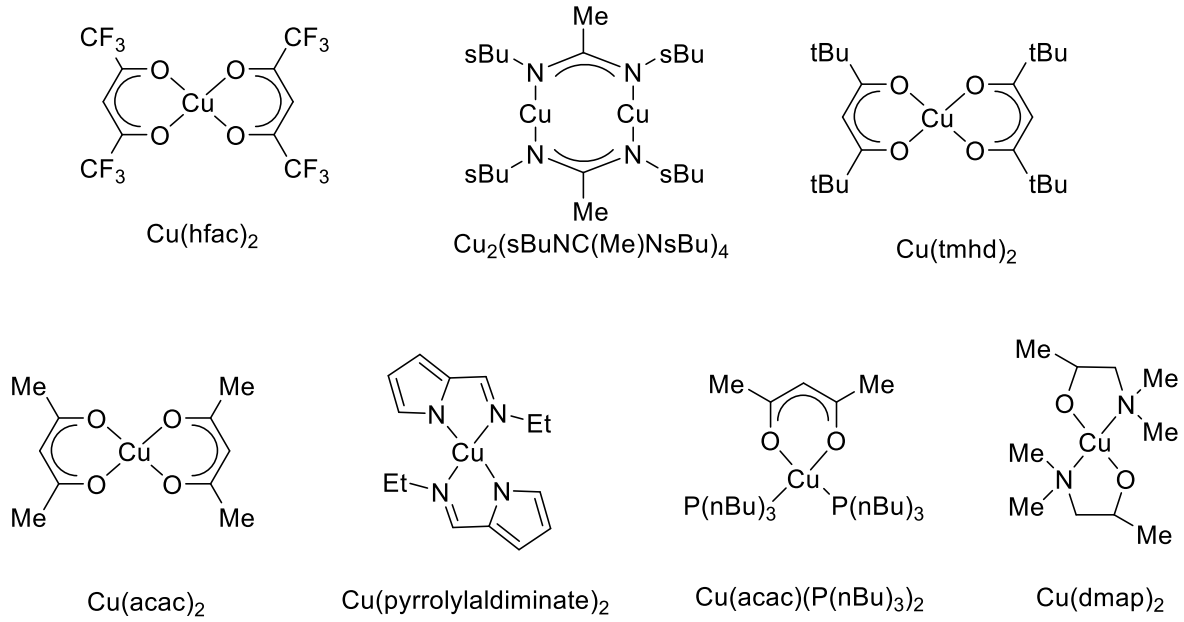

Copper metal deposition has been achieved by indirect and direct ALD processes. Indirect ALD includes the deposition of CuO, Cu_2O, and Cu_3N, followed by the reduction into Cu metal using co-reagents.[47,70] Prior deposition step of copper oxides or nitrides is not required in direct Cu ALD processes. Deposition of copper from CuCl and H_2 at 360-410 °C,[71] CuCl and Zn at 440-500 °C,[72] $Cu(hfac)_2$ and isopropanol at 300 °C,[73] $Cu_2(sBuNC(CH_3)NsBu)_4$ and H_2 at 150-250 °C,[74] and $Cu(tmhd)_2$ and H_2 at 190-260 °C have been reported as direct ALD processes. The precursors used in these direct Cu ALD processes showed low reactivity towards reducing agents at lower temperatures. Therefore, higher deposition temperatures were used. In 2009, uniform, conformal, and high-quality Cu thin films were deposited using $Cu(dmap)_2$ and $ZnEt_2$.[75] This Cu ALD process reported an ALD window of 100-120 °C and the films had low resistivities. At the deposition

temperatures, zinc incorporation was observed. Therefore, this process is not suitable to use in device manufacturing. In 2010, the low temperature ALD of Cu films was reported using similar copper precursors with several reducing agents such as $AlMe_3$ and BEt_3.[76]

In 2011, the Winter group reported a low temperature thermal ALD process using $Cu(dmap)_2$, formic acid, and hydrazine.[77] The $Cu(dmap)_2$ is unreactive toward hydrazine. Therefore, formic acid was used to transform $Cu(dmap)_2$ into copper (II) formate on the substrate surface. Then, hydrazine reduced the copper (II) formate to Cu metal. Cu metal and Cu/Mn alloy films were deposited by low temperature thermal ALD processes using $Cu(dmap)_2$ and $BH_3(NHMe_2)$ co-reactant.[28,78] Recently, high purity and low resistivity Cu thin films were also obtained using $Cu(dmap)_2$ and *tert*-butylhydrazine.[79] This process was studied at low temperatures of 80-140 °C and a growth rate of 0.17 Å/cycle was observed. The major challenge of Cu depositions is to deposit smooth films at very low thicknesses. Cu metal depositions were studied in detail and found out that substrate material has a great influence on film structure.[80] The ALD growth of Cu films was performed using a bis(aminoalkoxide) copper (II) precursor (CTA-1) and H_2 plasma at 30 °C.[80] On many substrates, including TaN and Si, Cu agglomerated to islands while on Ru very thin conductive films were grown. ALD growth on a metal substrate such as Ru can afford continuous and smooth Cu film due to the formation of an interfacial layer that enhances the Cu nucleation. This observation suggests that good wetting of Cu on the substrate is necessary to provide continuous layers at low thicknesses.

1.4.2 Ag Metal

Ag has the lowest resistivity (1.59 μΩ cm)[81] among all elements and is thus potentially an attractive metal to use as interconnects in microelectronics devices. Currently, Cu is used as the interconnect material in integrated circuits. However, in sub-100 nm thicknesses, Cu resistivity

increases due to scattering mechanisms.[82-83] It has been observed that Ag metal films can be scaled down below 100 nm thicknesses without any significant increase in resistivity.[82,84-85] Therefore Ag can be considered as a possible replacement for Cu. High conductivity is also a reason to use Ag metal in photonics.[86] There is a growing interest in Ag thin films to use in plasmonic devices.[87] It has been shown that localized surface plasmon resonances of Ag nanoparticles can be used to enhance Raman scattering in surface-enhanced Raman spectroscopy (SERS).[88-90] Additionally, thin Ag metal films can be used as gas sensors.[91] The chemisorption of gas molecules on the Ag metal surface changes its reflectivity.[91] Ag surfaces can also be used in catalysis and biological applications such as antimicrobial coatings.[35,86,92] The catalytic activity of nanoparticles is tunable through better control of size, shape, and composition.[93] Ag thin film deposition is a challenge mainly due to the coalescence of Ag atoms on substrates at early stages of growth to form nanoparticles. This nanoparticle growth takes a long time to form a continuous film. Furthermore, the nanoparticles lead to rough films. The growth of Ag films by thermal ALD is poorly developed due to the low thermal stabilities of the available precursors. Previously reported Ag precursors are shown in Chart 3. The Ag ion has a very positive electrochemical potential ($E°$ ($Ag^+ + e^- \leftrightarrow Ag$) = 0.7996 V)[94] and Ag(I) in the complexes can easily be reduced into Ag metal by the anionic ligands. This is the key problem of making Ag precursors with highest thermal stabilities. Most of the known Ag precursors are composed of anionic β-diketonate, carboxylate, or ketoiminate ligands and neutral donor ligands such as phosphines (PEt_3) or alkenes (cyclooctadiene, COD). Neutral ligands can easily dissociate from the metal complexes by giving a low-temperature decomposition pathway.

Chart 3. Silver ALD precursors.

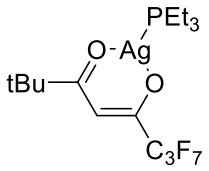

Ag(fod)(PEt_3)

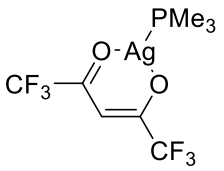

Ag(hfac)(PMe_3)

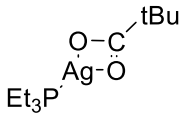

Ag(Piv)(PEt_3)

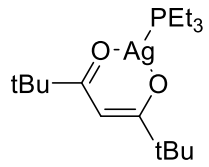

Ag(thd)(PEt_3)

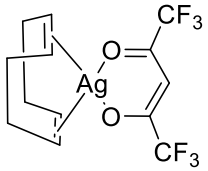

Ag(hfac)(1,5-COD)

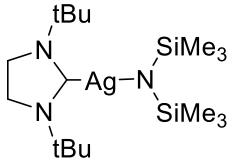

[(NHC)Ag(hmds)]

Silver metal depositions have been carried out using plasma ALD and thermal ALD. Plasma ALD processes include Ag(O_2CtBu)(PEt_3) and hydrogen radicals at 140 °C,[95] Ag(fod)(PEt_3) and H_2 at 120-150 °C,[64] Ag(fod)(PEt_3) and H_2 at 70-200 °C on various substrates (SiO_2, TiN, Ti/TiN, Co, Ni, and W),[96] and [(NHC)Ag(hmds)] and H_2 at 100 °C.[97] In these plasma ALD process, low resistivity Ag films were obtained. However, films deposited by plasma ALD may be non-conformal in high aspect ratio features. Thermal ALD processes including Ag(hfac)(1,5-COD) and propanol between 110-150 °C,[98] (hfac)Ag(PMe_3) and formalin between 170-200 °C,[99] (hfac)Ag(PMe_3) , TMA, and water at 110 °C,[99] Ag(hfac)(1,5-COD) and propanol between 121-130 °C,[100] Ag(hfac)(1,5-COD) and *tert*-butylhydrazine between 80-200 °C,[101]and Ag(fod)PEt_3 and $BH_3(NHMe_2)$ at 110 °C[102] gave Ag nanoparticles with low growth rates. Continuous Ag thin films have not been deposited using thermal ALD processes so far. This dissertation describes the thermal ALD of Ag metal.

1.4.3 Au Metal

The development of Au ALD has been hindered by the low thermal stabilities of available Au complexes. Au has very high positive electrochemical potentials (E° Au(I) = 1.692 V and E° Au(III) = 1.498 V).[94] Therefore finding a thermally stable Au precursor has proven to be difficult because most of the ligands can easily reduce Au ions to Au metal. Although many CVD precursors are available to deposit Au,[103-107] only three ALD processes have been reported.[108-110] Two different Au precursors used in ALD are shown in Chart 4. The bulk resistivity of Au is 2.44 μΩ cm.[81] Generally, Au is considered the best material for low-voltage, low-current, and low-contact-force applications such as gold-plated contacts and connectors.[111] Au metal is relatively stable and has low reactivity towards many chemical compounds. High reliability can be achieved from electronics components made of Au.[109] Particulate Au coatings also can be used in photonic applications.[109,112-113] The use of Au is avoided in semiconductor technology because Au diffuses into the underlying Si substrates even at moderate temperatures and charge carriers (electrons and holes) recombine at Au defects in Si and are eliminated. Au is also an expensive material to use in microelectronics devices. The deposition of a continuous and conductive Au film by ALD remains a challenge. ALD requires volatile, thermally stable, and reactive metal precursors.

Chart 4. Gold ALD precursors.

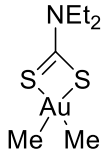

$Me_2Au(S_2CNEt_2)$

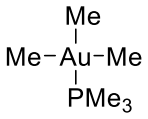

$Me_3P\text{-}AuMe_3$

The first Au ALD process was reported in 2016 by Griffiths and co-workers.[108] In this plasma-enhanced ALD process, the surface was first exposed to the Au precursor Me_3PAuMe_3, followed by oxygen plasma. Then water vapor was used as a ternary reactant to hydrolyze the phosphorous impurity to phosphoric acid. This phosphoric acid was removed during the purge step. Metallic Au was deposited at 120 °C with a growth rate of 0.5 Å/cycle. The second Au ALD process was reported in 2017 by Mäkelä and co-workers.[109] $Me_2Au(S_2CNEt_2)$ used as the Au precursor and ozone was used as the reactant. Self-limiting growth was observed at 180 °C with a growth rate of 0.9 Å/cycle. Low resistivity Au thin films were deposited by thermal ALD for the first time. Recently, a Au plasma-enhanced (PEALD) process was reported using $Me_3Au(PMe_3)$ and H_2 plasma.[110] Island-like growth was observed at lower thicknesses, but continuous films were observed when the films were 65.6 nm thick. Pure gold films with <1 at. % carbon and oxygen were obtained at 120 °C.

1.5 Thesis Problem

Metal thin films prepared by ALD are attractive materials in microelectronics manufacturing because ALD provides highly conformal films in high aspect ratio features. Therefore, thin film deposition by ALD is an essential technique in the microelectronics industry. This thesis focus on the design and synthesis of highly thermally stable Ag metal precursors and the deposition of Ag metal films by thermal ALD. Ag metal has the lowest resistivity (1.59 μΩ cm) among all elements and may be a promising metal to use as interconnects in microelectronics. There is a growing interest in Ag thin films for use in plasmonic devices as well. Ag metal has been deposited by plasma and thermal ALD processes. Very few thermal ALD processes have been reported to deposit Ag metal. All of the reported thermal ALD processes resulted in the formation of nanoparticles instead of continuous film growth. Therefore, Ag metal is challenging

to deposit using thermal ALD. Film growth by thermal ALD has been hindered by the low thermal stabilities of all silver precursors reported to date due to the positive electrochemical potential of Ag ion. Major issues include the lack of suitable metal precursors and reducing co-reagents. Generally, in ALD processes, the first nuclei appear on the substrate surface and grow into nanoparticles as the new nuclei appear. After depositing enough ALD cycles, nanoparticles coalescence to grow a continuous film. Then the growth process continues. In noble metal film depositions, effective nucleation may start after many ALD cycles. The number of cycles required to achieve the steady state growth rate is known as "nucleation delay." Substrates with higher surface energies than Ag act as wetting layers, thereby enhance the Ag nucleation. Therefore, substrate selection also a critical parameter in Ag ALD. The surface reactions are determined by the precursor and also the substrate material. As a result, thermally stable, highly volatile, and reactive Ag metal precursors need to be designed and synthesized.

The major goals and the focus of this thesis work are the design and synthesis of thermally stable and volatile Ag metal precursors, screening of reducing co-reagents, and deposition of Ag metal by thermal ALD. Ag has the lowest first ionization energy, but higher second and third ionization energies than copper and gold.[114] Therefore, the most common oxidation state for silver metal is +1. The crystal field stabilization energy is zero for d^{10}, and it is very stable. Therefore, Ag prefers linear complexes with coordination number two. In order to decrease the electron density on the metal to avoid self-reduction, anionic electron-withdrawing ligands are desired. Electron-withdrawing substituents pull the electron density away from the ligand. Therefore, the electron density is decreased on the metal, making the Ag ion more difficult to reduce to the metallic state. This approach should give metal complexes with the highest possible thermal stability. The addition of bulky alkyl or fluorinated groups to a ligand can lower the intermolecular

attractions between individual molecules, reduce the lattice energies, resulting in higher volatility. Neutral donor ligands can saturate the coordination sphere. Therefore, strong donor ligands that can coordinate with the metal center are desired. Previously reported Ag pyrazolates, $[Ag(3,5\text{-}CF_3)_2Pz]_3$ and $[Ag(3\text{-}tBu,5\text{-}C_3F_7)Pz]_3$ were identified as highly thermally stable and volatile Ag metal precursors.[115] These precursors have not been used in any Ag plasma or thermal ALD processes.

The structure and properties of the complexes will be evaluated by NMR spectroscopy, infrared spectroscopy, melting point determinations, CHN microanalyses, and X-ray crystal structure determinations. The volatilities and thermal stabilities will be determined by preparative sublimations, thermogravimetric analysis (TGA)/differential thermal analysis (DTA), and thermal decomposition temperature measurements. ALD growth studies will be performed using the highly thermally stable silver pyrazolate precursor $[Ag(3,5\text{-}CF_3)_2Pz]_3$ and appropriate co-reagents. The film compositions and morphologies will be assessed by X-ray photoelectron spectroscopy (XPS), X-ray diffraction (XRD), X-ray fluorescence spectroscopy (XRF), and scanning electron microscopy (SEM).

CHAPTER 2
ATOMIC LAYER DEPOSITION OF SILVER THIN FILMS USING HIGHLY THERMALLY STABLE AND VOLATILE SILVER PYRAZOLATE PRECURSOR

2.1 Introduction

Recently, there has been great attention paid toward Ag thin film depositions due to the potential use of Ag in plasmonic devices.[87] Ag nanostructures can be used to harness electromagnetic surface waves known as surface plasmons that generate along their surface.[116-117] Once the electromagnetic field of light has been converted into surface plasmons, it propagates on the metal surface but slowly decreases its intensity due to the losses arising from absorption in the metal.[118] The propagation length is a characteristic scale in surface plasmon-based photonics, which is dictated by loss in the metal. For Al metal, the propagation length is 2 μm at 500 nm wavelength. However, at the same wavelength, Ag has a propagation length of 20 μm.[118] Potential applications of surface plasmons include optics, data storage, light generation, microscopy, solar cells, and sensors for detecting biological molecules.[118] The metallic nanoparticle research field has reported that the plasmonic effect can be enhanced by changing the size, shape, and geometry of the nanoparticles.[119-120] Ag is also an attractive material to use as interconnects in microelectronics due to its resistivity (1.59 μΩ·cm), which is the lowest for any metal.

Ag films have usually been prepared using techniques such as physical[121-122] and chemical vapor deposition (CVD).[85,115,123-129] Recently, several plasma ALD processes have been used in Ag thin film depositions.[64,95-97] Generally, in plasma ALD, conformality is limited due to radical recombination reactions in high aspect ratio features. Highly reactive plasma species can also damage the substrates and growing films, thereby resulting in rough films. Growth by thermal ALD has been hampered by the low thermal stabilities of almost all available Ag precursors. Previously reported Ag precursors are composed of β-diketonate, carboxylate, or ketoiminate

ligands and neutral donor ligands such as phosphines (PEt_3) or alkenes (cyclooctadiene, COD).[127,130-138] The neutral donor ligands provide a saturated coordination environment to the metal center and prevent aggregation in the solid state. However, loss of alkenes at or below the sublimation temperatures of the Ag complexes forms less volatile species such as $[Ag(hfac)]_n$. The phosphine ligands can improve stability during volatilization, but films can be contaminated by P and C. Precursor decomposition can also be minimized by decreasing the deposition temperatures.

Pyrazolate ligands have been used to prepare volatile noble metal complexes (Ru and Os) for thermal CVD processes.[139-140] In 2005, the synthesis and characterization of a series of silver pyrazolate complexes were reported.[115] The bis-trifluoromethyl substituted complex $[Ag(3,5\text{-}CF_3)_2Pz]_3$ was used to deposit Ag films by low-pressure CVD experiments at temperatures between 250 and 350 °C. $[Ag(3,5\text{-}CF_3)_2Pz]_3$ showed better thermal stability than all other Ag precursors reported so far. Electron-withdrawing trifluoromethyl groups pull the electron density away from the pyrazolate nitrogen atoms. Therefore, the electron density is decreased on the Ag ion, which enhances the thermal stability of the complex. $[Ag(3,5\text{-}CF_3)_2Pz]_3$ sublimed at 110 °C/0.5 Torr without decomposition.[115] The higher volatility of this precursor should be due to the presence of the trifluoromethyl substituents. Lone pairs on the fluorine atoms repel each other to reduce intermolecular attractive bonding interactions. Therefore, the presence of trifluoromethyl groups decreases lattice energies, thereby increasing volatilities.

This chapter reports precursor properties of $[Ag(3,5\text{-}CF_3)_2Pz]_3$ (**1**) and $[Ag(3\text{-}tBu,5\text{-}C_3F_7)Pz)]_3$ (**2**) and Ag metal depositions with **1** and 1,1-dimethylhydrazine as the reducing agent. Chemical structures of Ag pyrazolate precursors are shown in Chart 5. The focus on bulky alkyl or fluorinated substituents is to enhance the thermal stabilities and volatilities of Ag precursors. Ag metal depositions on various substrates were performed using highly thermally stable and

volatile precursor **1** and 1,1-dimethylhydrazine. The Ag metal films were characterized with regard to thickness, morphology, crystallinity, and composition using SEM, XRF, grazing incident X-ray diffraction (GI-XRD), and XPS.

Chart 5. Trimeric silver pyrazolates (a) **1** and (b) **2**.

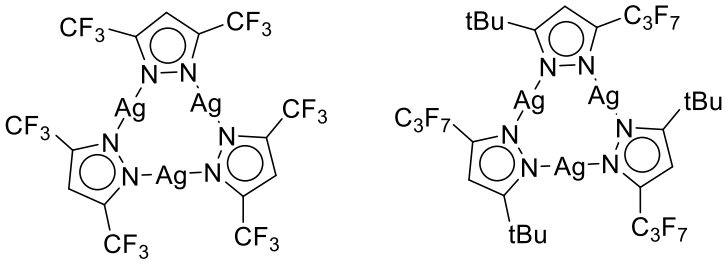

2.2 Result and Discussion

Precursor selection and initial studies for substrate selection. Precursors **1** and **2** were prepared by reported methods.[141-142] The volatility and thermal stability of **1** and **2** were determined by melting points, thermal decompositions, TGAs, and preparative sublimation studies to evaluate their suitability for the thermal ALD process. Sublimation temperatures, melting points, thermal decomposition temperatures for **1** and **2** are listed in Table 1.

Table 1. Thermal properties of **1** and **2**.

Complex	Melting Point (°C)	Thermal Decomposition Temperature (°C)	Sublimation Temperature (°C/ 0.2 Torr)	% Recovery
1	235-238	277	130	98
2	184-186	245	120	95

Complexes **1** and **2** sublimed at 130 °C/0.2 Torr and 120 °C/0.2 Torr, respectively. Complexes **1** and **2** offer sufficient volatility to use as ALD precursors. The melting points and thermal decomposition temperatures were determined in a sealed capillary tube, where a color change was observed upon decomposition of the material. Complex **1** showed a higher thermal decomposition temperature than **2**. The above observations suggested that the presence of trifluoromethyl groups reduces the electron density on the pyrazolate ligand to minimize self-reduction of the Ag ion and facilitate better thermal stability. TGA experiments were performed to understand the thermal behavior of **1** and **2** and are shown in Figure 9. Complexes **1** and **2** showed single step weight losses with approximately zero residual masses, due to the volatilization without decomposition. The 10% weight loss temperatures in TGAs approximate the 1 Torr vapor pressures at atmospheric pressure. For **1** and **2** 10% weight loss temperatures were 232 and 238 °C, respectively. Therefore, **1** is slightly more volatile than **2**, consistent with the higher molecular weight of **2**.

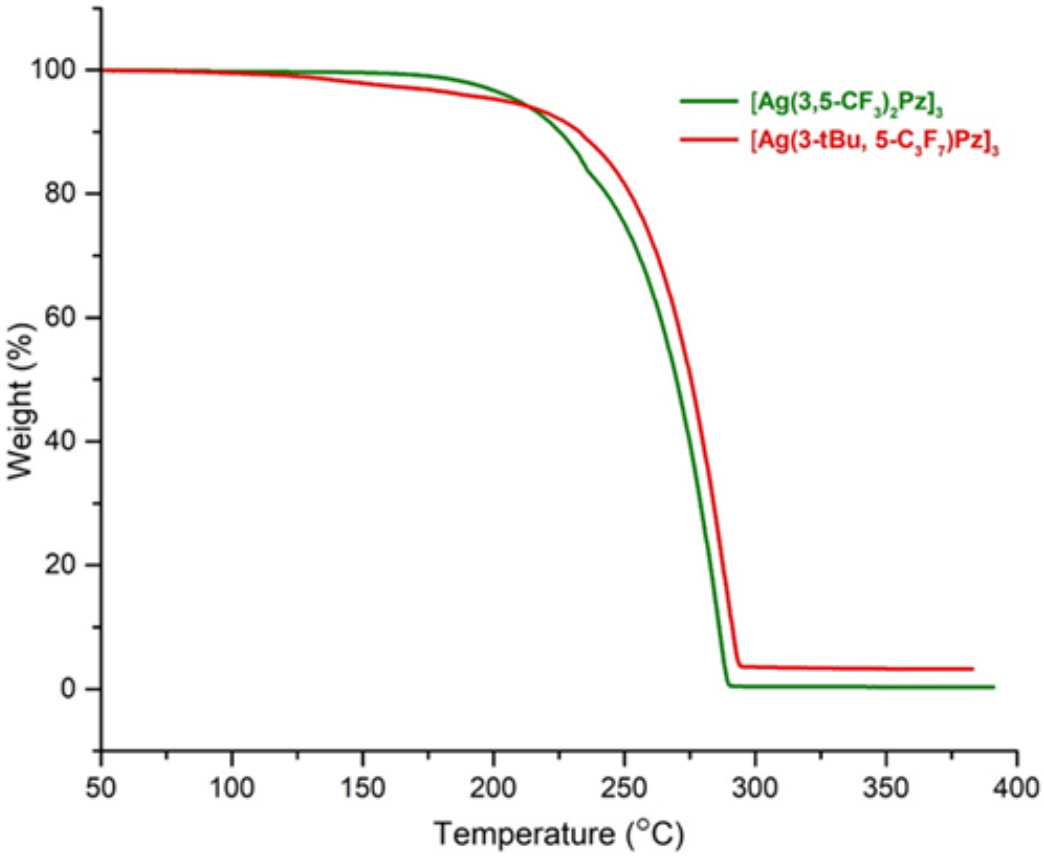

Figure 9. TGA traces of **1** and **2** (The heating rate was 10 °C/min).

To investigate the initial evidence of metal formation in solution, Ag pyrazolates **1** and **2** were treated with volatile reducing agents to obtain the silver metal in solution. Ag pyrazolates **1** and **2** (500 mg) were dissolved in 10 mL of tetrahydrofuran (THF) under inert atmosphere. Then, 5 molar equivalents (excess) of the reducing agent was added slowly with stirring. The first evidence of metal formation would involve gas evolution and formation of black/silver, insoluble precipitate. If no reaction was observed, then the solution was refluxed for five hours. The solution was then cooled to room temperature and the precipitate was collected. The residue was subjected to powder XRD to verify the presence of metal. Both **1** and **2** are reactive towards several reducing agents such as aqueous N_2H_4, 1,1-dimethylhydrazine, *tert*-butyl hydrazine, and formic acid (Table 2).

Table 2. Solution reduction experiment results for **1** and **2** in tetrahydrofuran.

Reducing agent	**1**	**2**
Aqueous N_2H_4	Ag mirror, 23 °C, 1 min	Ag mirror, 23 °C, 1 min
1,1-Dimethylhydrazine	Ag mirror, 66 °C, 1 min	Ag mirror, 66 °C, 10 min
tert-Butyl hydrazine	Ag mirror, 66 °C, 1 min	Ag mirror, 23 °C, 10 min
Formic acid	Ag mirror, 66 °C, 10 min	Ag mirror, 66 °C, 5 min
2-Propanol	No reaction at 23 or 66°C	Black color, 4h, 66 °C
1-Propanol	No reaction at 23 or 66°C	No reaction at 23 or 66°C

Complex **1** was selected as the metal precursor to deposit Ag films due to its higher thermal stability and better volatility, compared to **2**. Complex **1** has already been used as a CVD precursor in the temperature range of 250-350 °C,[115] while **2** has not been used in CVD or ALD experiments. 1,1-dimethylhydrazine was chosen as the co-reactant since it is reactive towards **1** in solution and is easy to deliver using a vapor-draw bubbler. Since **1** has used as a CVD precursor,[115] it is very important to determine the CVD component at the working temperatures range from 160-240 °C. The experiment to determine the CVD growth on different substrates was carried out by conducting depositions in the absence of the reducing agent. Initial depositions were carried out with several substrates such as SiO_2, Co, Ru, Si, Cu, Pt, and TiN. Ag metal can be deposited on all of these substrates using **1** and 1,1-dimethylhydrazine at 180 °C. Selected SEM images are shown in Figure 10.

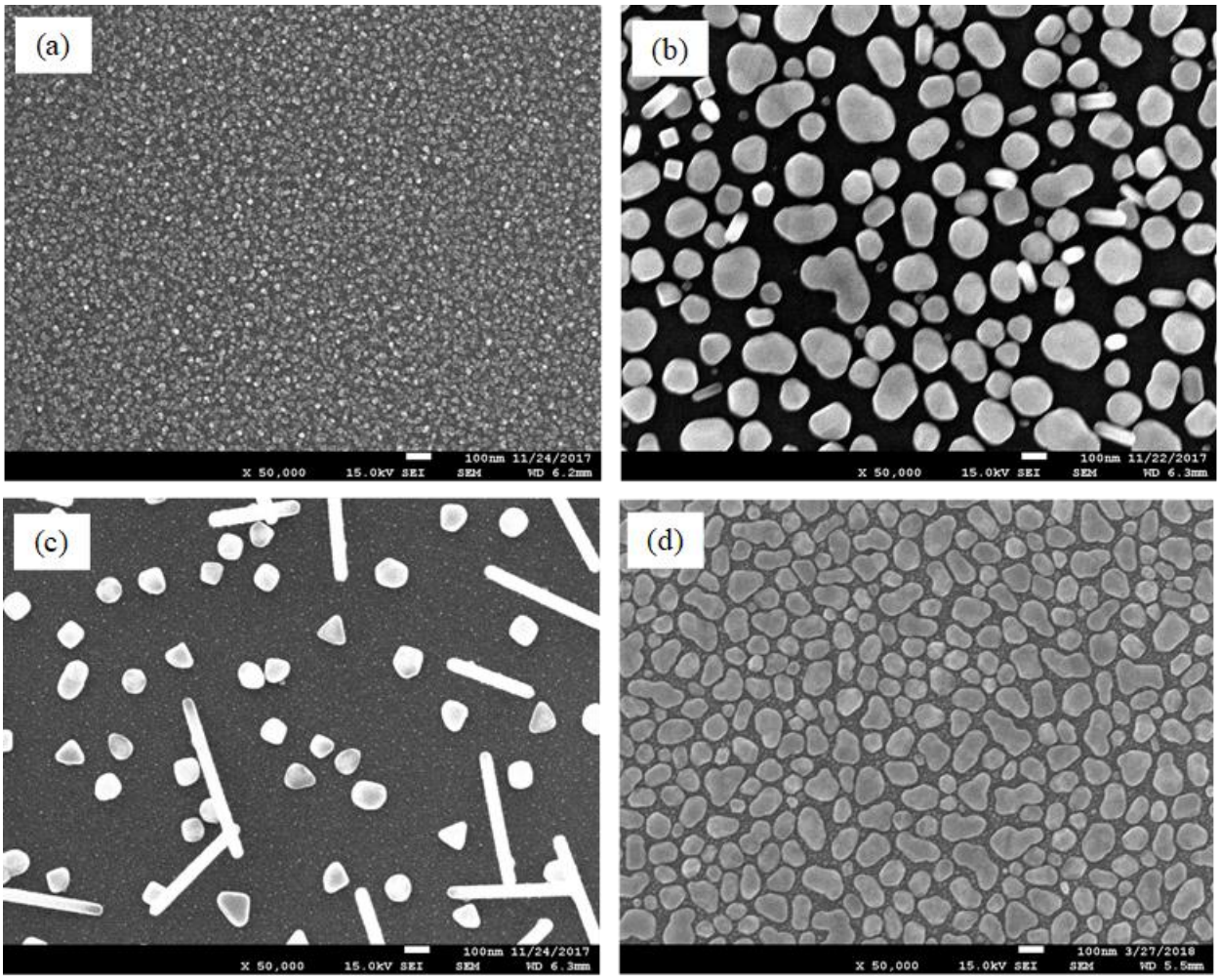

Figure 10. Top down SEM images of a Ag metal films deposited on (a) Si (b) Co (c) Pt (d) Ru substrates at 180 °C

However, Ag metal deposition was observed on Si, TiN, Cu, Ru, and Pt substrates in the absence of 1,1-dimethylhydrazine as well. For instance, Ag metal growth on Cu substrates is shown in Figures 11 and 12. Cu can act as a catalytic surface and reduce Ag metal precursor into silver metal by making volatile Cu species. Consequently, similar thicknesses were observed with and without the co-reactant.

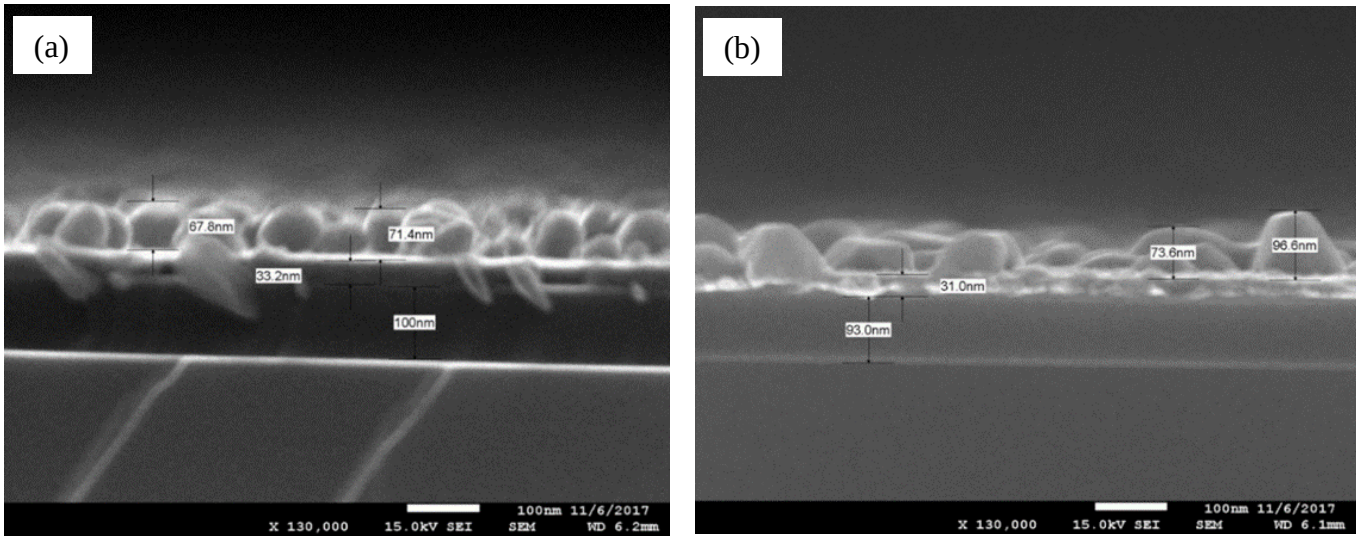

Figure 11. Cross-sectional SEM images of a Ag metal film deposited on a Cu substrate at 180 °C (a) **1** + 1,1-dimethylhydrazine (b) **1** only.

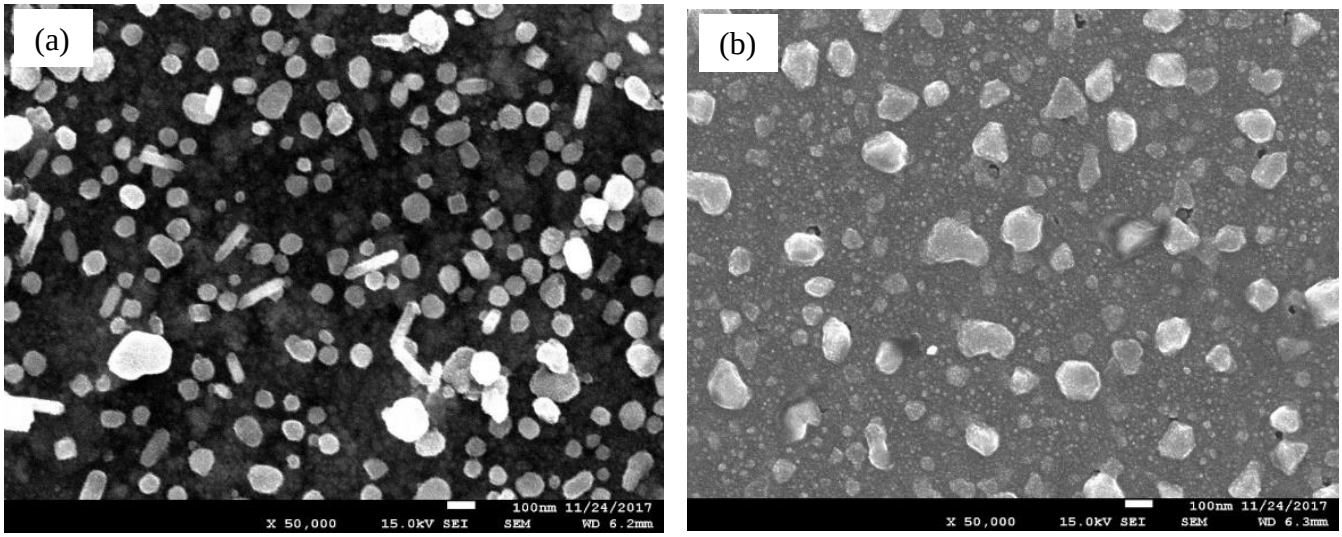

Figure 12. Top down SEM images of a Ag metal film deposited on Cu a substrate at 180 °C (a) **1** + 1,1-dimethylhydrazine (b) **1** only.

Nearly no growth was observed on Co and SiO_2 in the absence of 1,1-dimethylhydrazine. Figure 13 shows cross sectional SEM images of the Ag depositions on SiO_2 substrates at 180 °C. Therefore, SiO_2 substrates were selected to carry out the ALD study. Depositions were conducted with no co-reactant in the temperatures range from 160-240 °C to demonstrate the CVD component on the SiO_2 substrate (Figure 14). Since SEM measurements were not accurate enough to show the very small Ag growth observed on SiO_2 in the absence of co-reactant, Ag intensities were measured by XRF. XRF Ag concentrations of <20 counts/s were measured with no 1,1-dimethylhydrazine in the temperature range of 160-240 °C. However, Ag growth enhanced with the use of 1,1-dimethylhydrazine, and Ag concentrations were measured as 70-150 counts/s.

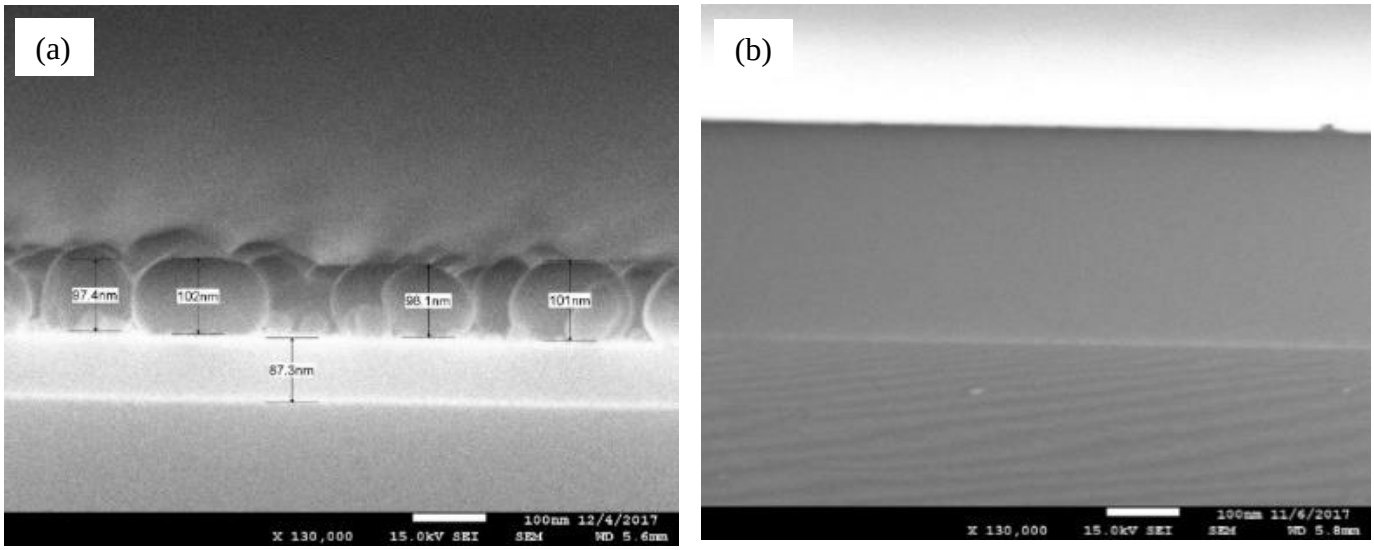

Figure 13. Cross-sectional SEM images of the deposition on SiO_2 at 180 °C (a) **1** + 1,1-dimethylhydrazine (b) **1** only.

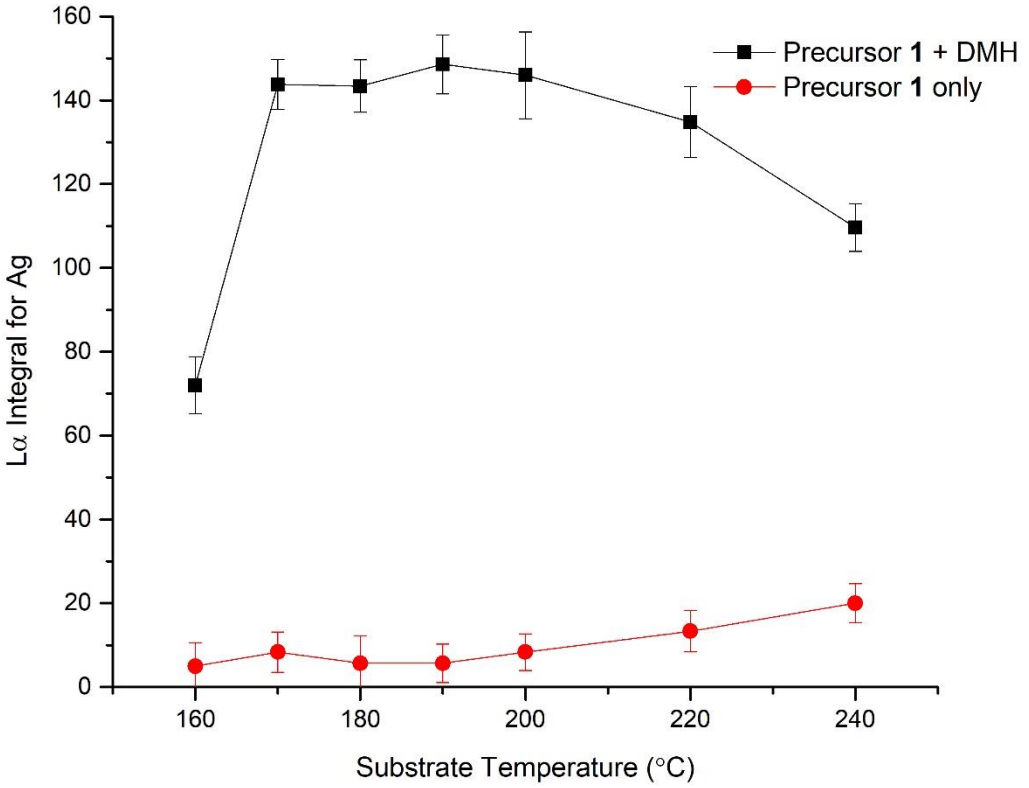

Figure 14. Plot of Ag concentration (counts/s) versus substrate temperature on SiO_2 substrates.

Self-limited growth and ALD window. Precursor pulse lengths, substrate temperatures, and the number of cycles were varied to evaluate the growth behavior. The growth rate was investigated as a function of the pulse lengths of **1** and 1,1-dimethylhydrazine at 180 °C using 1000 cycles and 10.0 s and 5.0 s N_2 purges after each precursor pulse. Nanoparticles with different sizes were observed in the cross-sectional SEM images. The nanoparticle height may not be an accurate method to present the growth rates. Therefore, XRF silver concentrations were measured to confirm the results obtained from SEM measurements. Using a recipe of **1** (variable)/N_2 (10 s)/1,1-dimethylhydrazine (0.1 s)/N_2 (5s) a growth rate of ~1.0 Å/cycle was found at ≥3.0 s pulse lengths of **1** (Figure 15(a)). XRF Ag concentration of ~150 counts/s was measured at ≥3.0 s pulse lengths of **1** (Figure 15(b)). Consumption of **1** increased gradually with increasing pulse times, which rules out precursor vapor depletion and pseudosaturation behavior in the delivery system.

Using a 3.0 s pulse of **1**, the growth rate of ~1.0 Å/cycle was observed for 1,1-dimethylhydrazine pulse length of ≥0.1 s (Figure 16(a)). For the above recipe, the XRF Ag concentration of ~150 counts/s was measured at ≥0.1 s pulse length of 1,1-dimethylhydrazine (Figure 16(b)). For the next growth experiments, **1** and 1,1-dimethylhydrazine pulse lengths were kept at 3.0 s and 0.1 s, respectively.

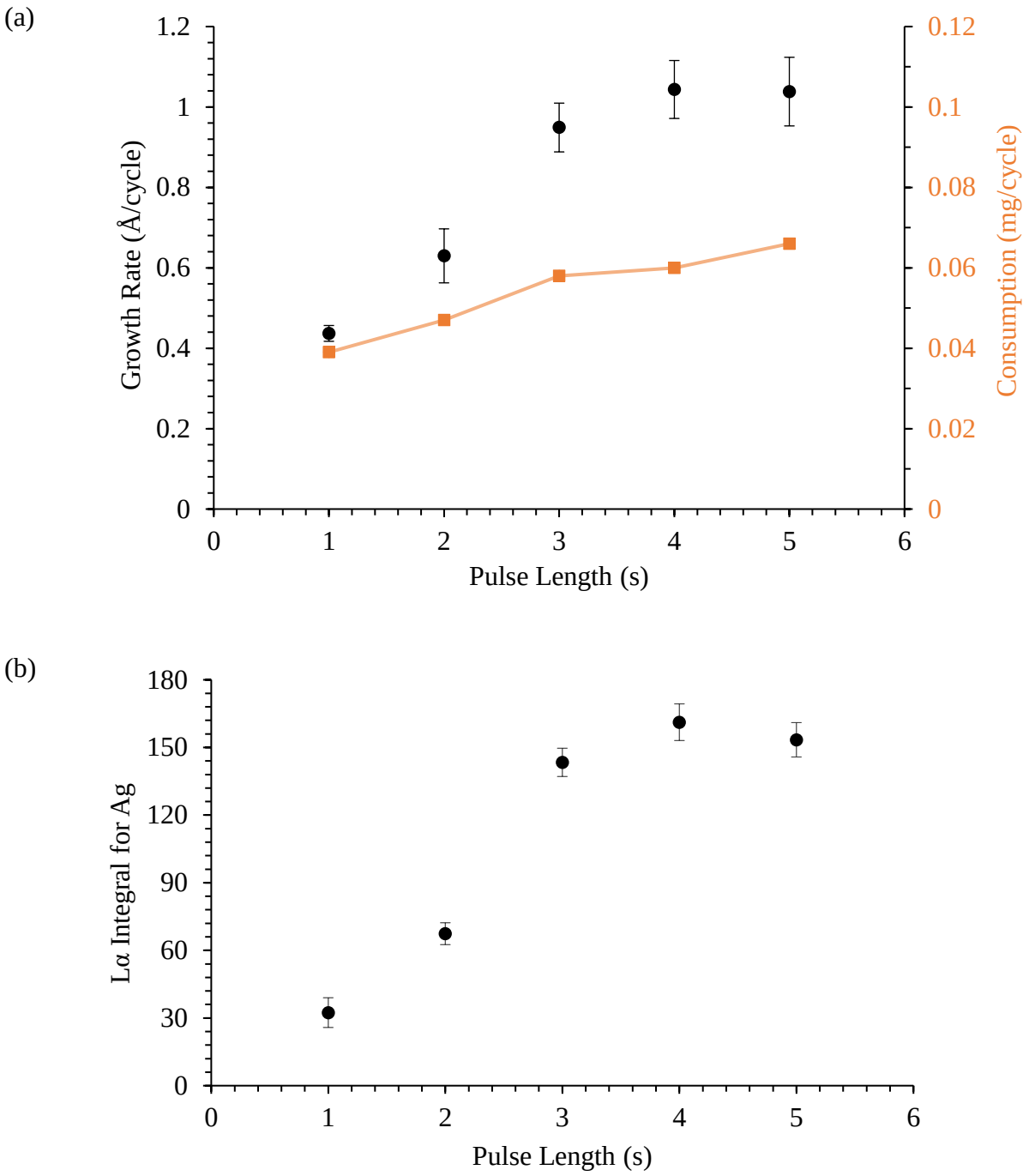

Figure 15. Dependence of growth rate on the pulse length of **1** for a Ag film grown at 180 °C with 1000 cycles on SiO_2 by (a) SEM and (b) XRF.

(a)

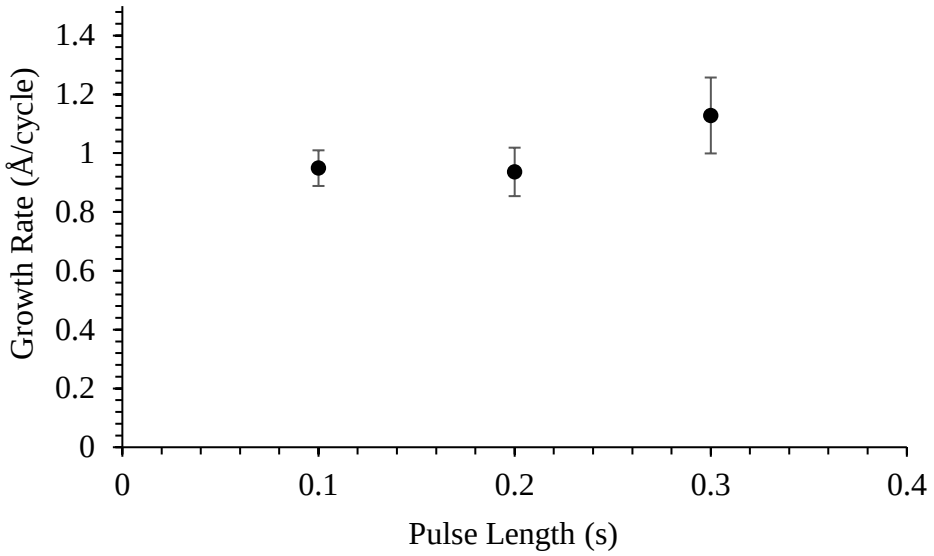

(b)

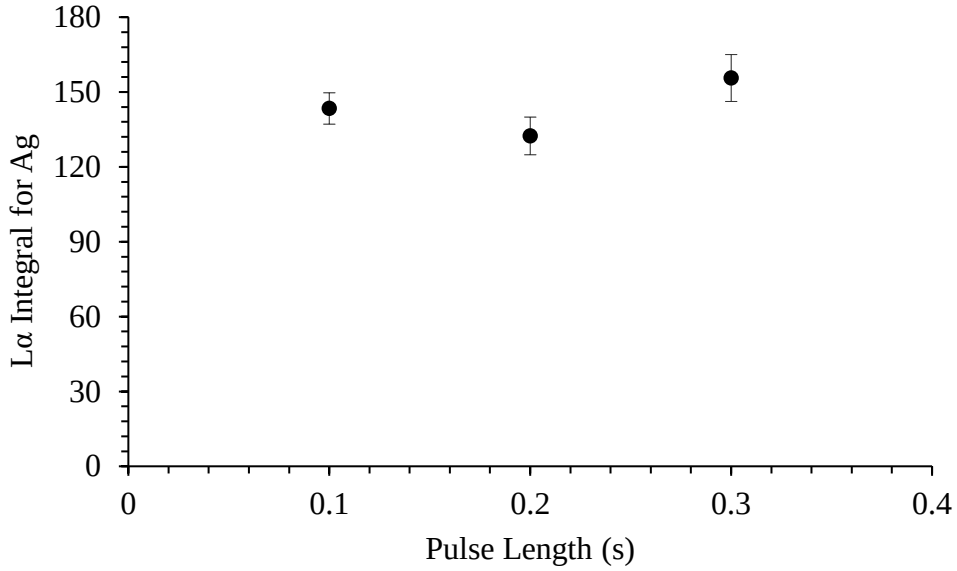

Figure 16. Dependence of growth rate on DMH pulse length for a Ag film grown at 180 °C with 1000 cycles on SiO_2 by (a) SEM and (b) XRF.

Based on the saturative doses, a pulse sequence of **1** (3.0 s)/N_2 purge (10.0 s)/1,1-dimethylhydrazine (0.1 s)/N_2 purge (5.0 s) was used for all following depositions. The effect of deposition temperature on the growth rate per cycle was studied in the temperature range of 160 to 240 °C. An ALD window was observed from 170 to 220 °C with a growth rate of about 1.0 Å/cycle (Figure 17(a)). XRF Ag concentrations of ~150 counts/s of were measured over the temperature range of 170-220 °C (Figure 17(b)). A lower growth rate was observed at 160 °C, possibly due to the insufficient reactivity of the precursors at low temperatures. At temperatures above the ALD window, a lower growth rate was observed, due to precursor desorption or loss of reactive sites. The ALD window is very important in industrial applications, where small temperature fluctuations can be tolerated by having a wide window where growth rates do not change. The ALD window observed herein can be compared with previously reported Ag thermal ALD processes. The thermal ALD process using Ag(hfac)(COD) and 1-propanol afforded a ALD window of 123-128 °C.[100] After that, Ag(hfac)(COD) used with *tert*-butyl hydrazine and afforded 105-128 °C temperature window.[101] A recently reported thermal ALD process employing Ag(fod)PEt_3 and $BH_3(NHMe_2)$ afforded an ALD window of 110-120 °C.[102]

(a)

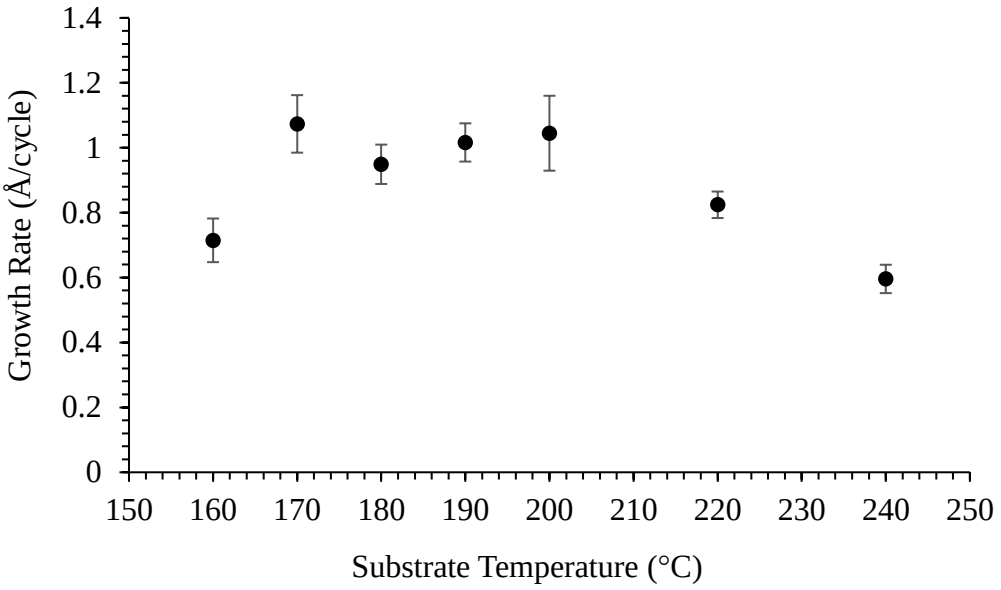

(b)

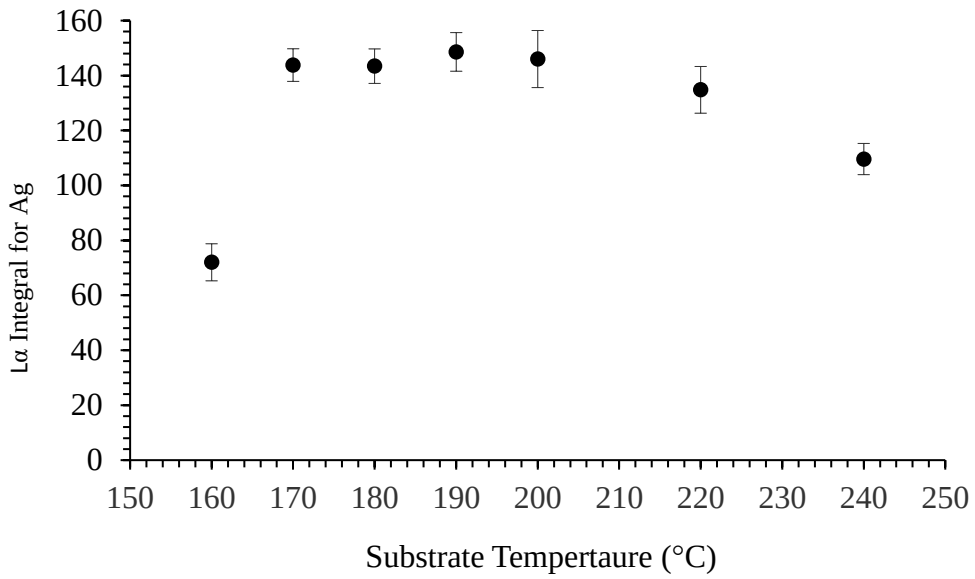

Figure 17. Dependence of growth rate on deposition temperature with 1000 cycles on SiO_2 by (a) SEM and (b) XRF.

Next, the dependence of film thickness on the number of cycles was studied at 180 °C using a saturative pulse sequence of **1** (3.0 s)/N_2 purge (10.0 s)/1,1-dimethylhydrazine (0.1 s)/N_2 purge (5.0 s). The resultant plot was linear (Figure 18(a)) with a slope of 0.82 Å/cycle, which is lower than the measured growth rate after precursor saturation and ALD window of 1.0 Å/cycle. To confirm the linear growth, XRF Ag concentrations were plotted with different number of deposition cycles (Figure 18(b)). The x and y-intercepts are ~125 and -18.6, respectively. These values indicate about 125 cycles of nucleation delay before steady state growth is reached.

(a)

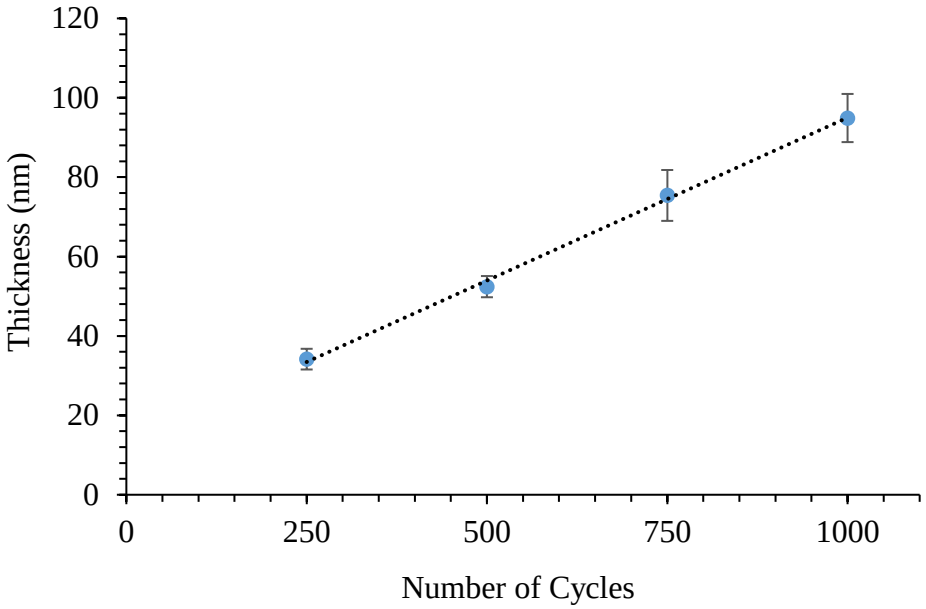

(b)

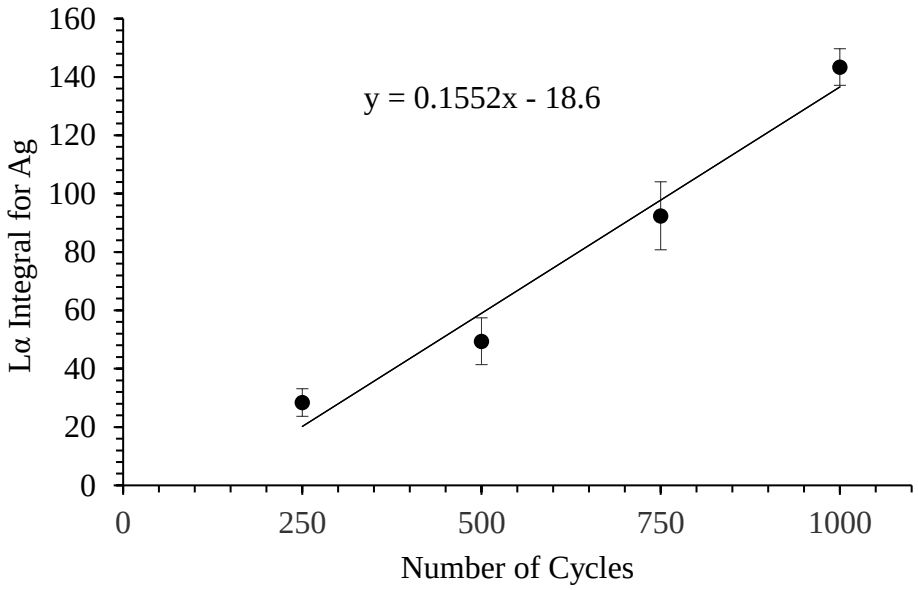

Figure 18. Thickness versus number of cycles on SiO_2 substrates at 180 °C by (a) SEM and (b) XRF.

Film analyses. All depositions produced discontinuous particles rather than continuous films (Figure 19). Thicker films consisted of particles with different sizes, which resulted from coalescence and continued nucleation. Even after 1000 cycles, Ag nanoparticles were not connected to make a continuous film. All the films were non-conductive due to the particle growth of the films and gaps between the islands.

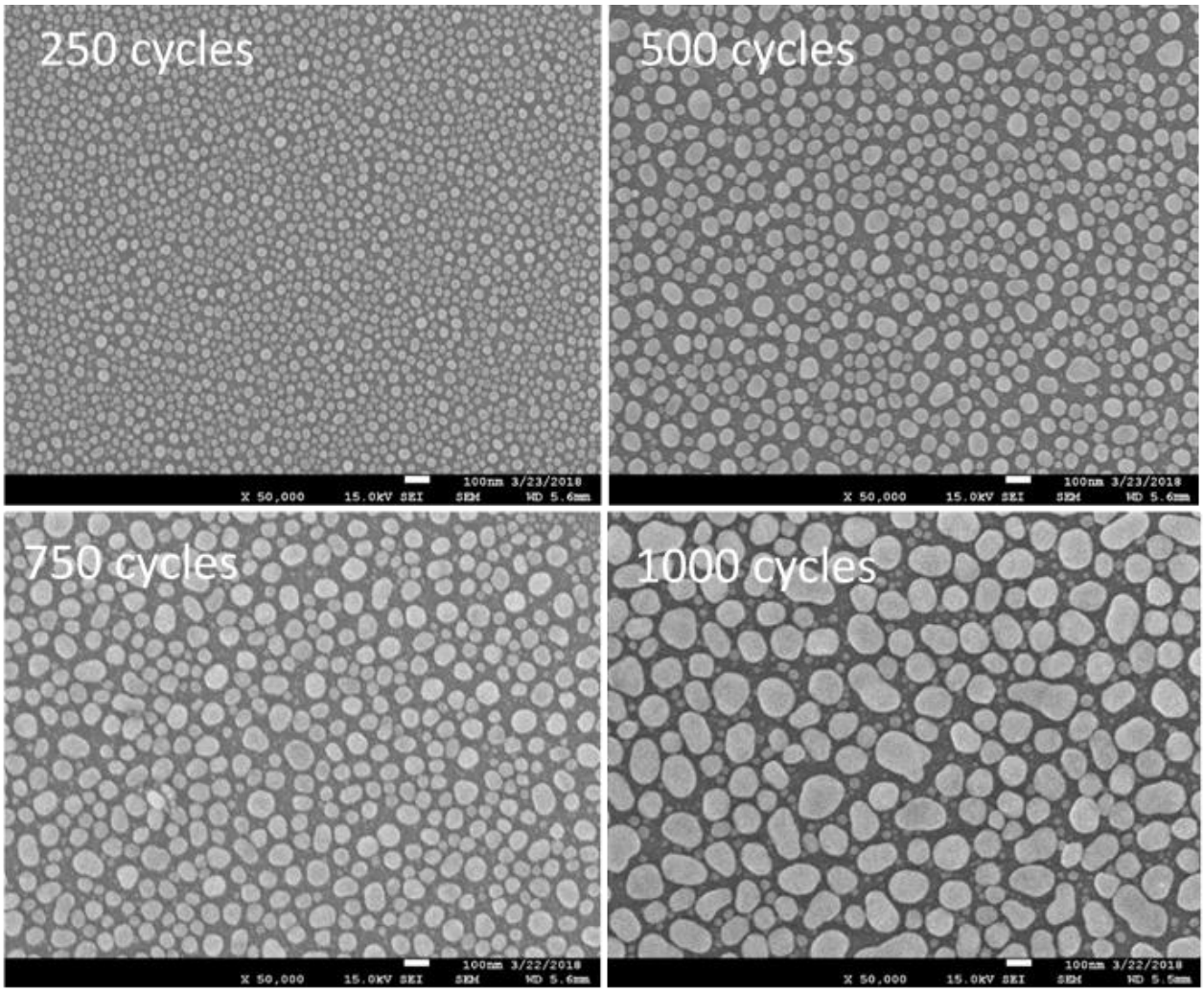

Figure 19. Top-down SEM images after different number of cycles at 180 °C on SiO_2.

The crystallinity of the Ag films was studied by GI-XRD. Figure 20 shows the GI-XRD patterns for silver metal grown at 180 °C on SiO_2 substrates. As shown, the diffraction pattern was

indexed as Ag (PDF 00-003-0931). The broad reflections suggest that the presence of small crystallites. Reflections at 2θ = 38.04º and 44.80º correspond to the cubic phase of metallic Ag.

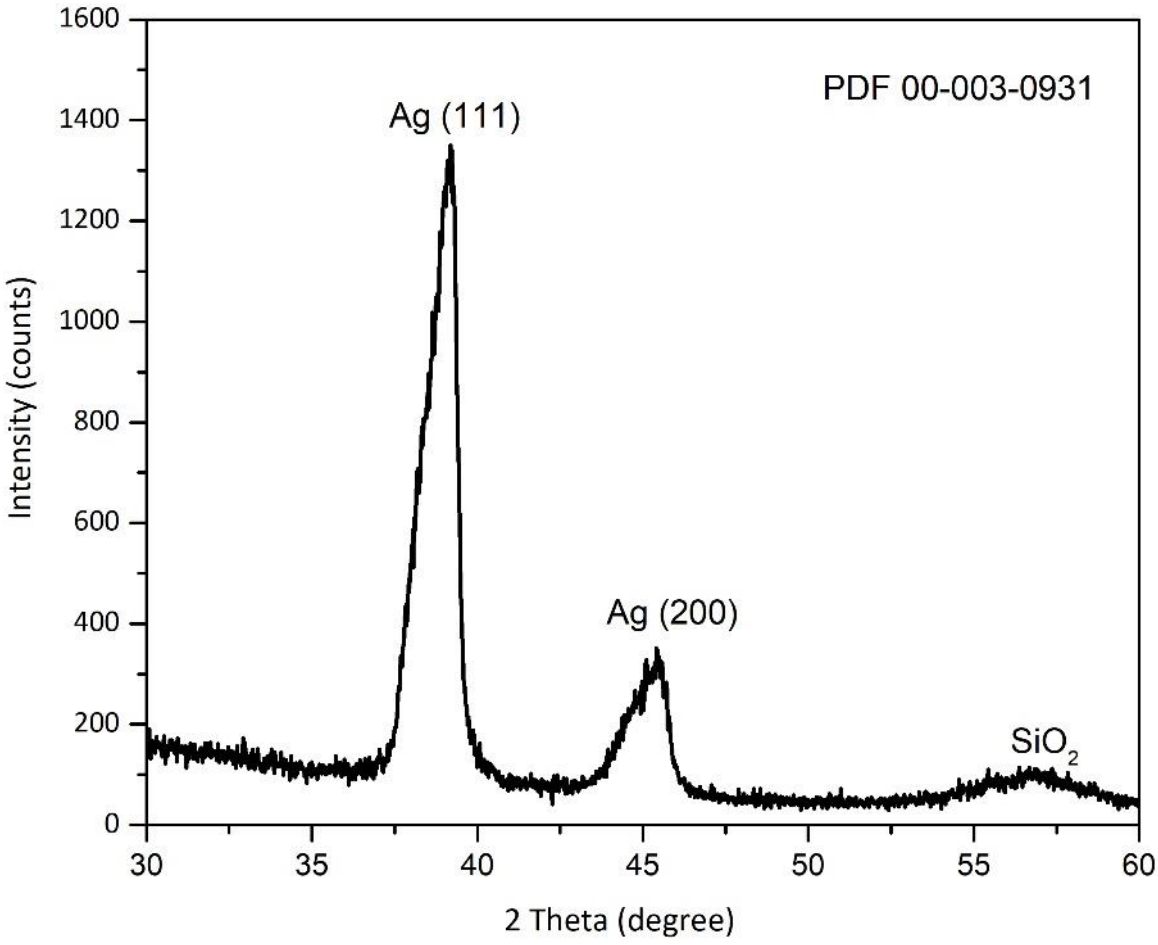

Figure 20. Grazing incidence XRD pattern of a 100 nm thick Ag nanoparticle film after 1000 cycles at 180 °C grown on a thermal SiO_2 substrate.

A 100 nm film deposited at 180 ºC was analyzed by XPS to determine the elemental composition. Surface contaminants were removed by sputtering with 3 keV argon ions to obtain the depth profile compositions (Figure 21). Composition of the film at the vertical line in Figure 21 is summarized in Table 3. After 1.0 min of 3 keV argon ion sputtering, the bulk of the film is reached, and the film consisted of 62% Ag, 15% Si, 21% O, and 2% C. The N concentration is

below the detection limits (<1%) of XPS analysis. XPS is a surface-sensitive technique. Detection of SiO_2 substrate supports the island-type growth observed. SEM images showed Ag nanoparticle growth on SiO_2 substrates. Therefore, the SiO_2 substrate is open to the surface. Hence, Si and O were also detected at the surface and bulk.

Table 3. Composition (in atomic percent) of a 100 nm thick Ag metal film grown with **1** (3 s pulse) and DMH (0.1 s pulse) on SiO_2 for 1000 cycles, as evaluated by XPS.

	Composition (at.%)
Ag 3d	62
Si 2p	15
O 1s	21
C 1s	2

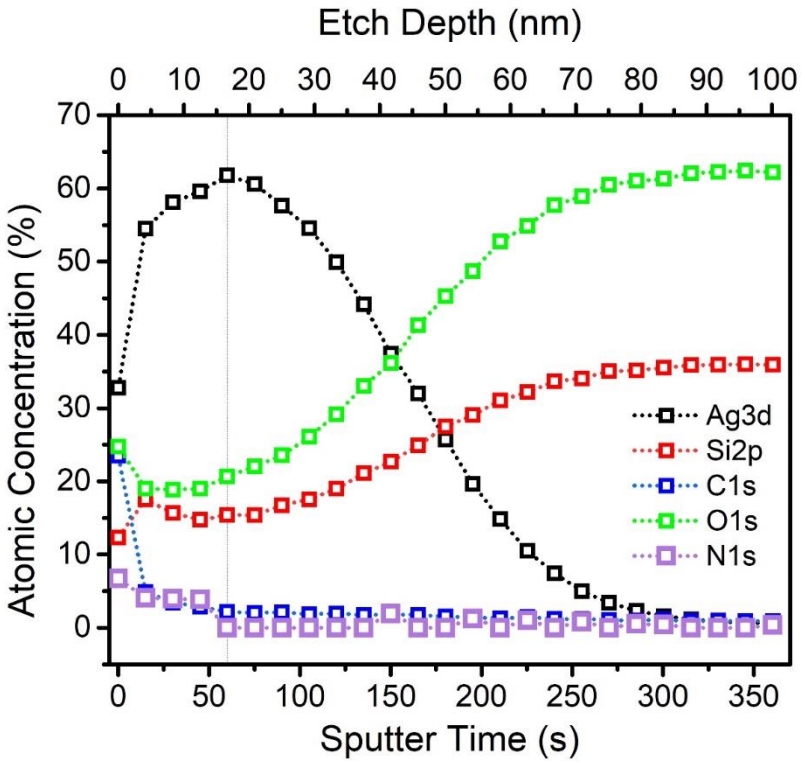

Figure 21. XPS depth profile of a 100 nm thick Ag film deposited at 180 °C.

The $Ag3d_{5/2}$ and $Ag3d_{3/2}$ binding energies for silver nanoparticles appeared at 368.2 and 374.3 eV, respectively, (Figure 22 (a)) and are in a good agreement with previously reported

assignments for bulk silver metal values.[100-102,115,143-152] XPS binding energies can be influenced by silver nanoparticle size, where reported binding energies of particulate films have shifted to higher values compared to the bulk.[153-154] The Si 2p binding energy at the surface and bulk is 103.7 eV, which corresponds to silicon in SiO_2 (Figure 22 (b)).[150,155] The O 1s ionization at 533.2 eV in the bulk after sputtering can be assigned to oxygen in SiO_2 (Figure 22 (c)).[155] A shoulder peak at 530.8 eV in the O 1s ionization may be due to the presence of silver oxides on the surface.[156] The C 1s ionization intensity before sputtering is very strong due to surface contamination (Figure 22 (d)). Adventitious carbon was set to the binding energy of 284.8 eV as the reference.[155] The binding energies at 286.7 and 288 eV are attributed to chemical states of C-O-C and O-C=O, respectively.[157] Overall, the absence of N and F content in the films rules out incorporation from the ligands present in the precursor molecules.

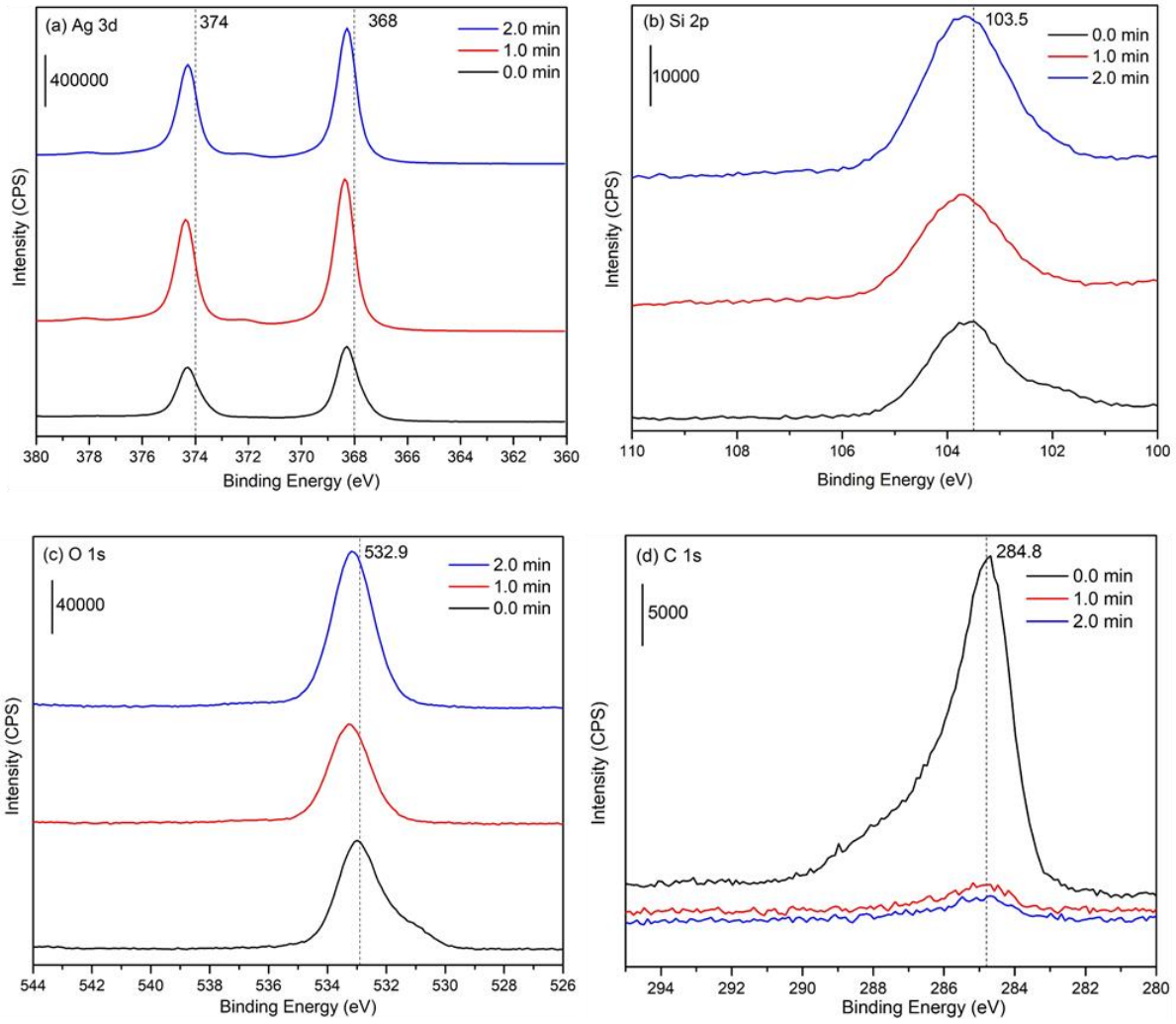

Figure 22. Ionization regions of a 100 nm thick Ag film deposited at 180 °C (a) Ag 3d (b) Si 2p (c) O 1s (d) C 1s.

2.3 Conclusions and Future Directions

Herein, thermal ALD of Ag metal films using **1** and 1,1-dimethylhydrazine was reported. Precursor **1** has been used as a single-source precursor to deposit Ag films on Si substrates by a low-pressure CVD method at the temperatures between 250-350 °C.[115] Herein, **1** and 1,1-dimethylhydrazine were used to deposit Ag metal on several substrates, including Si, SiO_2, Co, TiN, Cu, Ru, and Pt even at 180 °C. The use of the highly thermally stable and volatile silver

pyrazolate precursor **1** gave nanoparticle growth on SiO_2 substrates. The films consisted of discontinuous Ag nanoparticles, which is a similar morphology compared to previous Ag metal thermal ALD processes.[98-102] Self-limited growth was observed for **1** and 1,1-dimethylhydrazine on SiO_2 substrates, with a saturative growth rate of ~1.0 Å/cycle at 180 ºC. The growth rate of this process is higher than most other ALD processes reported. Previously reported plasma and thermal ALD processes offered growth rate ranges from 0.16-1.2 Å/cycle at different deposition temperatures.[64,95-102] A plot of growth rate versus substrate temperature showed an ALD window of 170 to 220 °C. The as-deposited films were crystalline. XPS analysis confirmed the deposition of silver metal on the SiO_2 substrate with ~2% carbon incorporation. After 1000 cycles, nanoparticle growth was observed on the SiO_2 substrate. However, nanoparticles with different sizes observed at 1000 cycles due to the coalescence of the nanoparticles. Therefore, as a future step, the number of deposition cycles can be increased to observe continuous nucleation to produce Ag thin films rather than nanoparticles. Selection of the substrate may also be a significant factor in Ag metal depositions. Ag atoms migrate on the substrate surface even at room temperature until they find an energetically favorable nucleation site. Substrates with higher surface energies than Ag act as wetting layers, thereby increasing the Ag nucleation. Therefore, the use of noble metal substrates such as Ru or Au might provide a strong bond between silver atoms and the substrate surface, which can minimize the Ag migration on the substrate. This approach may lead to the formation of a continuous film rather than nanoparticles. As another future step, depositions can be carried out on Ru and Au substrates to observe substrate effects on nucleation.

2.4 Experimental Section

Film Deposition. A Picosun R-75 SUNALE ALD reactor was used for the film deposition experiments. Ultrahigh purity nitrogen (99.999%, purchased from Air-gas) was used as the carrier

and purge gas. During the depositions, the chamber pressure was 4-5 Torr. Precursor **1** was synthesized according to a literature procedure[141-142] and was purified by sublimation at 130 °C/0.2 Torr. 1,1-Dimethylhydrazine reducing agent was purchased commercially and was used without further purification. Precursor **1** was delivered in a Picosolid booster at 157 °C, while 1,1-dimethylhydrazine was delivered with a vapor-draw bubbler at room temperature. Substrate temperatures were varied from 160 to 240 °C. Film growth experiments were conducted using a range of pulse lengths for **1** and 1,1-dimethylhydrazine to determine the degree of saturation. Initial depositions were carried out on various substrates such as SiO_2, Si, Cu, Pt, TiN, Ru, and Co. Ag metal films were deposited on SiO_2 substrates (100 nm thick) at 180 °C according to the sequence **1** (3.0 s)/N_2 purge (10.0 s)/1,1-dimethylhydrazine (0.1 s)/N_2 purge (5.0 s).

Film Characterization. Cross-sectional film thicknesses and morphologies were measured using SEM collected on a JEOL-6510LV scanning electron microscope. XRF measurements were performed before and after the deposition using an Oxford Instruments Maxxi 6 instrument. The Ag L_α intensity (2.230-4.140 KeV) was determined after 15 s measurements at 45 kV with a 1 mm collimator. XRD patterns were collected in the grazing incidence mode on a Bruker D8 Advance diffractometer using Cu Kα radiation. XPS data were collected with a Thermo Fisher Scientific Nexsa XPS system equipped with a monochromatic Al source (spot size 400 mm, 3000 eV Ar ion sputtering in monatomic mode, and $<1.0\times10^{-9}$ mbar working pressure). TGAs of **1** and **2** were performed using a TA Instruments SDT 2960 simultaneous with a ramping rate of 10 °C/min. The melting points and thermal decomposition temperatures for **1** and **2** were determined using an Electrothermal-IA 9000 series melting point apparatus with a heating rate of 10 °C/min.

CHAPTER 3
SYNTHESIS AND CHARACTERIZATION OF HIGHLY THERMALLY STABLE N-HETEROCYCLIC CARBENE SILVER PYRAZOLATE PRECURSORS

3.1 Introduction

Coinage metal (Cu, Ag, and Au) pyrazolate complexes have been widely discussed due to their interesting structural arrangements and fascinating properties.[142,158-161] In silver pyrazolate complexes, the formation of trimeric structures is preferred even with bulky substituents on the pyrazole ring, with tetramers such as $[Ag(3,5\text{-}tBu)_2Pz]_4$ being very rare.[162] This preference may be due to the size of the silver ion, which is the largest among the group of coinage metals. Also, the directional nature of the pyrazolate nitrogen atom lone pairs may favor trimers. The covalent radii of Cu(I), Ag(I), and Au(I) are 1.11, 1.33, and 1.25 Å, respectively.[142] Most of the silver pyrazolates contain close Ag-Ag contacts, which are called "argentophilic interactions." Argentophilic interactions are weak bonding interactions between metal cations with "close-shell" electronic configurations.[163-164] Argentophilic interactions are weaker than most covalent and ionic bonds but are stronger than the van der Waals bonds, and are comparable to the strength of typical hydrogen bonds. Argentophilic interactions exist when Ag-Ag distances are shorter than twice the van der Waals radius for the Ag atom (3.44 Å).[165] These interactions arise primarily due to dispersive forces, which are strengthened by the relativistic effect in heavier elements. Dispersion forces are temporary attractive forces that result from temporary dipoles occuring in adjacent atoms. Silver 4d orbitals experience some relativistic expansion while 5s orbitals undergo contraction. The relativistic effects increase the distance of the 4d orbital from the nucleus of the atom and decrease the distance of the 5s orbital. Therefore, temporary dipoles can form in d orbitals, and electrostatic bonding interactions are possible.

As ALD precursors, monomers are preferred due to their lower molecular weights and better volatilities. This chapter discusses the use of N-heterocyclic carbenes (NHCs) as strong Lewis bases to synthesize monomeric silver pyrazolates. In organometallic chemistry, the preparation and use of NHC ligands is currently an important topic.[166-168] NHCs are strong two-electron σ-donors that can coordinate more strongly to transition metals than phosphine ligands.[168] In the field of transition metal catalysis, complexes containing NHCs often show increased stability and reactivity relative to their phosphine analogs.[166-167,169-171] As a neutral donor ligand, NHCs provide better stability for monomeric Ag(I) complexes when compared with phosphine ligands.[172] In phosphines, the substituents have significant effects on both the electronic and steric properties of the ligand.[168] Steric properties of carbenes are determined by modifying the groups on the N atoms, while electronic properties are altered by functionalizing the diazole ring. NHCs such as imidazol-2-ylidenes and imidazolidin-2-yli-denes are strong σ-donors and weak π-acceptors (Chart 6).[173-174] In 1993, the first homoleptic carbene-silver complex was isolated.[175] Several Ag pyrazolate complexes containing NHCs have also been reported.[176-178]

Chart 6. NHCs (a) imidazol-2-ylidenes and (b) imidazolidin-2-yli-denes.

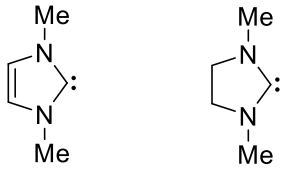

(a) (b)

This chapter reports the syntheses, structures, and precursor properties of a series of dimeric, monomeric, and tetrameric Ag pyrazolate complexes. The trinuclear Ag(I) complexes containing fluorinated pyrazolates, **1** and **2**, were used as starting materials due to their high

volatility and thermal stability. Three different five-membered ring NHCs, in which the nitrogen atom substituents were Me, Et, and iPr, and a saturated five-membered ring NHC with *tert*-butyl groups on the nitrogen atoms were used (Chart 7). Saturated NHCs show improved volatility over unsaturated NHCs in previously reported NHC-Cu complexes.[179] Increased volatility could be due to the lack of a π-electron system and non-planarity in saturated carbenes. Thus, it is essential to explore saturated carbene complexes as well. Reactivity of the monomeric precursors was also investigated using different co-reactants such as aqueous hydrazine, 1,1-dimethylhydrazine, formic acid, and alcohol.

Chart 7. N-heterocyclic carbenes (a) ***iPr2*NHC** (b) ***Et2*NHC** (c) ***Me2*NHC** (d) ***tBu2*NHC**.

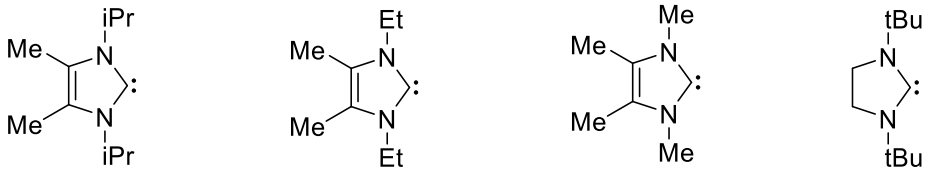

(a) (b) (c) (d)

3.2 Result and Discussion

Synthetic Aspects. Three different types of unsaturated NHCs, where the nitrogen atom substituents, Me, Et, or iPr, were chosen, as shown in equation 1. A saturated NHC with *tert*-butyl groups on the nitrogen atoms was also selected (eq 2). These ligands were prepared by reported methods.[180-181] Treatment of **1** and **2** with three equivalent of the carbenes afforded **3**-**8**, **9**·Et_2O, and **10** as colorless crystalline solids in 10-81% yields (equations 1 and 2). Selected reactions were also carried out in different solvents such as diethyl ether, THF, and toluene. Hexane was used as the solvent to perform all of the syntheses because of the high reaction yields obtained. The air, moisture, and light sensitivity of **3**-**8**, **9**·Et_2O, and **10** were tested by keeping the crystalline

materials in ambient air for 1-2 days. The isolated crystals were all stable to ambient atmosphere.

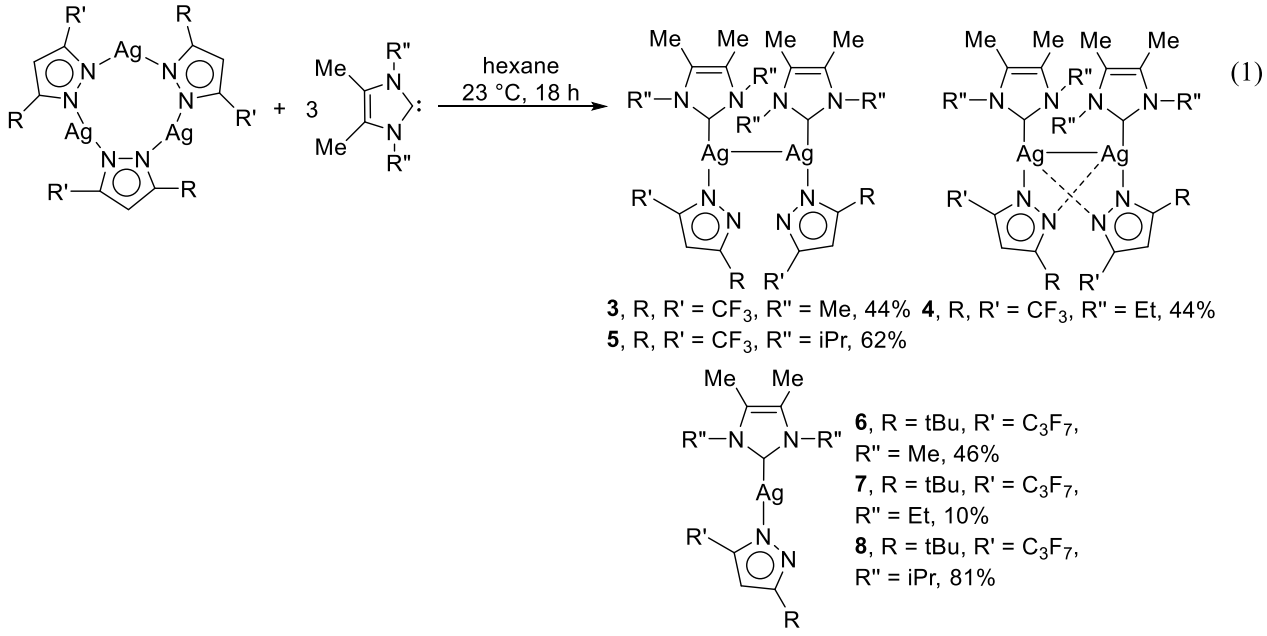

(1)

3, R, R' = CF_3, R" = Me, 44% **4**, R, R' = CF_3, R" = Et, 44%
5, R, R' = CF_3, R" = iPr, 62%

6, R = tBu, R' = C_3F_7, R" = Me, 46%
7, R = tBu, R' = C_3F_7, R" = Et, 10%
8, R = tBu, R' = C_3F_7, R" = iPr, 81%

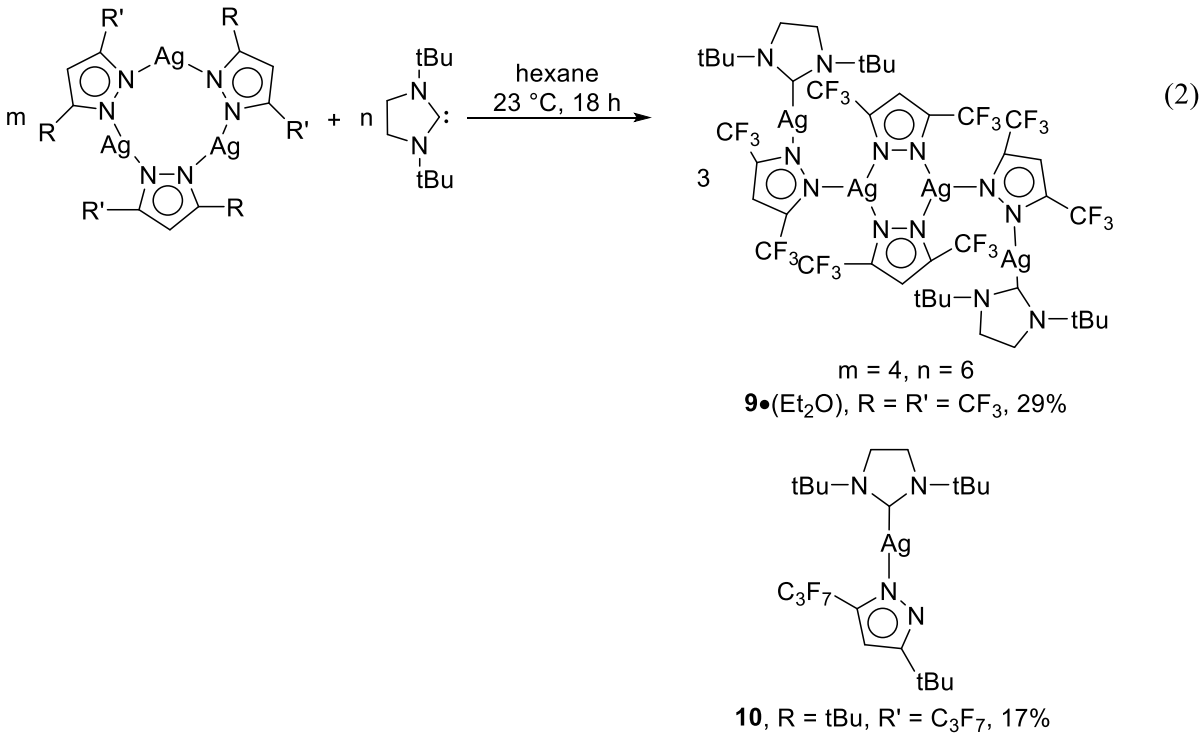

(2)

m = 4, n = 6
9•(Et_2O), R = R' = CF_3, 29%

10, R = tBu, R' = C_3F_7, 17%

Complexes **3**-**8**, **9**·Et_2O, and **10** were characterized by X-ray structure determinations and spectral and analytical techniques. X-ray crystal structures of **3**-**5**, **8**, **9**·Et_2O, and **10** were determined. The solid state structures exhibit considerable diversity, and are described below. All of the complexes are diamagnetic and were subjected to ^1H and $^{13}C\{^1H\}$ NMR analyses. The ^1H NMR spectrum of crystalline **9**•(Et_2O) showed resonances for the diethyl ether solvate, with the correct integration for one diethyl ether per molecule of **9**. In spite of the diverse solid state structures, the NMR spectra of all complexes showed one type of pyrazolate and carbene ligand at 23 °C. This is not surprising for **3**, **5**-**8**, and **10**, since one type of pyrazolate and carbene ligand would be expected if their solid state structures are maintained in solution or if the weak silver-silver interactions lead to monomers in solution. The observation of one type of $(CF_3)_2$pz ligand in **4** suggests either a monomeric structure in solution or a dimer in which the asymmetric Ag-N bonds undergo rapid site exchange. Similarly, **9**•(Et_2O) contains two different types of $(CF_3)_2$pz ligands in the solid state, so observation of only one type of $(CF_3)_2$pz ligand resonance suggests rapid ligand site exchange at 23 °C or a different solution structure. The carbene carbon atom resonances in the $^{13}C\{^1H\}$ NMR spectra of **3**, **4**, **5**, **6**, **8**, and **9**•(Et_2O) were observed as singlets in the range of 170.03-177.43 ppm. No C-^{107,109}Ag coupling was observed, suggesting rapid exchange of the carbene ligands at 23 °C.[173,182-186] In the case of **7** and **10**, the carbene carbon atom signals were not observed, in spite of concentrated samples and long collection times. These signals may be very broad, perhaps due to intermediate exchange rates on the NMR time scale. The carbene carbon atom resonance has not been observed in several previous silver complexes.[173,184-185]

X-Ray Crystal Structures. The X-ray crystal structures of **3**-**5**, **8**, **9**•(Et_2O), and **10** were obtained to determine the solid state configurations. Crystallographic data are summarized in

Tables 4 and 5. Selected bond distances and angles are shown in Tables 6 and 7. Figure 23-28 shows representative perspective views of **3**-**5**, **8**, **9**•(Et_2O), and **10**. There is a large amount of structural diversity, especially considering the similarities among the ligands. Complexes **3**-**5** crystallize as dimers, with variable Ag-Ag distances, **8** and **10** are monomeric, and **9**•(Et_2O) forms a tetramer with a bridging pyrazolate core and only two NHC ligands.

Complex **3** contains one pyrazolate ligand and one NHC ligand, with an Ag-Ag distance of 3.391 Å (Figure 23). This distance is shorter than twice the van der Waals radius for the Ag atom (3.44 Å),[165] and is thus consistent with the presence of an argentophilic interaction.[163] The N1-Ag1-C6 vectors within the dimers are eclipsed and the planes of the ligand 5-membered rings are approximately coplanar within the dimers. The Ag1-N1 bond length is 2.097(2) Å, whereas the Ag1-N2 distance is 2.906 Å. The latter distance is within the sum of the van der Waals radii for Ag and N (~3.27 Å[165,187]), so very weak bonding may be present. These asymmetric Ag-N distances and the Ag1-N1-N2 angle of 112.9(1)° are consistent with η^1-pyrazolate coordination. The Ag1-C6 bond length is 2.066(3) Å and the N1-Ag1-C6 angle is 167.53(7)°. Within the dimeric unit, there is a close contact between Ag1 and C6' of 3.080 Å, which is within the van der Waals radii of Ag and C atoms (3.42 Å).[165,187] This close contact appears to arise from an electrostatic interaction between the positively polarized C atom of the NHC ligand and the filled d orbitals on the Ag ion. Structurally similar dimers of the formula $[AgX(NHC)]_2$ (X = F, Cl, Br, I) have been studied theoretically, and have calculated Ag-Ag distances that range from 3.04 to 3.61 A.[188] The $[AgX(NHC)]_2$ complexes adopt eclipsed head-to-tail X-Ag-C vectors similar to that observed in **3**, which was proposed to arise from electrostatic interactions between the X and NHC ligands within the dimers.[188] The eclipsed head-to-tail geometry in **3** may arise from similar electrostatic interactions between pyrazolate and NHC ligands within the dimer. However, the N1-C6 distance

is 3.668 Å, which is larger than the van der Waals radii of N and C (3.25 Å[187]). Weak intermolecular and intramolecular N-H•••H-C contacts are present in the lattice of **3**.

There are three independent molecules in the unit cell of **4**. A perspective view of the dimer containing Ag1A and Ag2A is shown in Figure 24. The dimers in **4** consists of two η^2-pyrazolate ligands, with an NHC ligand coordinated to each silver ion. The Ag-Ag distances in **4** are 3.0303(9), 3.067(1), and 3.068(1) Å. These values are considerably shorter than those in **3**, due to the bridging pyrazolate ligands that hold the silver atoms in closer proximity. The Ag-N distances are 2.159(7) (Ag1A-N31A), 2.408(7) (Ag2A-N32A), 2.511(7) (Ag1A-N41A), and 2.226(7) Å (Ag2A-N42A). These distances are much longer than the Ag-N distances in **3**, due in part to the silver coordination number of three in **4** versus two in **3** (ignoring the Ag-Ag interactions). Each pyrazolate ligand in **4** also has asymmetric Ag-N bond lengths to the silver ions, with Ag-N bond distance differences of 0.249 and 0.285 Å in the dimer containing Ag1A and Ag2A. This asymmetry may be caused by steric crowding around the silver ions and by weaker Ag-N bond energies in the three-coordinate silver ions. The Ag1A-C11A and Ag2A-C21A bond lengths are 2.078(8) and 2.090(8) Å, respectively, which are close to the corresponding value in **3**. Excluding the Ag-Ag interactions, the sum of the bond angles about Ag1A (355.9°) and Ag2A (355.5°) are close to 360°, consistent with trigonal planar geometry about each silver ion. With regard to the other two independent molecules in the unit cell, the dimer containing Ag1C and Ag2C is close structurally to the dimer containing Ag1A and Ag2A, with similar Ag-N bond lengths, asymmetric Ag-N bond lengths within each pyrazolate ligand, and identical Ag-C bond lengths within experimental error. However, the dimer containing Ag1B and Ag2B has a slightly different structure than the other two. Most notably, bonding of the pyrazolate ligands to the silver ions is highly asymmetric (Ag1B-N31B 3.558, Ag2B-N32B 2.076(7), Ag1B-N41B 2.115(7), Ag2B-

N42B, 2.730 Å). Thus, the silver ions in the dimer containing Ag1B and Ag2B are closer to two coordinate, whereas the silver ions in the other two dimers are three coordinate. The Ag1B-C11B and Ag2A-C21B bond lengths are 2.070(8) and 2.051(8) A, which are similar to the values in **3** and the other two dimers. The origins of the different structures in the dimer containing Ag1B and Ag2B are not clear, but bond length distortions involving the pyrazolate ligands may be low energy.

Complex **5** adopts a dimeric structure that is similar to **3**, in that there are no bridging pyrazolate ligands and the dimer is held together by a Ag-Ag interaction with a distance of 3.1321(8) Å (Figure 25). However, unlike **3**, the N-Ag-C vectors in **5** are not eclipsed, but instead have a torsion angles that range between about 59 and 72°. These non-zero torsion angles in **5** appear to originate from steric interactions between the pyrazolate and NHC ligands across the dimer. The Ag1-N1 and Ag2-N5 bond lengths are 2.101(6) and 2.115(6) Å, respectively, which are similar to the value in **3** and shorter than the values in **4**. The Ag1-N6 and Ag2-N2 distances (3.076 and 3.202 Å, respectively) are longer than the related distance in **3**, but are still within the sum of the van der Waals radii for Ag and N (~3.27 Å[165,187]). These asymmetric Ag-N distances are consistent with η^1-pyrazolate bonding. The Ag-C bond lengths (Ag1-C6 2.072(7), Ag2-C22 2.074(6) Å) are identical to those in **3** and **4** within experimental uncertainty. The N1-Ag1-C6 and N5-Ag2-C22 angles are 174.0(3) and 171.3(2)°, respectively. These values are similar to that of **3** and are essentially linear, as expected for ideal two-coordinate geometry (ignoring the Ag-Ag interaction).

Complexes **8** and **10** have monomeric structures with very similar bond lengths and angles (Figures 26 and 28). The Ag-Ag distances (**8**, 6.514; **10**, 6.796, 6.931 Å) are much longer than twice the van der Waals radius for the Ag atom (3.44 Å)[165] and are too long to argentophilic

interactions. The Ag-N bond lengths (**8**, Ag1-N2 2.078(4); **10**, Ag1-N1 2.073(2) Å) are similar to the related values in **3** and **5** within experimental uncertainty, and are shorter than the Ag-N distances in **4**. The Ag-N distances to the second nitrogen atom in each pyrazolate ligand (**8**, Ag1-N1 2.949; **10**, Ag1-N2 2.927 Å) are long, and are similar to the corresponding distance in **3**. Accordingly, **8** and **10** are best described as containing η^1-pyrazolate ligands. The Ag1-C10 and Ag1-C11 distances in **8** and **10** are 2.063(5) and 2.078(2) Å, respectively. These distances are identical within experimental uncertainty and are similar to the values in **3**-**5**. The N2-Ag1-C10 and N1-Ag1-C11 angles in **8** and **10** are 177.4(2) and 176.95(7)°, respectively, which are close to the 180° value expected for linear, two-coordinate Ag atoms.

Complex **9·Et₂O** crystallizes as a tetranuclear complex, as shown in Figure 27. The crystals also incorporate one molecule of diethyl ether per tetrameric unit, as described earlier. The central core of the tetramer consists of a $Ag_2((CF_3)_2pz)_2$ unit, with μ_2-pyrazolate ligands. Each Ag ion in the central core is bonded to a nitrogen atom of a pyrazolate ligand, and a Ag(NHC) fragment is coordinated to the other nitrogen atom of the pyrazolate ligand. The Ag_2N_4 core is approximately planar, and the pyrazolate planes in the outer $Ag((CF_3)_2pz)$(NHC) unit are perpendicular to the core plane. The Ag-Ag distances (Ag1-Ag1' 3.603; Ag1-Ag2 3.464 Å) are longer than twice the van der Waals radius for the Ag atom (3.44 Å)[165], and thus no argentophilic interactions are present. The Ag-N distances for three-coordinate Ag1 (Ag1-N2 2.226(1); Ag1-N4 2.216(1); Ag1'-N3 2.222(1) Å) are longer than the value for two-coordinate Ag2 (Ag2-N1 2.096(1) Å), as expected. The Ag2-N1 bond length is similar to the related values in **3**, **5**, **8**, and **10**, consistent with the two-coordinate Ag ions in these complexes. The Ag-C distance in **9•**(Et_2O) is 2.084(2) Å, which is identical within experimental uncertainty to the values in **3**-**5**, **8**, and **10**. The N1-Ag2-C11 angle is 178.56(5)°, which is expected for a two-coordinate Ag atom. The angles about Ag1 range from

118.8 to 122.2°, which fits with idealized trigonal planar geometry. The Ag-N-N angles for the pyrazolate ligands also encompass 118.1 to 121.5°, as expected for trigonal planar pyrazolate nitrogen atoms.

The overall structures adopted herein can be compared with previously reported silver pyrazolate complexes and selected silver complexes containing NHC ligands. Silver pyrazolate complexes containing chelating NHCs have been reported, although the structures are not similar to those observed herein.[176-178,189] Ag-N bond lengths in these complexes range from about 2.08 to 2.10 Å, and Ag-C bond lengths lie between 2.05 and 2.10 Å. These distances are very similar to those observed herein, with the exception of the longer Ag-N distances in **4**. Complexes **3** and **5** adopt dimeric structures with essentially linear N-Ag-C vectors that are either eclipsed (**3**) or twisted (**5**) across the dimers. Dimers with head-to-tail eclipsed C-Ag-X vectors are predicted theoretically in $[Ag(NHC)X]_2$, where X = F, Cl, Br, I.[188] The eclipsed structures in these dimers was attributed to electrostatic ligand interactions across the dimers. Complexes of the formula $[Ag(NHC)Cl]_n$ (n = 1, 2) adopt structures with twisted N-Ag-C vectors across dimers or form monomers, with moderate size NHC ligand substituents.[190-191] Formation of monomers occurs with large NHC substituents.[190] It is likely that the formation of monomeric structures observed herein for **8** and **10** is similarly driven by the steric bulk of the ligands. Complex **5** adopts a dimeric $Ag_2(pyrazolate)_2$ core, with μ_2-pyrazolate ligands, and then each silver atom is bonded to an NHC ligand. The crystal structures of very similar complexes of the formula $Ag_2(pyrazolate)_2L_2$ have been reported, where L is a neutral donor ligand.[192-196] The tetrameric structure of **9**•(Et_2O) contains a central $Ag_2(pyrazolate)_2$ core, with a Ag(pyrazolate)(NHC) fragment coordinate to each core Ag ion through a μ_2-pyrazolate interaction. The crystal structures of several similar tetrameric

complexes have been reported, where the silver ions in a dimeric Ag_2(pyrazolate)$_2$ core are each bonded to a Ag(pyrazolate)(NHC) unit through μ_2-pyrazolate ligands.[197]

Table 4. Experimental crystallographic data for **3**, **4**, and **5**.

	3	**4**	**5**
Formula	$C_{12}H_{13}AgF_6N_4$	$C_{14}H_{17}AgF_6N_4$	$C_{16}H_{21}AgF_6N_4$
fw	435.13	463.18	491.24
space group	$P2_1/n$	$P2_1/n$	P-1
a (Å)	7.3601(7)	9.2055(10)	10.0537(10)
b (Å)	15.0620(14)	64.620(8)	11.3296(10)
c (Å)	14.0041(13)	17.533(2)	17.3537(16)
V (Å^3)	1499.2(2)	10376(2)	1915.7(3)
Z	4	24	4
T (K)	100.1	100(2)	100.1
λ (Å)	0.71073	0.71073	0.71073
ρ_{calc} (gcm^{-3})	1.928	1.779	1.703
μ (mm^{-1})	1.412	1.230	1.116
R(*F*)[a] (%)	2.26	6.68	7.12
Rw(*F*)[b] (%)	4.85	15.96	16.52

[a] $R(F) = \Sigma||F_o| - |F_c||/\Sigma|F_o|$. [b] $R_w(F^2) = [\Sigma w(F_o^2-F_c^2)^2/\Sigma w(F_o^2)^2]^{1/2}$.

Table 5. Experimental crystallographic data for **8**, **9**·Et_2O, and **10**.

	8	**9**·Et_2O	**10**
Formula	$C_{21}H_{30}AgF_7N_4$	$C_{46}H_{58}Ag_4F_{24}N_{12}O$	$C_{21}H_{32}AgF_7N_4$
fw	579.36	1682.52	581.37
space group	Pnma	P-1	$P2_1/c$
a (Å)	22.4937(18)	10.3135(9)	12.2197(8)
b (Å)	12.5802(9)	12.0136(10)	9.8710(6)
c (Å)	8.6645(7)	14.0181(13)	20.2318(12)
V (Å^3)	2451.8(3)	1501.3(2)	2429.6(3)
Z	4	1	4
T (K)	100.1	100.1	100.1
λ (Å)	0.71073	0.71073	0.71073
ρ_{calc} (gcm^{-3})	1.570	1.861	1.589
μ (mm^{-1})	0.891	1.406	0.899
R(*F*)[a] (%)	3.94	2.57	2.59
Rw(*F*)[b] (%)	9.77	5.51	5.89

[a] $R(F) = \Sigma||F_o| - |F_c||/\Sigma|F_o|$. [b] $R_w(F^2) = [\Sigma w(F_o^2-F_c^2)^2/\Sigma w(F_o^2)^2]^{1/2}$.

Table 6. Selected bond lengths (Å) and angles (deg) for **3**, **4**, and **5**.

	Ag-N (Å)	Ag-C (Å)	N-Ag-C/N (°)	N-Ag-C (°)
3	Ag1-N1 2.097(2) Ag(1)-N2 2.906	Ag1-C6 2.066(3)	N1-Ag1-C6 167.53(7)	Ag1-N1-N2 112.9(1)
4	Ag1a-N31a 2.159(7) Ag2a-N32a 2.408(7) Ag1a-N41a 2.511(7) Ag2a-N42a 2.226(7)	Ag1a-C11a 2.078(8) Ag2a-C21a 2.090(8)	N31A-Ag1a-N41A 85.1(2) N31A-Ag1A-C11A 153.0(3) N32A-Ag2A-N42A 92.0(2) N32A-Ag2A-C21A 121.9(3) N41A-Ag1A-C11A 117.8(3) N42A-Ag2A-C21A 141.6(3)	Ag1a-N31A-N32A 114.6(5) Ag2A-N32A-N31A 108.4(5) Ag1A-N41A-N42A 106.0(5) Ag2A-N42A-N41A 116.2(5)
5	Ag1-N1 2.101(6) Ag1-N6 3.076 Ag2-N5 2.115 Ag2-N2 3.202	Ag1-C6 2.072(7) Ag2-C22 2.074(6)	N1-Ag1-C6 174.0(3) N5-Ag2-C22 171.3(2)	Ag1-N1-N2 118.7(5) Ag2-N5-N6 118.2(5)

Table 7. Selected bond lengths (Å) and angles (deg) for **8, 9**·Et_2O**,** and **10**.

	Ag-N (Å)	Ag-C (Å)	N-Ag-C/N (°)	N-Ag-C (°)
8	Ag1-N2 2.078(4) Ag1-N1 2.949	Ag1-C10 2.063(5)	N2-Ag1-C10 177.4(2)	Ag1-N2-N1 115.6(4)
9•Et_2O	Ag1-N2 2.226(1) Ag1'-N3 2.222(1) Ag1-N4 2.216(1) Ag2-N1 2.096(1)	Ag2-C1 2.084(2)	N1-Ag2-C1 178.56(5)	Ag1-N2-N1 118.09(9) Ag1'-N3-N4 119.11(9) Ag1-N4-N3 121.48(9) Ag2-N1-N2 119.41(9) N2-Ag1-N3 118.76(5) N2-Ag1-N4 122.19(5) N3-Ag1-N4 119.05(4)
10	Ag1-N1 2.073(2) Ag1-N2 2.927	Ag1-C11 2.078(2)	N1-Ag1-C11 176.95(7)	Ag1-N1-N2 115.7(1)

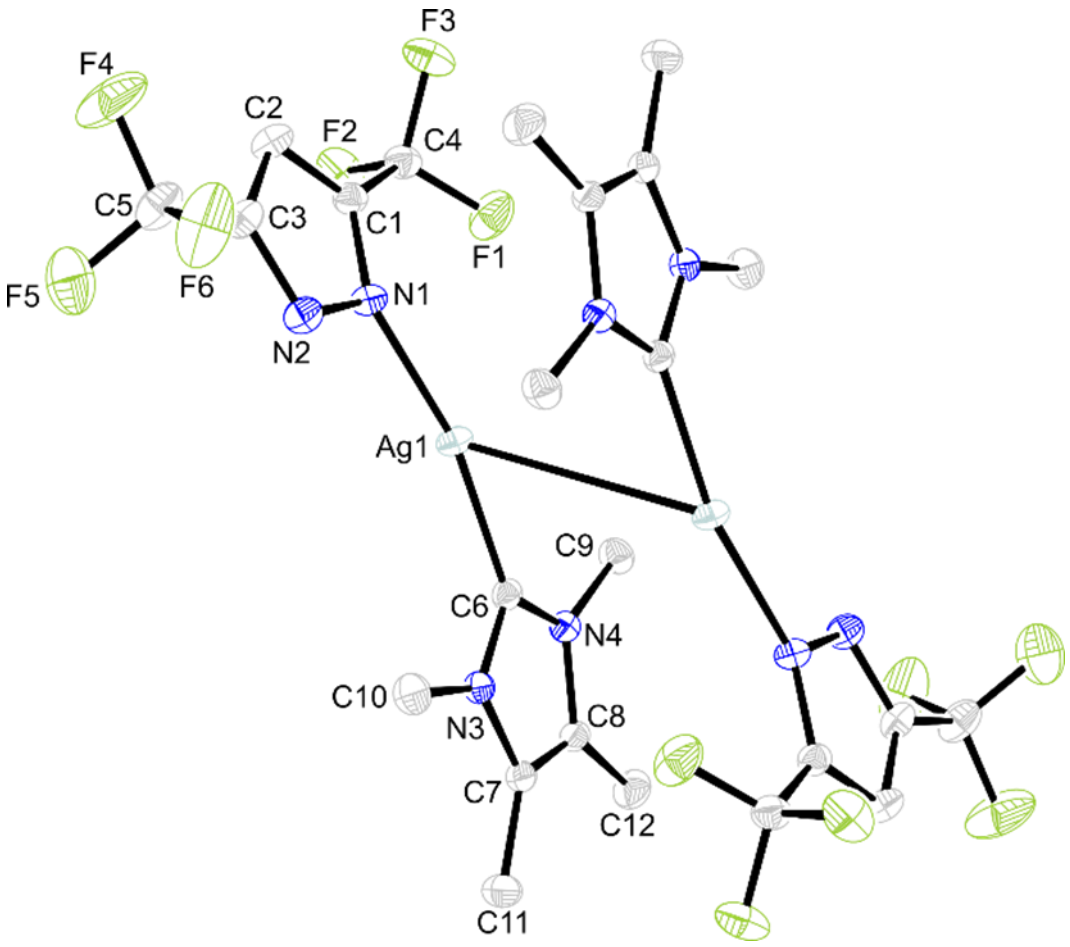

Figure 23. Perspective view of **3** with thermal ellipsoids at the 50% probability level.

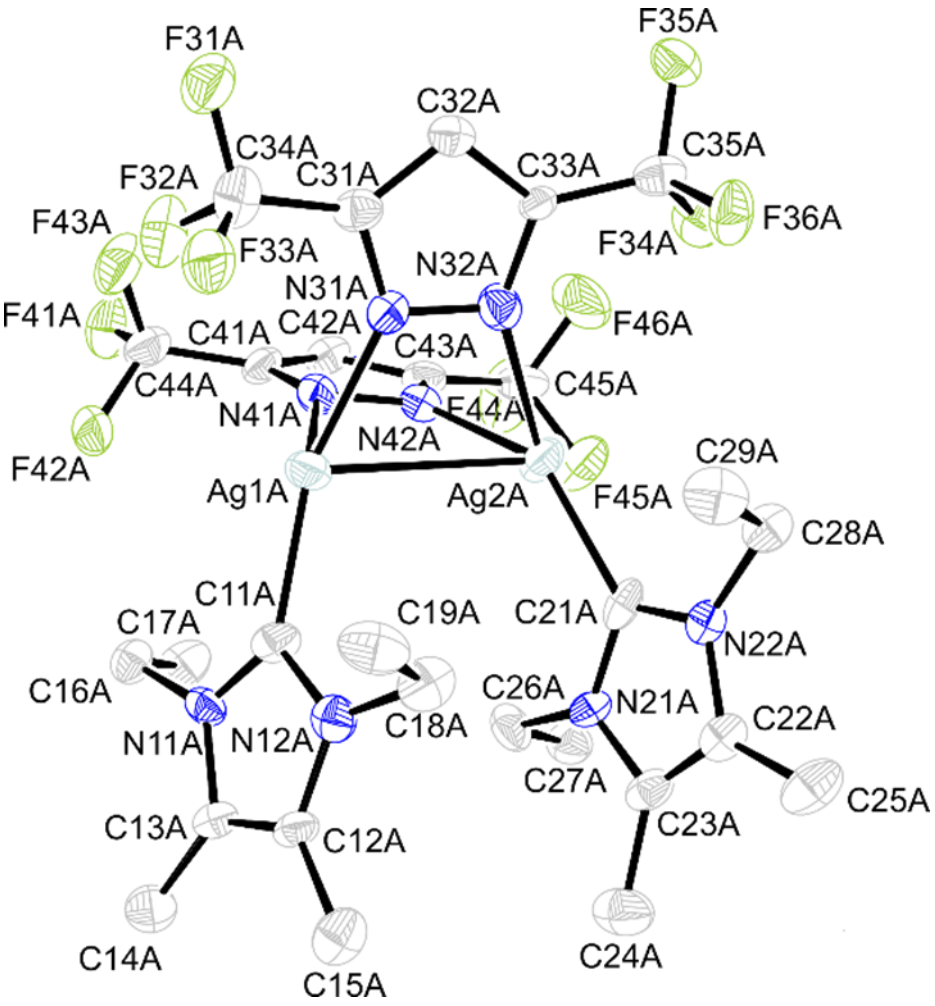

Figure 24. Perspective view of **4** with thermal ellipsoids at the 50% probability level.

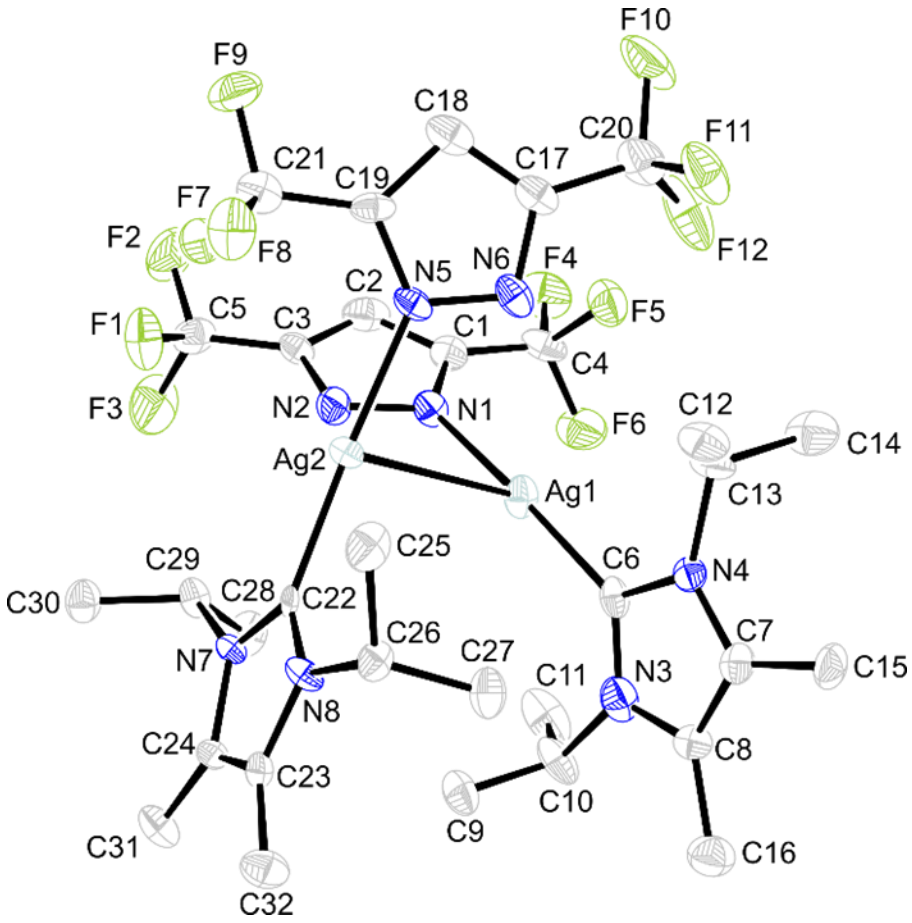

Figure 25. Perspective view of **5** with thermal ellipsoids at the 50% probability level.

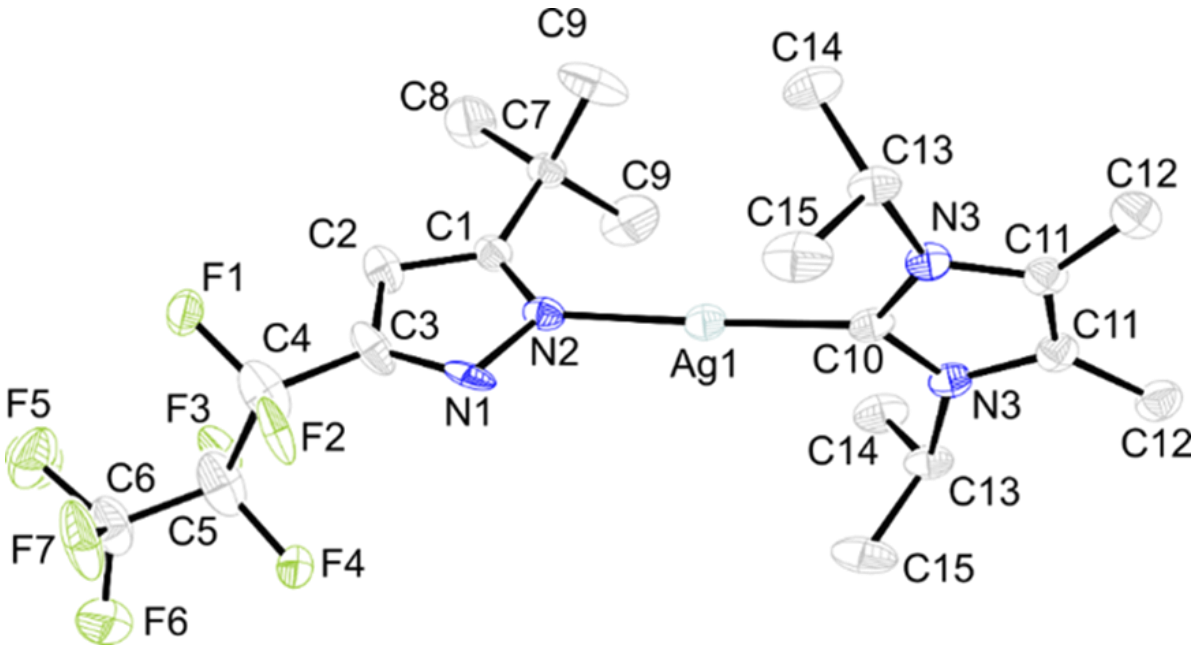

Figure 26. Perspective view of **8** with thermal ellipsoids at the 50% probability level.

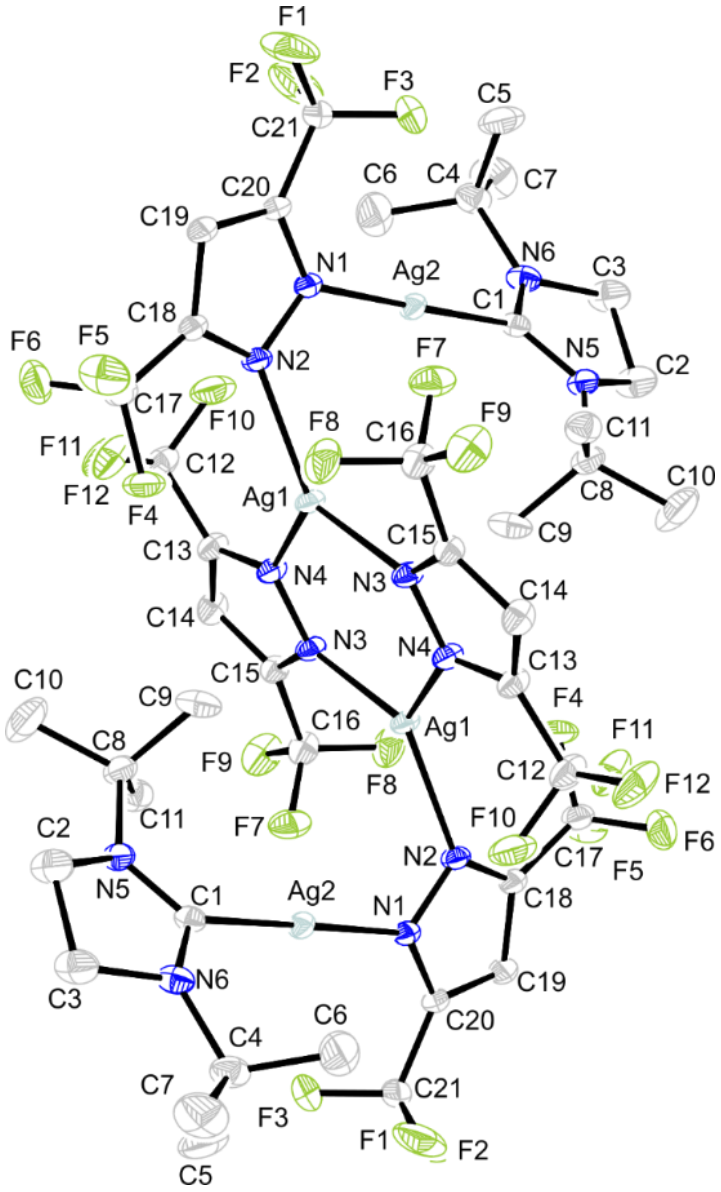

Figure 27. Perspective view of **9**·Et_2O with thermal ellipsoids at the 50% probability level.

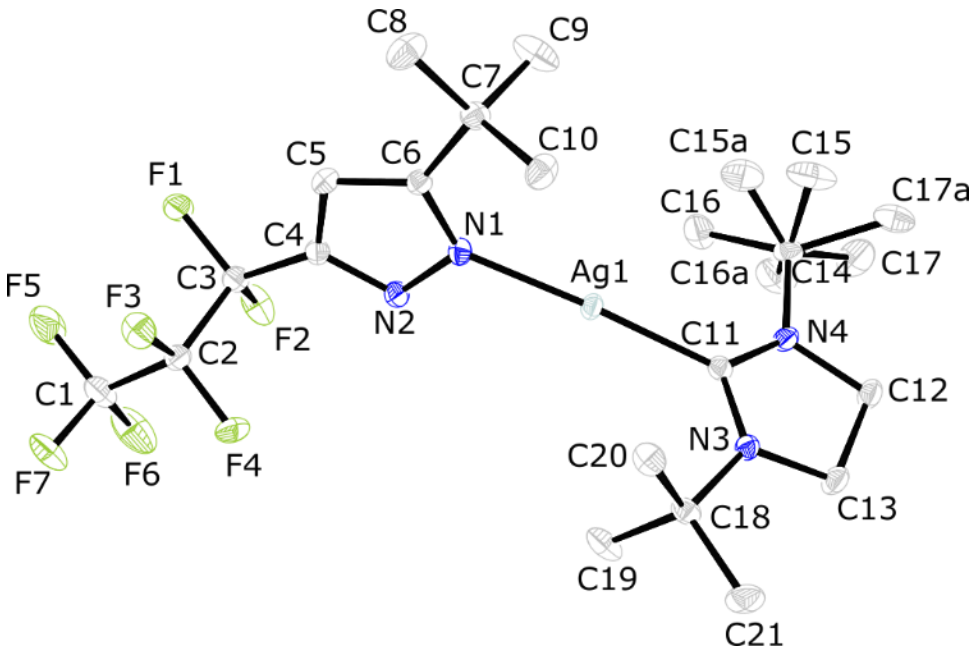

Figure 28. Perspective view of **10** with thermal ellipsoids at the 50% probability level.

To observe the behavior of **4** in the solution, a low-temperature NMR experiment was carried out at different temperatures (Figure 29). ^{1}H NMR spectra show broader resonances at low temperatures. The NMR spectra showed one type of pyrazolate and carbene ligand at 23 and -60 °C. However, at -70 °C a broad resonance at around 6.67 ppm started to appear. ^{19}F NMR spectra showed a singlet at room temperature and two different resonances at low temperatures (Figure 30). However, the intensities of the two resonances are different and not equal to 1:1, indicating two different fluorine environments. Two different complexes are possibly present at low temperatures in the solution. However, the above data do not identify the exact species that occur at low temperatures.

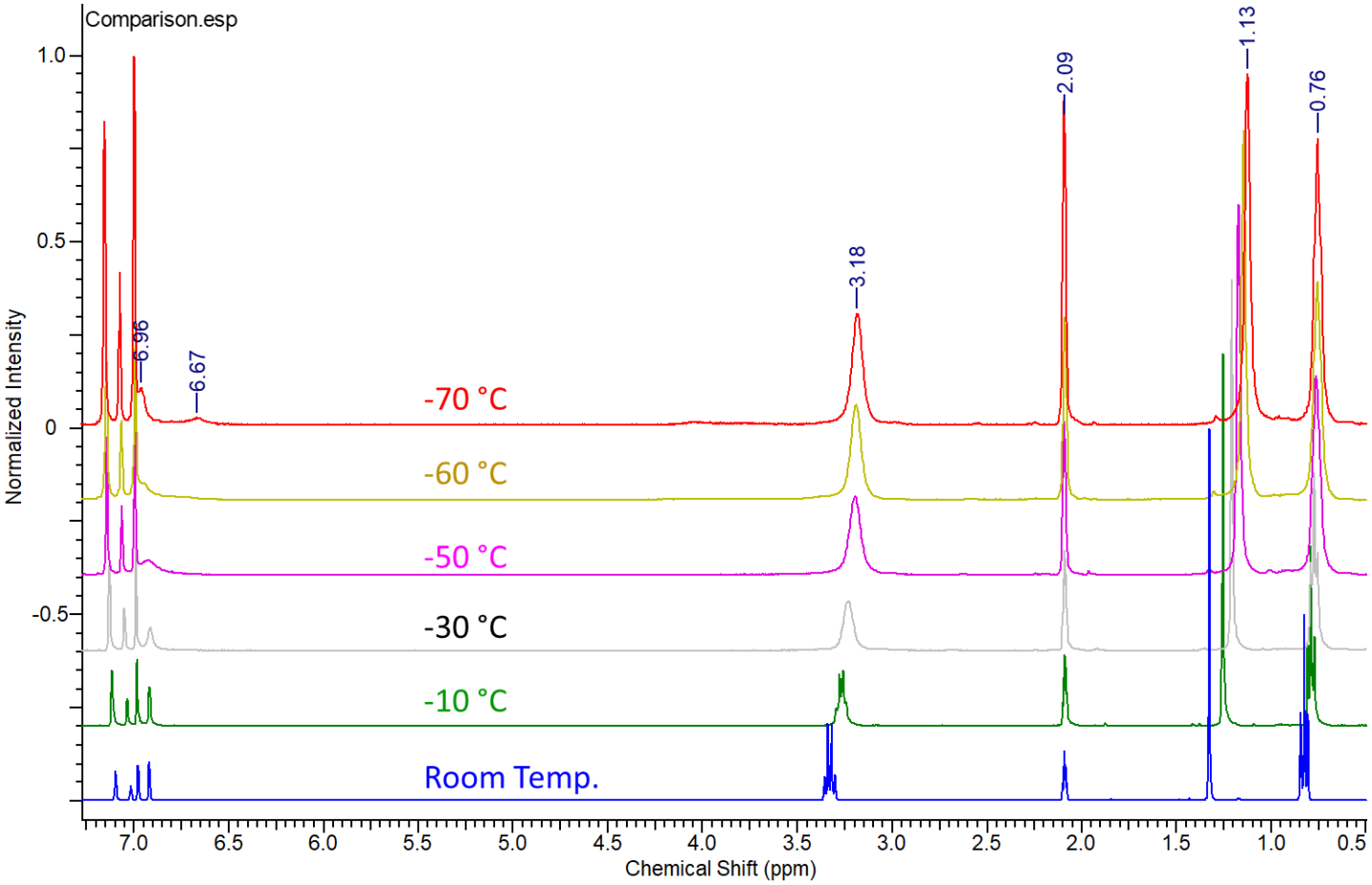

Figure 29. ^{1}H NMR spectrum of **4** at different temperatures.

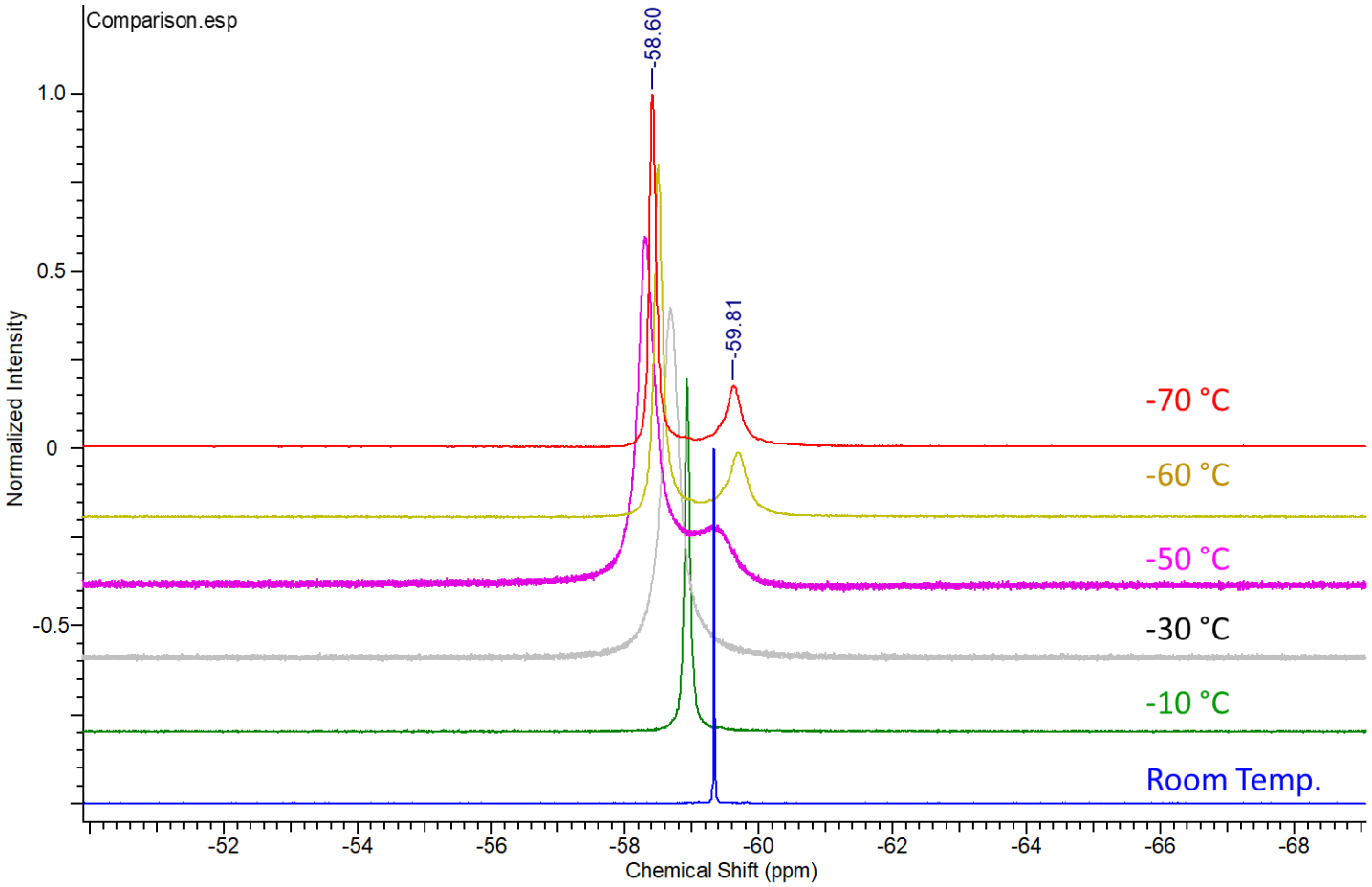

Figure 30. ^{19}F NMR spectrum of **4** at different temperatures.

Thermal Stability, Volatility, and Reactivity towards Co-Reagents. The melting points, thermal decomposition temperatures, and preparative sublimation data for **3-8**, **9**•Et_2O, and **10** are shown in Table 8. Precursors used in ALD and CVD should be liquids at the gaseous delivery temperatures, since liquids have a constant surface area, and thus constant gas phase precursor concentrations are obtained. By contrast, the surface areas of solid precursors can change depending upon loading and solids can create particles in the films. Complexes **3-6**, **8**, and **9**·Et_2O have melting points that are lower than the sublimation temperatures and are thus delivered from the liquid state. The sublimation temperatures of **3-6**, **8**, **9**•Et_2O, and **10** range from 110 to 130 °C at 0.2 Torr, which are approximately the same as those of **1** and **2** (120 and 130 °C, respectively). Interestingly, the melting points of **1** and **2** are about 105 and 65 °C higher, respectively, than the 120 to 130 °C sublimation temperatures. Accordingly, these trimeric pyrazolates sublime as solids. Importantly, **3-6**, **8**, **9**•Et_2O, and **10** sublime intact, do not lose the NHC ligands, and show undetectable (<1%) resonances for **1** and **2** in the ^1H NMR spectra of the sublimed materials. The decomposition temperatures of ALD precursors are often close to the upper limits of self-limited growth, and thus provide valuable information. As a baseline, the decomposition temperatures of **1** and **2** were 277 and 245 °C, respectively. Among **3-8**, **9**•Et_2O, and **10**, only **4** has a higher decomposition temperature than the parent trimeric pyrazolate. Complexes **3-5** and **9**•Et_2O contain $(CF_3)_2$pz ligands and have higher decomposition temperatures (200 to 233 °C) than **6-8** and **10** (160 to 200 °C), which contain (C_3F_7)(tBu)pz ligands. Thermal decomposition may involve dissociation of the NHC ligand. Since the $(CF_3)_2$pz ligand should be more electron withdrawing than the (C_3F_7)(tBu)pz ligand, the Ag ions in **3-5** and **9**•Et_2O are stronger Lewis acids than the Ag ions in **6-8** and **10**. Another possibility is that the $(CF_3)_2$pz ligand is a poorer reducing agent for the Ag ions than the (C_3F_7)(tBu)pz ligand. Interestingly, the sublimation temperatures of **1** and **2**

are 120 to 130 °C at 0.2 Torr, which are in the same range as **3-6**, **8**, **9**•Et_2O, and **10**. Since volatility generally decreases with increasing precursor molecular weight, it is possible that these trimeric complexes sublime as monomers or dimers.

Table 8. Melting points, thermal decomposition temperatures, and sublimation temperatures for **1**-**10**.

Complex	Melting Point (°C)	Decomposition (°C)	Sublimation Temperature (0.2 Torr)
1	235-238	277	130
2	184-186	245	120
3	114-117	203	130
4	96-98	293	140
5	101-102	233	120
6	107-109	180	120
7	88-91	160	decomposed
8	94-95	200	110
9•Et_2O	109-111	205	130
10	146-149	191	120

Precursor thermal properties were assessed by thermogravimetric analysis (TGA) and differential thermal analysis (DTA). Figure 31 shows the TGA traces for **1**, **3**-**5**, and **9**•(Et_2O). The related TGA data for **2**, **6**-**8**, and **10** are shown in Figure 32. Most significantly, only **1** and **2** show single step weight losses with approximately zero residual masses. The 10% weight loss temperatures were 232 and 238 °C for **1** and **2**, respectively. These temperatures approximate the 1 Torr vapor pressures at atmospheric pressure. Thus, **1** is slightly more volatile than **2**, consistent with the higher molecular weight of the latter. By contrast, **3**-**5**, **9**•(Et_2O), and **10** are much less

volatile than **1** and **2**, with 10% weight loss temperatures of >270 °C. Moreover, none of the NHC complexes evaporates completely, and instead all decompose at >300 °C to afford nonvolatile residues. Non-volatile residues in **4**, **5**, **9**·Et_2O, and **10** are roughly equal the percentage Ag in each complex (**4**, 23%; **5**, 22%; **9**·Et_2O, 26%; **10**, 19%). However, non-volatile residues in **3**, **6**, **7**, and **8** are higher than the percent of Ag in the complexes (**3**, 25%; **6**, 21%; **7**, 20%; **8**, 19%).

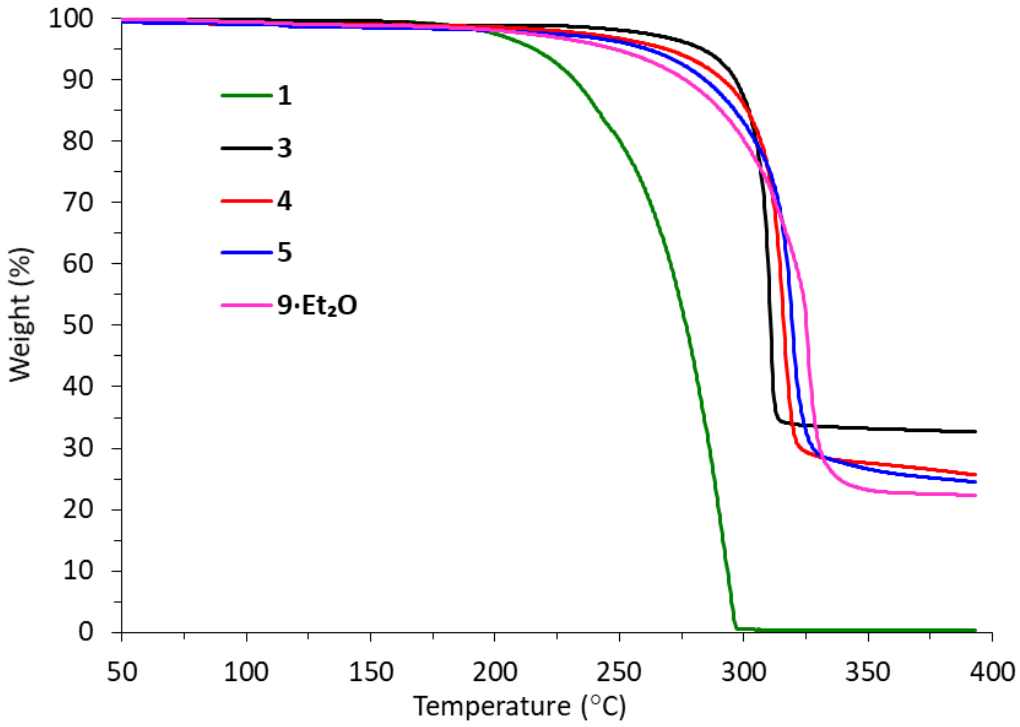

Figure 31. TGA plots of **1**, **3**, **4**, **5**, and **9**·Et_2O.

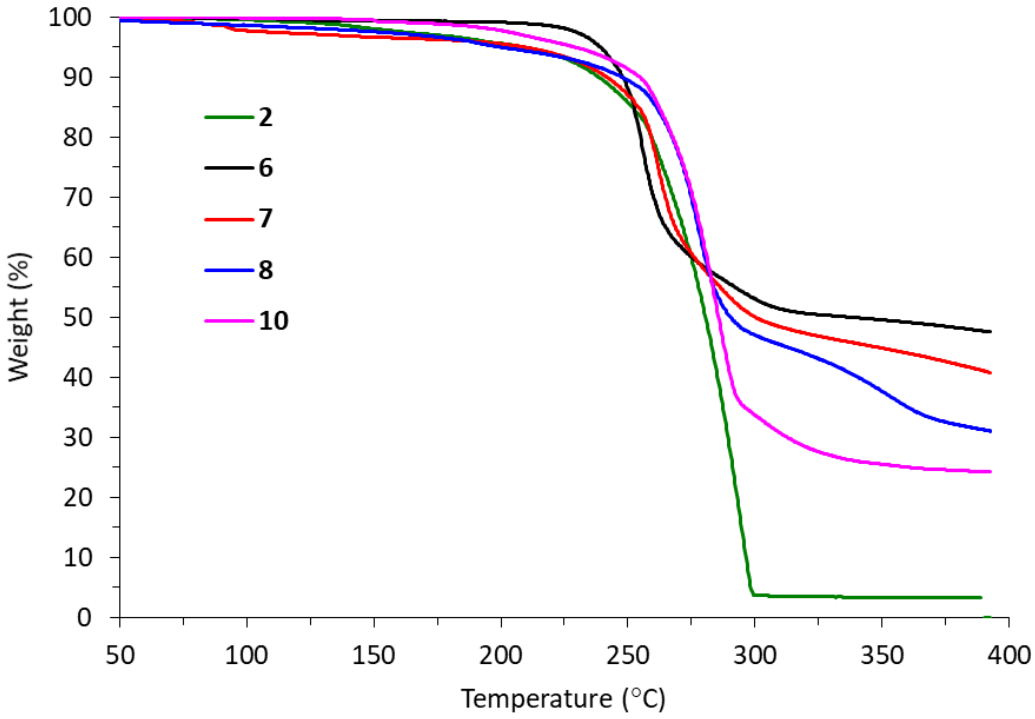

Figure 32. TGA Plots of **2**, **6**, **7**, **8**, and **10**.

To explore the reactivity of these precursors, **5** and **8** were treated with reducing co-reagents. In these reactions, a solution of **5** and **8** in toluene was treated with five equivalent of each potential reducing reactant, as listed in Table 9. The reactions that did not show any color changes or gas formation upon addition of the co-reactants were stirred at room temperature for 18 hours stirring and were then refluxed for 5 or 8 h. The solution was then cooled to room temperature and the precipitate was collected. The residue was subjected to powder XRD to verify the presence of metal. Both **5** and **8** are reactive towards several reducing agents such as aqueous N_2H_4, 1,1-dimethylhydrazine, and formic acid. Selected powder XRD patterns observed for the residues are shown in Figure 33-36. As shown, measured XRD patterns were matched to Ag metal.

Table 9. Reactivity of **5** and **8** towards reducing agents in toluene.

Reducing agent	**5**	**8**
Aqueous NH_2NH_2	Ag mirror, 23 °C, 5 min	Ag mirror, 23 °C, 5 min
Water	No reaction at 23 or 111 °C	No reaction at 23 or 111 °C
1,1-Dimethylhydrazine	Ag mirror, 23 °C, 18 h	Black solid, 23 °C, 18 h
Formic acid	Black solid, 111 °C, 1 h	Black solid, 111 °C, 1 h
$tBuNH_2$	Black solid, 111 °C, 18 h	No reaction at 23 or 111 °C
1-Propanol	No reaction at 23 or 111 °C	No reaction at 23 or 111 °C
2-Propanol	No reaction at 23 or 111 °C	No reaction at 23 or 111 °C

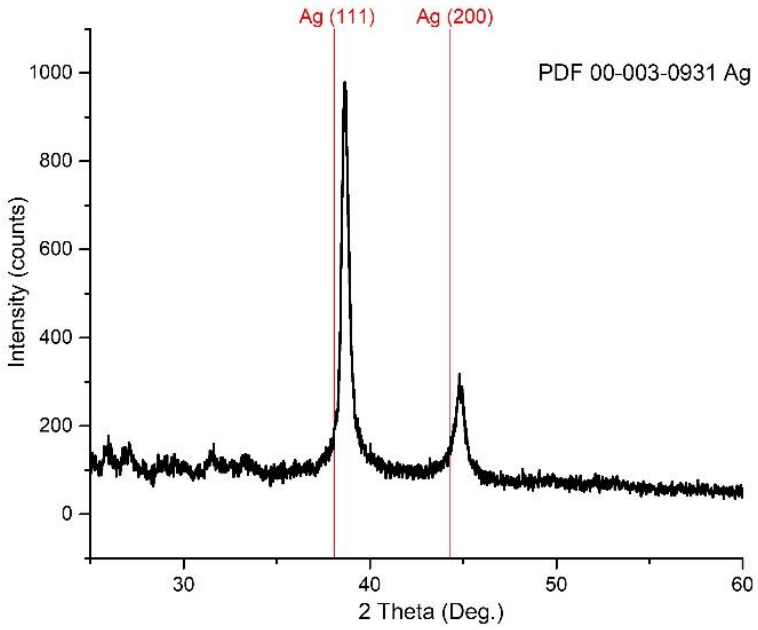

Figure 33. Powder XRD pattern from solution reduction of **5** + 1,1-dimethylhydrazine.

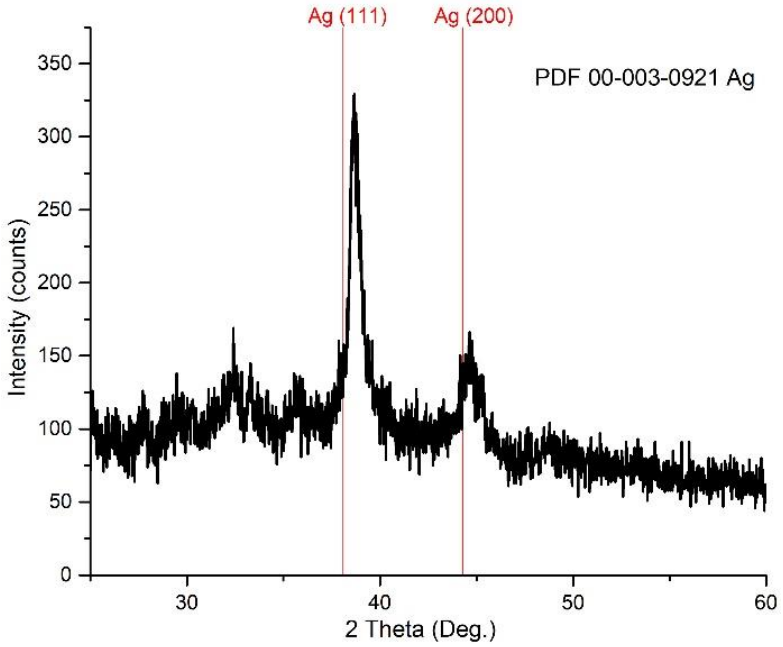

Figure 34. Powder XRD pattern from solution reduction of **5** + formic acid.

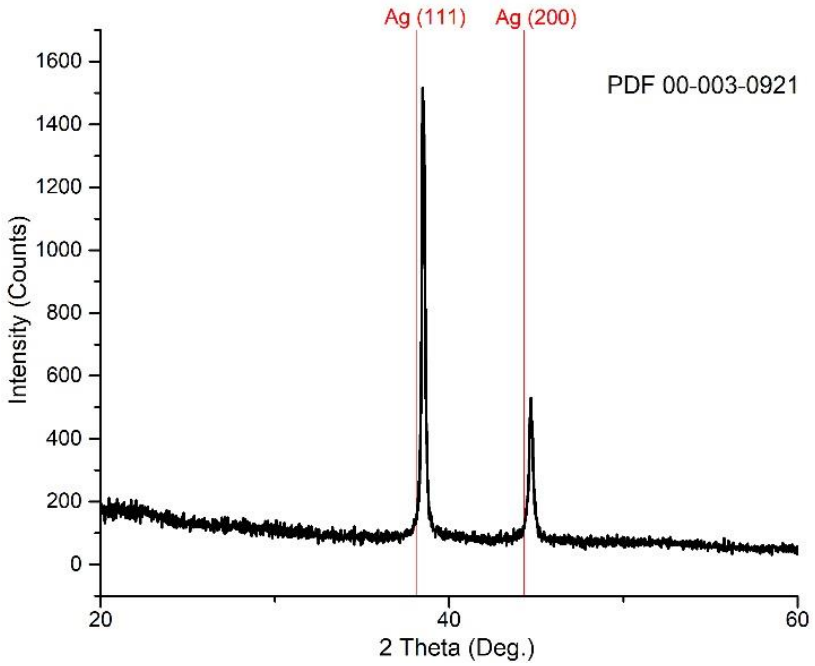

Figure 35. Powder XRD pattern from solution reduction of **5** + $tBuNH_2$.

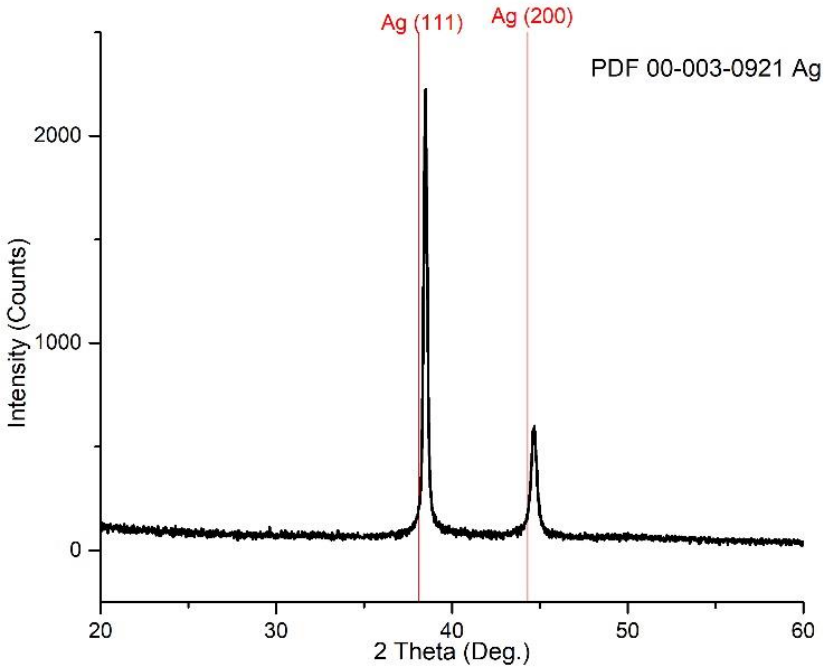

Figure 36. Powder XRD pattern from solution reduction of **8** + formic acid.

3.3 Conclusions

Chapter three discussed the use of four different types of NHCs as strong Lewis bases to synthesize monomeric silver pyrazolates. Monomeric precursors are preferred in ALD due to their lower molecular weight and better volatility. Trimers **1** and **2** were selected as parent pyrazolates because of their high volatility and thermal stability. Treatment of the trimers **1** and **2** with NHCs afforded Ag(pz)(NHC) adducts, including monomers, dimers, and a tetramer. Solid state structures showed a large amount of structural diversity, especially considering the similarities among the ligands. Dimers have close Ag-Ag contacts that are consistent with argentophilic interactions. The Ag-Ag distances in the monomers are too long to have argentophilic interactions. Silver pyrazolate complexes containing NHC ligands have been reported.[176-178,189] Nevertheless, the previously reported silver pyrazolate NHC adducts are not structurally similar to the complexes reported herein.

The Ag(pz)(NHC) adducts are air, moisture, and light stable. Silver pyrazolate precursors have not been used in any thermal or plasma ALD processes. Trimers **1** and **2** show similar sublimation temperatures to Ag(pz)(NHC) adducts, raising the possibility that **1** and **2** may sublime as monomers or dimers. Consequently, monomers, dimers, and trimers showed similar volatilities. Trimers **1** and **2** evaporate completely without decomposition, and TGA traces showed single step weight losses with approximately zero residual masses. All of the Ag(pz)(NHC) complexes synthesized herein do not evaporate entirely and decompose at >300 °C to afford nonvolatile residues. Trimers have higher thermal stabilities than most of the Ag(pz)(NHC) complexes. Among NHC complexes, only **4** has higher thermal stability than its parent trimer **1**. The thermal properties of Ag(pz)(NHC) adducts can be compared with reported Ag ALD[64,95-102] and CVD[85,115,123-129] precursors. Ag precursors such as Ag(Piv)(PEt_3), Ag(hfac)(1,5-COD),

Ag(hfac)(PMe_3), and Ag(fod)(PEt_3) have been widely used in Ag CVD and ALD studies. In almost every case, TGA studies reveal that the precursors decompose at > 250 °C and leave residues approximately similar to or higher than the amount of Ag in the complexes.[64] A similar pattern of TGA traces were observed for the complexes reported herein. The TGA trace of the recently reported Ag(hmds)(NHC)[97] precursor is also similar to most of the Ag(pz)(NHC) described herein. However, **3-5** and **9**•Et_2O contain $(CF_3)_2$pz ligands have slightly higher thermal stabilities than most of the available Ag(*β*-diketonate) phosphine or alkene adducts.

Liquid precursors are preferred in ALD and CVD since liquids have a constant surface area, which gives constant gas phase precursor concentrations. Complexes **3**-**6**, **8**, and **9**·Et_2O have melting points that are lower than the sublimation temperatures and are thus delivered from the liquid state. These low melting points considered as an improvement over the trimers, which sublime as solids. Reducing agents such as 1-propanol, *tert*-butyl hydrazine, and $BH_3(NHMe_2)$ have been used in Ag thermal ALD processes.[98,100-102] Nevertheless, solution reduction experiments were poorly documented or were not carried out. The Ag(pz)(NHC) adducts showed good reactivity towards several reducing agents, which was confirmed by the formation of Ag metal in the solution.

Overall, NHCs were used to synthesize Ag(pz)(NHC) adducts with large structural diversity. Ag(pz)(NHC) adducts showed similar volatility and solution reactivity to trimers. However, Ag(pz)(NHC) adducts have poor thermal stabilities compared to trimers **1** and **2**. ALD experiments were not carried out using any of these Ag(pz)(NHC) precursors.

3.4 Experimental Section

General Considerations. The synthesis and manipulation of **3-10** were carried out under argon, using either a glove box or Schlenk line techniques. Hexane was distilled from sodium,

tetrahydrofuran and diethyl ether were distilled from purple solutions of sodium benzophenone ketyl, and toluene was distilled from sodium. Anhydrous pentane was purchased from Sigma Aldrich and was used as received. Silver oxide was purchased from Fischer Scientific. 3,5-Bis(trifluoromethyl)pyrazole was purchased from Matrix Scientific. 2,2-Dimethyl-6,6,7,7,8,8,8-heptafluoro-3,5-octanedione was purchased from TCI Chemicals. Hydrazine hydrate solution and concentrated sulfuric acid were purchased from Sigma-Aldrich. The silver pyrazolates **1** and **2** were prepared according to literature procedures.[141-142] 3-*tert*-Buyl-5-heptafluoropropylpyrazole was synthesized according to a literature procedure.[198-199] Saturated and unsaturated carbenes were prepared using published procedures.[180-181]

^{1}H NMR and ^{13}C{H} NMR spectra were obtained in deuterated benzene, chloroform, toluene, or dimethyl sulfoxide as indicated and were referenced to the residual proton and carbon resonance of the solvents. Melting points were determined on a Thermo Scientific Mel-Temp 3.0 digital melting point apparatus. TGA and DTA were carried out with a SDT 2960 TGA/DTA instrument. Infrared spectra were obtained from SHIMADZU IRTracer-100. CHN microanalysis was performed by Midwest Microlab, Indianapolis, IN.

Preparation of Ag-(3,5-CF_3)pz(^{Me2}NHC) (3). A 100-mL Schlenk flask was charged with a magnetic stir bar, **1** (1.00 g, 1.07 mmol), and hexane (40 mL). To this stirred solution at ambient temperature was slowly added a solution of 1,3-dimethyl-4,5-dimethyl-1H-imidazol-3-ium-2-ide (0.399 g, 3.19 mmol) in hexane (30 mL). This solution was stirred at ambient temperature for 18 h. The volatile components were removed under reduced pressure and the resultant pale brown colored solid was dissolved in diethyl ether (30 mL). The solution was filtered through a 2-cm pad of Celite on a coarse glass frit, and concentrated to about 20 mL under reduced pressure. Hexane (20 mL) was slowly added to the flask to form a separate layer on top of the diethyl ether layer.

The flask was then placed in a 4 °C refrigerator for 24 h to allow solvent diffusion to occur. This procedure afforded **3** as colorless crystals (0.604 g, 44%). X-ray quality crystals were obtained from this crystallization process: mp 114-117 °C, dec. 203 °C; ^{1}H NMR (benzene-d_6, 23 °C, δ) 7.06 (s, 1 H, Pz-***H***), 2.69 (s, 6 H, N-C***H***$_3$), 1.18 (s, 6 H, C-C***H***$_3$); ^{13}C{^{1}H} NMR (benzene-d_6, 23 °C, ppm) 175.95 (s, ***C***-Ag), 143.20 (q, CF$_3$***C***N, $^{2}J_{CF}$ = 35.1 Hz), 125.30 (s, ***C***-CH$_3$), 123.43 (q, ***C***F$_3$, $^{1}J_{CF}$ = 267.8 Hz), 102.46 (m, ***C***H), 35.33 (s, N-***C***H$_3$), 8.16 (s, C-***C***H$_3$); IR (cm^{-1}) 2158 (w), 1502 (w), 1437 (w), 1343 (w), 1256 (m), 1109 (s), 1003 (m), 847 (m), 793 (m).

Anal. Calc for $C_{12}H_{13}AgF_6N_4$: C, 33.13; H, 3.01; N, 12.88. Found: C, 33.11; H, 2.99; N, 12.74.

Preparation of Ag-(3,5-CF$_3$)pz(*^{Et2}*NHC) (4). In a fashion similar to the preparation of **3**, treatment of **1** (1.05 g, 1.13 mmol) with 1,3-diethyl-4,5-dimethyl-1H-imidazol-3-ium-2-ide (0.488 g, 3.20 mmol) afforded **4** as colorless crystals (0.705 g, 44%). X-ray quality crystals were grown from hexane by slow evaporation at room temperature: mp 96-98 °C, dec. 293 °C; ^{1}H NMR (benzene-d_6, 23 °C, δ) 7.01 (s, 1 H, Pz-***H***), 3.20 (q, J = 7.4 Hz, 4 H, N-C***H***$_2$CH$_3$), 1.20 (s, 6 H, C-C***H***$_3$), 0.74 (t, J = 7.4 Hz, 6 H, N-CH$_2$C***H***$_3$); ^{13}C{^{1}H} NMR (benzene-d_6, 23 °C, ppm) 174.46 (s, ***C***-Ag), 143.35 (q, CF$_3$***C***N, $^{2}J_{CF}$ = 35.1 Hz), 124.62 (s, ***C***-CH$_3$), 123.23 (q, ***C***F$_3$, $^{1}J_{CF}$ = 267.8 Hz), 102.64 (m, ***C***H), 44.09 (s, N-***C***H$_2$CH$_3$), 16.65 (s, N-CH$_2$***C***H$_3$), 8.09 (s, C-***C***H$_3$); IR (cm^{-1}) 2988 (w), 1504 (w), 1344 (m), 1252 (s), 1109 (s), 1005 (s), 806 (s).

Anal. Calc for $C_{28}H_{34}Ag_2F_{12}N_8$: C, 36.30; H, 3.69; N, 12.09. Found: C, 33.89; H, 3.15; N, 11.62.

Preparation of Ag-(3,5-CF$_3$)pz(*^{iPr2}*NHC) (5). In a fashion similar to the preparation of **3**, treatment of **1** (1.00 g, 1.07 mmol) with 1,3-diisopropyl-4,5-dimethyl-1H-imidazol-3-ium-2-ide (0.580 g, 3.21 mmol) afforded **5** as colorless crystals (0.981 g, 62%). X-ray quality crystals were

grown from hexane by slow evaporation at room temperature: mp 101-102 °C, dec. 233 °C; ^{1}H NMR (benzene-d_6, 23 °C, δ) 7.03 (s, 1H, Pz-***H***), 3.79 (septet, J = 7.0 Hz, 2H, N-C***H***$(CH_3)_2$), 1.28 (s, 6H, C-C***H***$_3$), 1.13 (d, J = 6.6 Hz, 6H, N-CH(C***H***$_3)_2$); ^{13}C{^{1}H} NMR (benzene-d_6, 23 °C, ppm) 170.03 (s, ***C***-Ag), 143.28 (q, CF_3***C***N, $^{2}J_{CF}$ = 35.1 Hz), 124.47 (s, ***C***-CH_3), 123.64 (q, ***C***F_3, $^{1}J_{CF}$ = 268.2 Hz), 102.82 (m, ***C***H), 50.79 (s, N-***C***H$(CH_3)_2$), 23.93 (s, N-CH(***C***$H_3)_2$), 8.69 (s, C-***C***H_3); IR (cm^{-1}) 2986 (w), 1499 (w), 1369 (w), 1252 (s), 1113 (s), 1003 (s), 974 (m), 800 (m).

Anal. Calc for $C_{16}H_{21}AgF_6N_4$: C, 39.12; H, 4.31; N, 11.41. Found: C, 39.31; H, 4.21; N, 11.42.

Preparation of Ag-(3-tBu,5-C_3F_7)pz(*Me2*NHC) (6). In a fashion similar to the preparation of **3**, treatment of **2** (1.05 g, 0.882 mmol and 1,3-dimethyl-4,5-dimethyl-1H-imidazol-3-ium-2-ide (0.310 g, 2.49 mmol) afforded **6** as colorless crystals (0.630 g, 46%). X-ray quality crystals were obtained by recrystallization from diethyl ether/hexane (1:1) at -30 °C: mp 107-109 °C, dec. 180 °C; ^{1}H NMR (benzene-d_6, 23 °C, δ) 6.85 (s, 1H, Pz-***H***), 2.70 (s, 6H, N-C***H***$_3$), 1.63 (s, 9H, C(C***H***$_3)_3$, 1.17 (s, 6H, C-C***H***$_3$); ^{13}C{^{1}H} NMR (benzene-d_6, 23 °C, δ) 177.43 (s, ***C***-Ag), 162.30 (s, $(CH_3)_3$C***C***N), 139.66 (t, CF_2***C***N, J_{CF} = 26.7 Hz), 124.87 (s, ***C***-CH_3), 119.49 (qt, ***C***F_3, $^{1}J_{CF}$ = 272.8 Hz, $^{2}J_{CF}$ = 30.9 Hz), 110.10 (m, ***C***F_2CN), 110.47 (m, CF_2***C***F_2CF_3), 100.46 (s, *C*H), 35.16 (s, N-***C***H_3), 32.29 (s, ***C***$(CH_3)_3$), 32.04 (s, C(***C***$H_3)_3$), 8.18 (s, C-***C***H_3); IR (cm^{-1}) 2953 (m), 1460 (w), 1388 (w), 1342 (m), 1202 (s), 1099 (s), 995 (m), 866 (s), 743 (s).

Anal. Calc for $C_{17}H_{22}AgF_7N_4$: C, 39.03; H, 4.24; N, 10.71. Found: C, 39.00; H, 4.18; N, 10.71.

Preparation of Ag-(3-tBu,5-C_3F_7)pz(*Et2*NHC) (7). In a fashion similar to the preparation of **3**, treatment of **2** (0.500 g, 0.419 mmol) with1,3-diethyl-4,5-dimethyl-1H-imidazol-3-ium-2-ide (0.192 g, 1.26 mmol) afforded **7** as a crystalline solid (0.071 g, 10 %): mp 88-91 °C, dec. 160 °C;

^{1}H NMR (benzene-d_6, 23 °C, δ) 6.87 (s, 1H, Pz-***H***), 3.23 (q, J = 7.4 Hz, 4H, N-C***H***$_2$CH$_3$), 1.63 (s, 9H, C(C***H***$_3$)$_3$, 1.19 (s, 6H, C-C***H***$_3$), 0.75 (t, J = 7.0 Hz, 6H, CH$_2$C***H***$_3$); ^{13}C{^{1}H} NMR (benzene-d_6, 23 °C, δ) 175.69 (s, ***C***-Ag), 162.21 (s, (CH$_3$)$_3$C***C***N), 139.78 (t, CF$_2$***C***N, J_{CF} = 26.3 Hz), 124.41 (s, ***C***-CH$_3$), 119.4 (qt, ***C***F$_3$, $^{1}J_{CF}$ = 288.0 Hz, $^{2}J_{CF}$ = 35.9 Hz), 110.32 (m, ***C***F$_2$CN), 109.91 (m, CF$_2$***C***F$_2$CF$_3$), 100.58 (s, *C*H), 43.89 (s, N-***C***H$_2$CH$_3$, 32.14 (s, ***C***(CH$_3$)$_3$), 31.87 (s, C(***C***H$_3$)$_3$), 16.67 (s, N-CH$_2$***C***H$_3$), 8.13 (s, C-***C***H$_3$); IR (cm^{-1}) 2968 (m), 1504 (w), 2349 (m), 1464 (m), 1369 (m), 1346 (s), 1203 (s), 1091 (s), 970 (w), 868 (s).

Anal. Calc for $C_{19}H_{26}Ag_1F_7N_4$: C, 41.40; H, 4.75; N, 10.16. Found: C, 41.23; H, 4.89; N, 10.08.

Preparation of Ag-(3-tBu, 5-C$_3$F$_7$)pz(*^{iPr2}*NHC) (8). In a fashion similar to the preparation of **3**, treatment of **2** (0.500 g, 0.420 mmol) with 1,3-diisopropyl-4,5-dimethyl-1H-imidazol-3-ium-2-ide (0.230 g, 1.28 mmol) afforded **8** as colorless crystals (0.589 g, 81%). X-ray quality crystals were grown from hexane by slow evaporation at room temperature: mp 94-95 °C, dec. 200 °C; ^{1}H NMR (benzene-d_6, 23 °C, δ) 6.87 (s, 1H, Pz-***H***), 3.93 (septet, J = 6.6 Hz, 2H, N-C***H***(CH$_3$)$_2$), 1.63 (s, 9H, C(C***H***$_3$)$_3$), 1.32 (s, 6H, C-C***H***$_3$), 1.15 (d, J = 6.6 Hz, 6H, N-CH(C***H***$_3$)$_2$); ^{13}C{^{1}H} NMR (benzene-d_6, 23 °C, ppm) 162.43 (s, (CH$_3$)$_3$C***C***N), 139.55 (t, CF$_2$***C***N, J_{CF} = 26.3 Hz), 124.32 (s, ***C***-CH$_3$), 116.95 (qt, ***C***F$_3$, $^{1}J_{CF}$ = 251.4 Hz, $^{2}J_{CF}$ = 32.0 Hz), 110.41 (m, ***C***F$_2$CN), 110.04 (m, CF$_2$***C***F$_2$CF$_3$), 100.60 (s, ***C***H), 51.50 (s, N-***C***H(CH$_3$)$_2$), 32.29 (s, ***C***(CH$_3$)$_3$), 31.94 (s, C(***C***H$_3$)$_3$), 23.45 (s, N-CH(***C***H$_3$)$_2$), 8.84 (s, C-***C***H$_3$); IR (cm^{-1}) 2961 (m), 1398 (m), 1367 (m), 1331 (m), 1223 (s), 1173 (s), 1103 (s), 993 (m), 867 (s), 744 (m).

Anal. Calc for $C_{21}H_{30}AgF_7N_4$: C, 43.54; H, 5.22; N, 9.67. Found: C, 43.82; H, 5.04; N, 9.70.

Preparation of $Ag_2(3,5\text{-}CF_3)_2pz(^{tBu2}NHC)Et_2O$ (9·Et_2O). In a fashion similar to the preparation of **3**, treatment of **1** (1.03 g, 1.10 mmol) with 1,3-di-*tert*-butylimidazolidine (0.608 g, 3.33 mmol) afforded **9** as colorless, X-ray quality crystals (0.472 g, 29%): mp 109-111 °C, dec. 205 °C; ^{1}H NMR (benzene-d_6, 23 °C, δ) 6.82 (s, 1H, Pz-***H***), 3.28 (q, 4H, $CH_3C\boldsymbol{H_2}$-O), 2.51 (s, 4H, -C***H***$_2$), 1.12 (t, 6H, C***H***$_3CH_2$-O), 1.08 (s, 18H, N-C(C***H***$_3)_3$; $^{13}C\{^1H\}$ NMR (benzene-d_6, 23 °C, ppm) 174.57 (s, ***C***-Ag), 143.73 (q, $CF_3\boldsymbol{C}N$, $^2J_{CF}$ = 35.9 Hz), 122.38 (q, ***C***F_3, $^1J_{CF}$ = 268.2 Hz), 102.97 (m, ***C***H), 65.92 (s, $CH_3\boldsymbol{C}H_2$-O-), 54.92 (s, N-***C***H_2-), 45.47 (s, N-***C***$(CH_3)_3$), 30.43 (s, N-C(***C***$H_3)_3$), 15.59 (s, ***C***H_3CH_2-O-); IR (cm^{-1}) 2980 (w), 1543 (m), 1435 (m), 1367 (m), 1256 (s), 1111 (s), 1009 (s), 802 (s), 756 (m).

Anal. Calc for $C_{46}H_{58}Ag_4F_{24}N_{12}$: C, 32.84; H, 3.47; N, 9.98. Found: C, 32.92; H, 3.33; N, 10.03.

Preparation of Ag-(3-tBu,5-C_3F_7)pz(^{tBu2}NHC) (10). In a fashion similar to the preparation of **3**, treatment of **2** (0.517 g, 0.434 mmol) with 1,3-di-*tert*-butylimidazolidine (0.237 g, 1.29 mmol) afforded **10** as colorless crystals (0.123 g, 17%): mp 146-149 °C, dec. 191 °C; ^{1}H NMR (benzene-d_6, 23 °C, δ) 6.81 (s, 1H, Pz-***H***), 2.56 (s, 4H, -C***H***$_2$), 1.58 (s, 9H, C(C***H***$_3)_3$, 1.14 (s, 18H, N-C(C***H***$_3)_3$; $^{13}C\{^1H\}$ NMR (benzene-d_6, 23 °C, ppm) 162.02 (s, $(CH_3)_3C\boldsymbol{C}N$), 139.98 (t, $CF_2\boldsymbol{C}N$, J_{CF} = 25.18 Hz), 119.20 (qt, ***C***F_3, $^1J_{CF}$ = 288.0 Hz, $^2J_{CF}$ = 31.3 Hz), 110.06 (m, ***C***F_2CN), 109.69 (m, $CF_2\boldsymbol{C}F_2CF_3$), 101.11 (s, ***C***H), 55.02 (s, N-***C***H_2-), 45.57 (s, N-***C***$(CH_3)_3$), 31.96 (s, ***C***$(CH_3)_3$), 31.56 (s, C(***C***$H_3)_3$), 30.56 (s, N-C(***C***$H_3)_3$); IR (cm^{-1}) 2963 (w), 1479 (m), 1435 (w), 1342 (m), 1204 (s), 1099 (s), 997 (m), 869 (s), 777 (m), 742 (s).

Anal. Calc for $C_{21}H_{32}AgF_7N_4$: C, 43.40; H, 5.55; N, 9.64. Found: C, 43.17; H, 5.30; N, 9.60.

CHAPTER 4
SYNTHESIS AND CHARACTERIZATION OF THERMALLY STABLE AND VOLATILE N-HETEROCYCLIC CARBENE SILVER DIKETONATE PRECURSORS

4.1 Introduction

Ag(*β*-diketonate) alkene and phosphine adducts have been widely used in Ag metal CVD and ALD studies. Thermal and plasma ALD processes were performed using Ag(*β*-diketonate) precursors such as (hfac)Ag(1,5-COD), Ag(hfac)PMe_3, Ag(thd)PEt_3, Ag(Piv)PEt_3, and Ag(fod)PEt_3.[64,96,98-100,102] The alkene-based precursor (hfac)Ag(1,5-COD) has very low thermal stability, due to loss of the COD ligand at or below the sublimation temperature to afford non-volatile Ag$(hfac)_n$ species.[200] Among phosphine based precursors, Ag(fod)PEt_3 has been extensively employed in Ag metal ALD processes due to its promising precursor properties.[64,96,102] Thermogravimetric analysis (TGA) of Ag(fod)PEt_3 suggested that it should be thermally stable at least up to 230 °C.[64] However, ALD experiments revealed that precursor decomposition occurs above 140 °C due to the observation of non-uniform film thicknesses.[64] Neutral donor ligands such as phosphines could also easily dissociate from the metal complexes, thus giving a low-temperature decomposition pathway. Thermal ALD requires highly thermally stable precursors to achieve self-limited growth. However, the Ag ion has a very positive electrochemical potential (E° ($Ag^+ + e^- \leftrightarrow Ag$) = 0.7996 V) and Ag(I) in the complexes can easily be reduced into Ag metal by the anionic ligands. Therefore, it is a challenge to prepare highly thermally stable Ag metal precursors.

Chapter 3 explained the syntheses, structure, and precursor properties of a series of Ag(pyrazolate)(NHC) complexes. Solid state structures of Ag(pyrazolate)(NHC) complexes showed considerable diversity, including dimers, monomers, and a tetramer. Ag-C(carbene) bond lengths in these complexes varied from 2.051-2.093 Å, demonstrating strong coordination of

NHCs to the Ag(I) ions. Chapter 4 discusses the syntheses, structure, and thermal properties of Ag(diketonate)(NHC) adducts. Five different β-diketonate ligand precursors were chosen, including 1,1,1,5,5,5-hexafluoroacetylacetone (Hhfac), 1,1,1,2,2,3,3-heptafluoro-7,7-dimethyloctane-4,6-dione (Hfod), 2,2,6,6-tetramethylheptane-3,5-dione (Hthd), 1,1,1-trifluoro-5,5-dimethylhexane-2,4-dione (Hpta), and 1-(2-thienoyl)-3,3,3-trifluoroacetone (Htta). The parent Ag diketonates are shown in Chart 7. Electron-withdrawing fluorinated substituents were introduced to decrease the electron density on the diketonate ligand. The alkyl or fluorinated groups on the β-diketonate ligands lower the intermolecular attractions between individual molecules, thereby increasing the volatilities. The unsaturated carbene ^{iPr2}NHC and saturated carbene ^{tBu2}NHC were used for the preparation of monomeric Ag(diketonate)(NHC) adducts.

Chart 8. Silver diketonates.

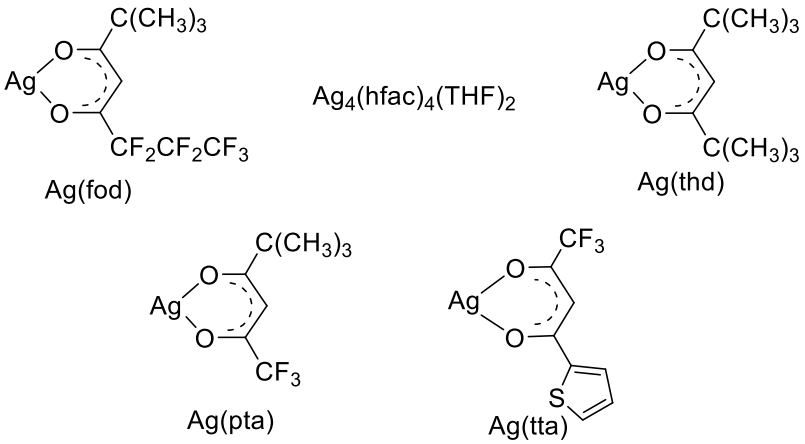

4.2 Result and Discussion

Synthetic Aspects. Two different NHCs were chosen, the unsaturated carbene ^{iPr2}NHC and saturated carbene ^{tBu2}NHC. These ligands were prepared by reported methods.[180-181] Five different silver diketonates (Ag(hfac), Ag(fod), Ag(thd), Ag(pta), and Ag(tta)) were synthesized using previously reported procedures.[64,201-202] Treatment of the silver-diketonate complexes with

the carbenes resulted in the new complexes **11**-**18** as colorless crystalline solids in 20-48% yields (equations 3 and 4). A one-pot synthesis route employing Ag_2O, carbene, and a diketone resulted in **19** and **20** as stabilized carbenium ions with anionic diketonates (equation 5). All reactions were carried out under an argon atmosphere. However, isolated crystalline solids were all stable indefinitely in ambient atmosphere. Several attempts at purifying Ag(tta)(^{iPr2}NHC) and Ag(tta)(^{tBu2}NHC) were unsuccessful. Preliminary ^{1}H NMR spectroscopy data of these complexes suggested the presence of [^{iPr2}NHC][tta] and [^{tBu2}NHC][tta], along with Ag(tta)(^{iPr2}NHC) and Ag(tta)(^{tBu2}NHC). These mixtures could not be separated by crystallization from solvents, since both the silver complex and the organic compound appeared to have similar solubilities. Accordingly, these compounds were not pursued further.

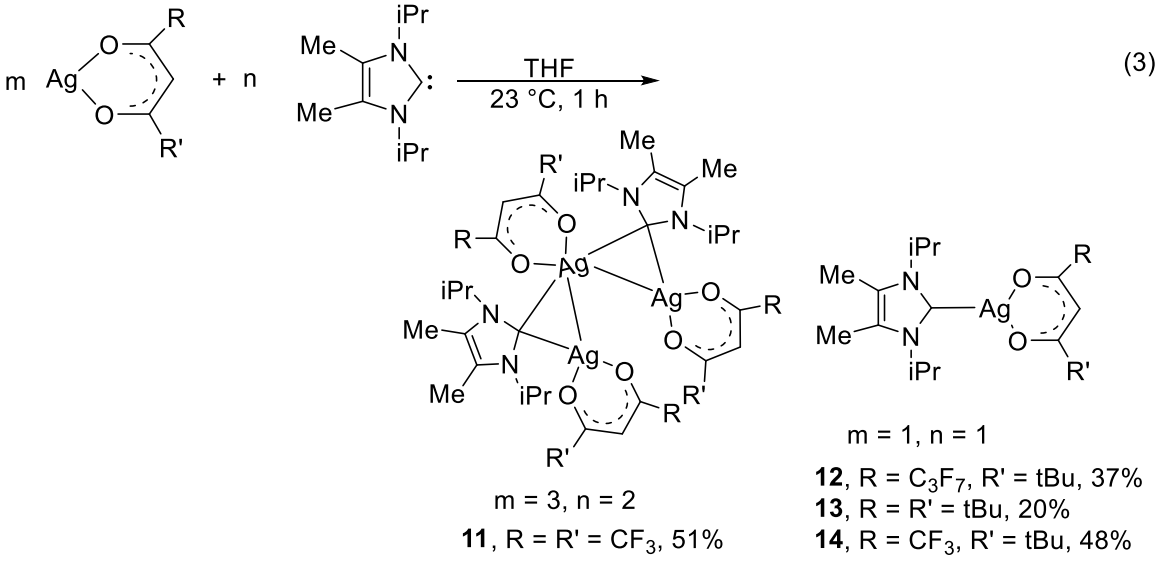

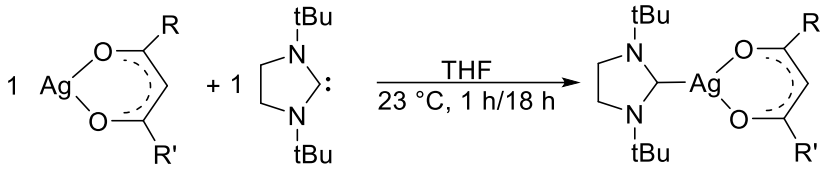

(4)

15, R = R = R' = CF_3, 32%
16, R = C_3F_7, R' = tBu, 25%
17, R = R' = tBu, 20%
18, R = CF_3, R' = tBu, 41%

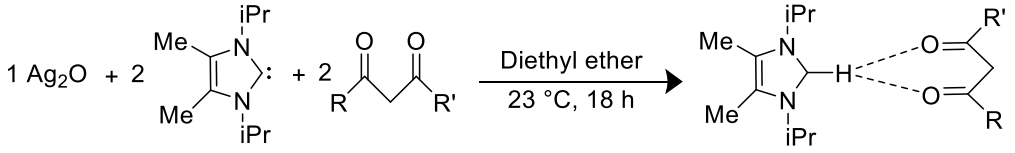

(5)

19, R = R' = CF_3,7%
20, R = R' = tBu, 49%

Complexes **11**-**20** were characterized by spectral and analytical methods. Furthermore, crystal structures of **11**, **13**-**16**, and **18**-**20** were determined. The solid state structures are described below. All complexes are diamagnetic and were subjected to ^{1}H and ^{13}C{^{1}H} NMR analyses. The ^{1}H NMR spectrum of crystalline **11** showed resonances for the carbene and the diketonate ligands with a 2:3 integration. The NMR spectra of all other metal complexes showed one type of diketonate and carbene ligands at 23 °C. The ^{1}H NMR spectra of crystalline **19** and **20** showed an extra proton resonance at 10.96, and 13.06 ppm, respectively. These protons correspond to the imidazolium-H atoms in **19** and **20**. During the synthesis of **17** and **18**, minor resonances were also observed in the crude product mixtures that might correspond to analogues of **19** and **20**. However, these minor compounds could not be crystallized in pure form and were thus not characterized. NMR samples of **11**, **12**, **17**, and **18** showed the formation of silver metal on the walls of the NMR tube after standing for several days. Compounds **11**-**18** need to be crystallized within 24-48 h from solvents to obtain colorless crystals. Longer crystallization times give brown-colored crystals. This

observation could be due to slow decomposition of the crude materials in solutions. The carbene carbon atom resonances in the $^{13}C\{^{1}H\}$ NMR spectra of **11**-**14** and **15**-**18** were observed as broad signals in the range of 166.29-176.83 and 204.33-206.33 ppm, respectively. ^{13}C-$^{107/109}Ag$ coupling was not observed, suggesting rapid exchange of the carbene ligands at 23 °C.[173,182-186] For instance, carbene carbon atom of Ag(1,3-diphenyl-1,3-propanedionate)(^{Me2}NHC) had a resonance of 179.4 ppm and ^{13}C-$^{107/109}Ag$ coupling was not observed.[183]

X-Ray Crystal Structures. The X-ray crystal structures of **11**, **13**-**16**, and **18**-**20** were obtained to determine the solid state configurations. The crystallographic data are summarized in Tables 10-12, while selected bond distances and angles are shown in Tables 13 and 14. Figures 37-44 show representative perspective views of **11**, **13**-**16**, and **18**-**20**. Complex **11** forms a trimer, whereas **13**-**16** and **18** crystallized as monomers. Complex **11** contains three diketonate ligands coordinated to each Ag atom with two carbene ligands on the terminal Ag ions.

Complex **11** crystallizes as a trimeric complex, as shown in Figure 37. There are two crystallographically independent molecules present in the unit cell of **11**. Each Ag atom in the complex is bonded to a κ^2-diketonate ligand. Additionally, there are two μ_2-bridging carbene ligands, each of which is coordinated to the central Ag ion and a terminal Ag ion. The Ag-Ag distances in **11** are 2.7076(3), 2.7313(3), and 3.3446(3) Å, which are consistent with argentophilic interactions because Ag-Ag distances are shorter than twice the van der Waals radius for the Ag atom (3.44 Å).[163,165] The Ag-O distances are 2.328(2) (Ag1A-O1A), 2.187(2) (Ag1A-O2A), 2.351(2) (Ag2A-O3A), 2.357(2) (Ag2A-O4A), 2.184(2) (Ag3A-O5A), and 2.341(2) (Ag3A-O6A) Å. Two diketonate ligands in **11** have asymmetric Ag-O bond lengths to the Ag ions (Ag1A-O1A 2.328(2); Ag1A-O2A 2.187(2) Å and Ag3A-O5A 2.184(2); Ag3A-O6A 2.341(2) Å) while one diketonate ligand has symmetric Ag-O bond lengths to the Ag ion (Ag2A-O4A 2.351(2); Ag2A-

O3A 2.356(2) Å). Asymmetric Ag-O bond lengths are very common in Ag-diketonate complexes.[64] The Ag-C bond lengths are 2.124(2) (Ag1A-C1A), 2.360(2) (Ag2A-C1A), 2.119(2) (Ag3A-C27A), and 2.381(2) (Ag2A-C27A). The Ag-C bond lengths to Ag2A are longer than those to Ag1A and Ag3A because of the higher coordination number at Ag2A (6-coordinate) compared to Ag1A and Ag3A (4-coordinate). Therefore, the Ag-C bonds to Ag2A should be weaker than Ag-C bonds to Ag1A and Ag3A.

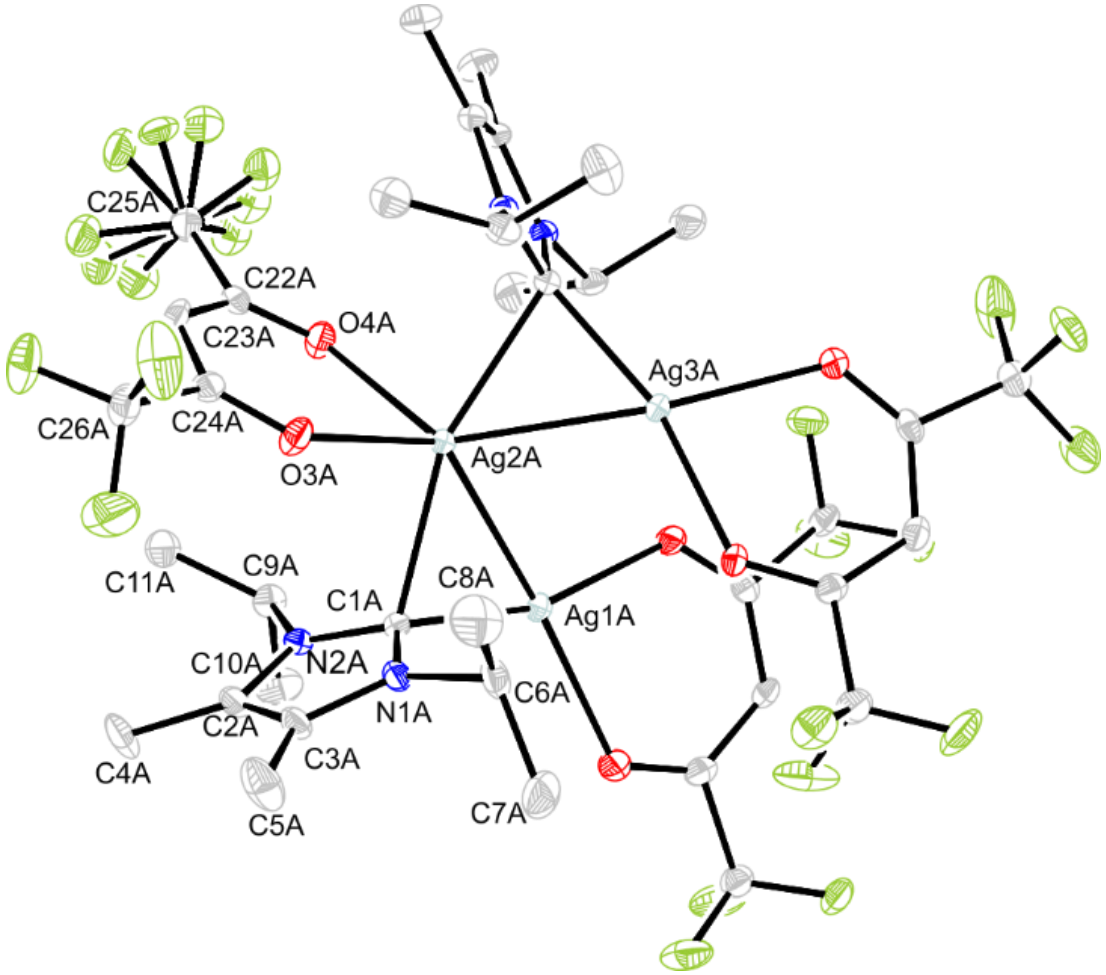

Figure 37. Perspective view of **11** with thermal ellipsoids at the 50% probability level.

Complexes **13**, **14**, **15**, **16**, and **18** crystallize as monomers with very similar bond distances and angles (Figures 38-42). Ag-Ag bond distances (**13**, 6.132; **14**, 5.799; **15**, 6.889; **16**, 10.883; **18**, 10.171 Å) are much longer than twice the van der Waals radius for the Ag atom (3.44 Å).[165] Accordingly, argentophilic interactions were not observed in any of these complexes. The Ag-C bond lengths (**13**, Ag1-C12 2.064(2); **14**, Ag1-C1 2.072(2); **15**, Ag1-C10 2.096(3); **16**, Ag1-C1 2.090(2); **18**, Ag1-C1 2.089(2) Å) are identical within experimental uncertainty. The Ag-C bond lengths observed in **13**, **14**, **15**, **16**, and **18** are identical to Ag-C bond distances observed in **11** (Ag1A-C1A 2.124(2); Ag3A-C27A 2.119(2) Å). The diketonate ligands in **13**, **14**, **15**, **16**, and **18** have asymmetric Ag-O bond lengths (**13**, Ag1A-O1A 2.198(1) and Ag1A-O2A 2.283(1) Å; **14**, Ag1A-O1A 2.268(1) and Ag1A-O2A 2.272(1) Å; **15**, Ag1A-O1A 2.277(2) and Ag1A-O2A 2.303(3) Å; **16**, Ag1A-O1A 2.174(1) and Ag1A-O2A 2.367(1) Å; **18**, Ag1A-O1A 2.228(1) and Ag1A-O2A 2.296(1) Å). However, C-O bond distances (1.242-1.267 Å) in the diketonate have no significant difference. The C-C bond distances between the carbon atoms in the diketonate backbone are also approximately the same (1.371-1.428 Å). Therefore, the charges of the diketonate ligands are delocalized well. The ^{iPr2}NHC ligands in **13** and **14** are located on the same plane with the silver(*β*-diketonate) plane. However, ^{tBu2}NHC ligands in **15**, **16**, and **18** are slightly twisted from the silver(*β*-diketonate) plane. The carbene ligands try to be coplanar with the diketonate ligands to reduce the steric hindrance. This is favorable in unsaturated carbenes having a C=C backbone. The sum of the bond angles around the Ag ions in **13**, **14**, **15**, **16**, and **18** (~359.9°) are close to 360°, which is consistent with distorted trigonal planar geometry around Ag ion in each complex.

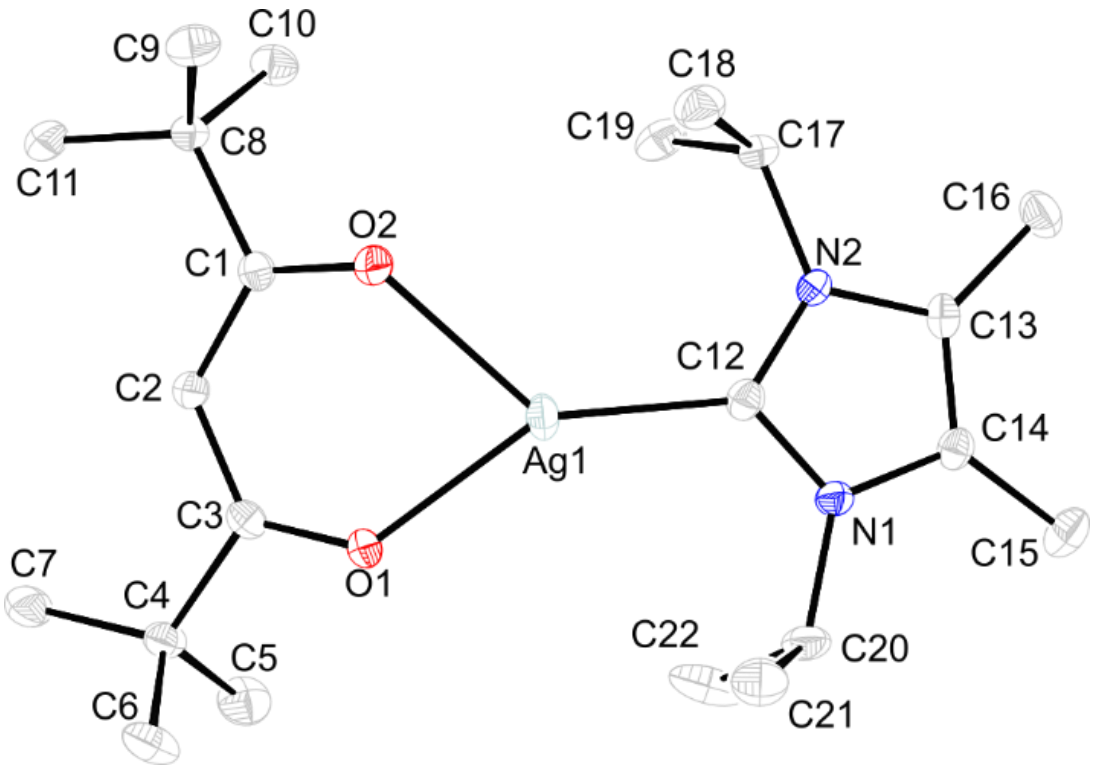

Figure 38. Perspective view of **13** with thermal ellipsoids at the 50% probability level.

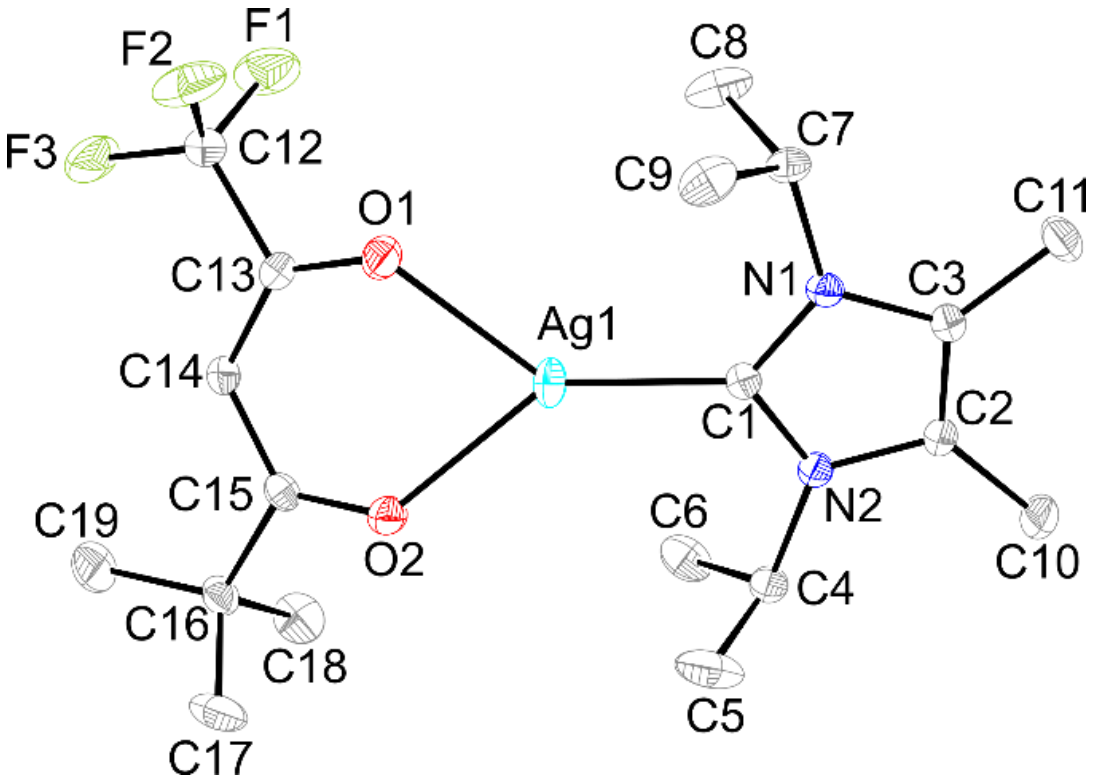

Figure 39. Perspective view of **14** with thermal ellipsoids at the 50% probability level.

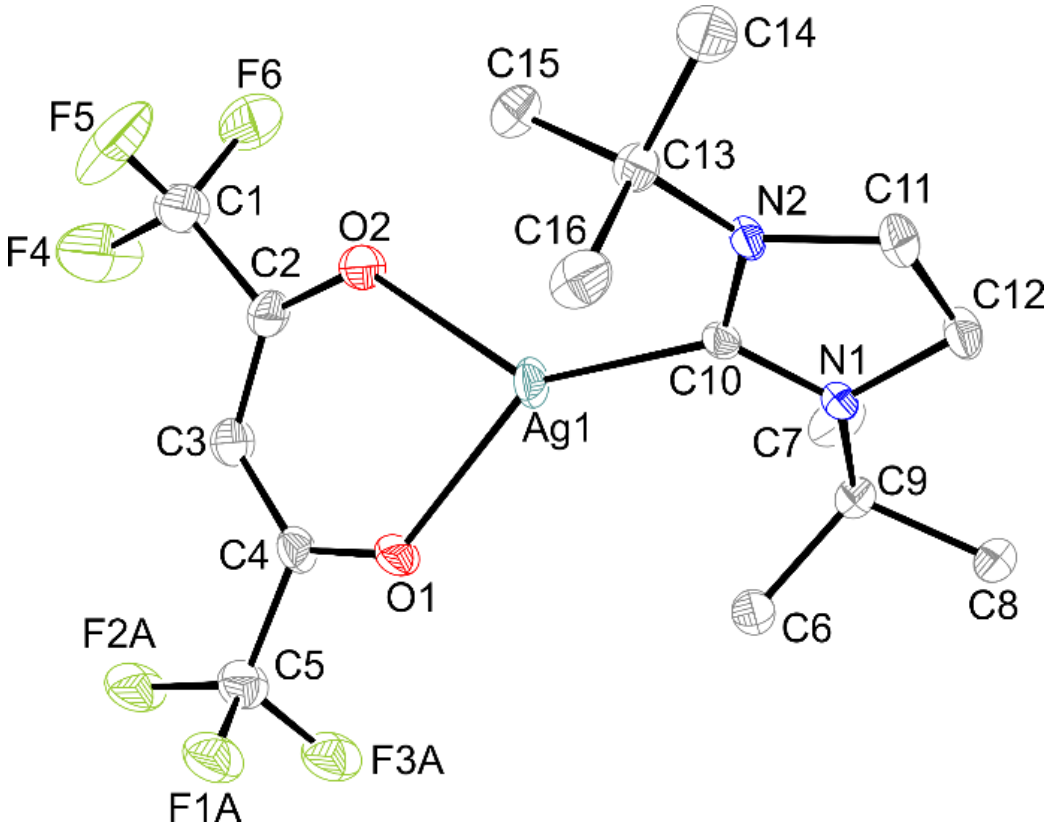

Figure 40. Perspective view of **15** with thermal ellipsoids at the 50% probability level.

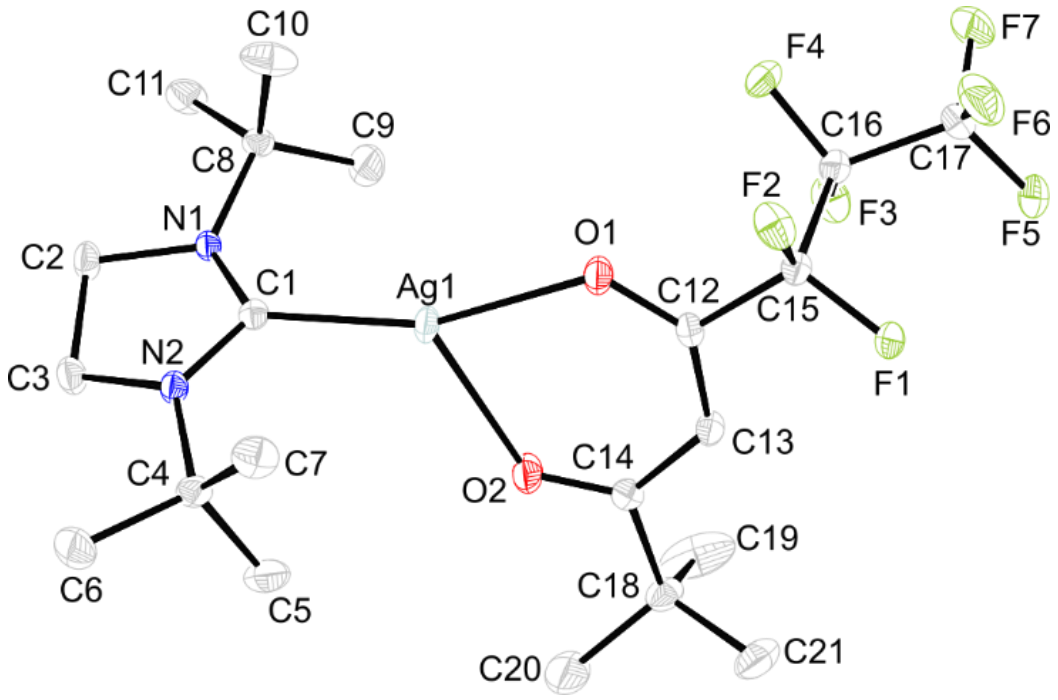

Figure 41. Perspective view of **16** with thermal ellipsoids at the 50% probability level.

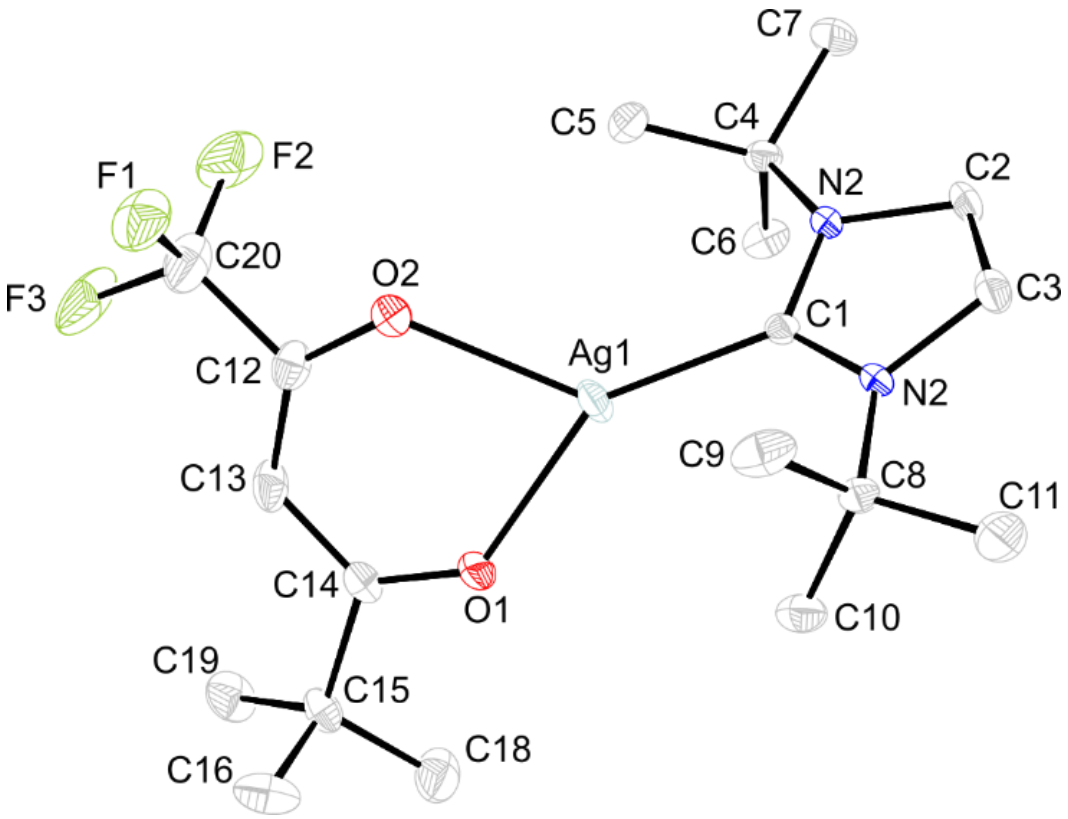

Figure 42. Perspective view of **18** with thermal ellipsoids at the 50% probability level.

The solid state structures of **19** and **20** revealed protonated NHCs with *β*-diketonate anions (Figures 43 and 44). In **19** and **20**, the NHC and *β*-diketonate ions are located in different planes. There are hydrogen bonding interactions observed in both of these complexes. In **19**, the H•••O bond distances are 2.344 and 2.444 Å. H•••O bond distances of 2.187 and 2.274 Å are observed in **20**. These hydrogen bonding interactions stabilize the carbenium ion with the diketonate anion in the solid state. Complexes **19** and **20** can be compared with previously reported imidazolium cyclopentadienides.[203] The reaction of imidazolium with both $[Cp_2Ti^{III}Cl]_2$ and CpLi afforded $[NHC^{Dipp}H]^+[Cp]^-$ where NHC^{Dipp} = ^{iPr2}NHC.[203] The solid state structure reveals the imidazolium proton directed at the Cp^- ring and involves C-H···Cp^- (2.171Å) hydrogen bonding. However, in solution $[NHC^{Dipp}H]^+[Cp_2Ti^{III}Cl_2]^-$ dissociates to NHC^{Dipp} and cyclopentadienide through intramolecular proton transfer.[203] In another study, ^{iPr2}NHC was treated with cyclopentadienes to obtain similar imidazolium cyclopentadienides.[204] The carbene acts as a Bronsted base and deprotonates the cyclopentadiene to give imidazolium cyclopentadienides.[204] They have been used as Cp transfer reagents in different cyclopentadienyl transition metal complexes.

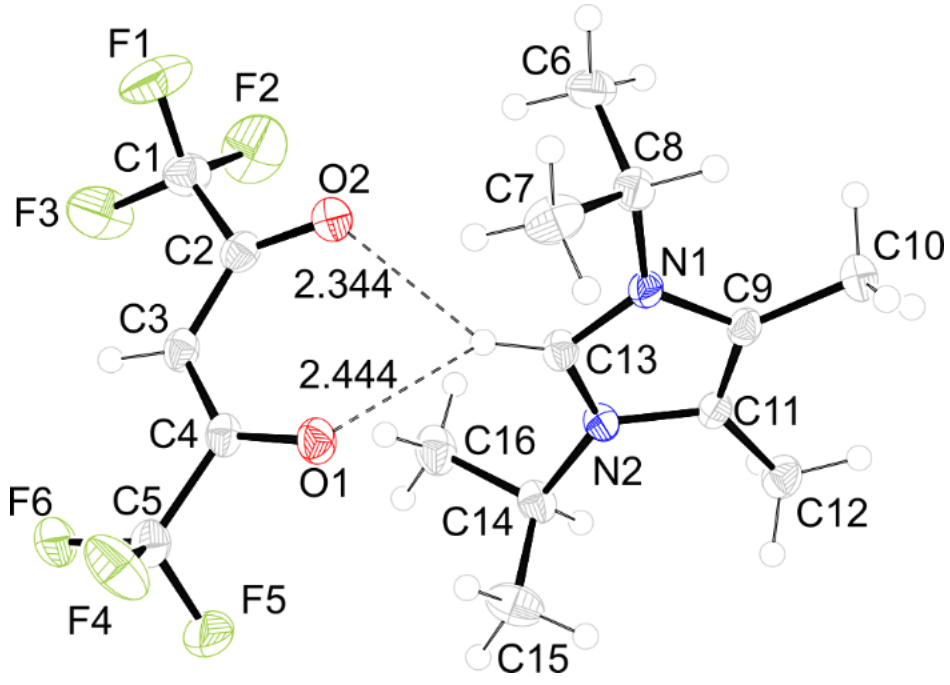

Figure 43. Perspective view of **19** with thermal ellipsoids at the 50% probability level.

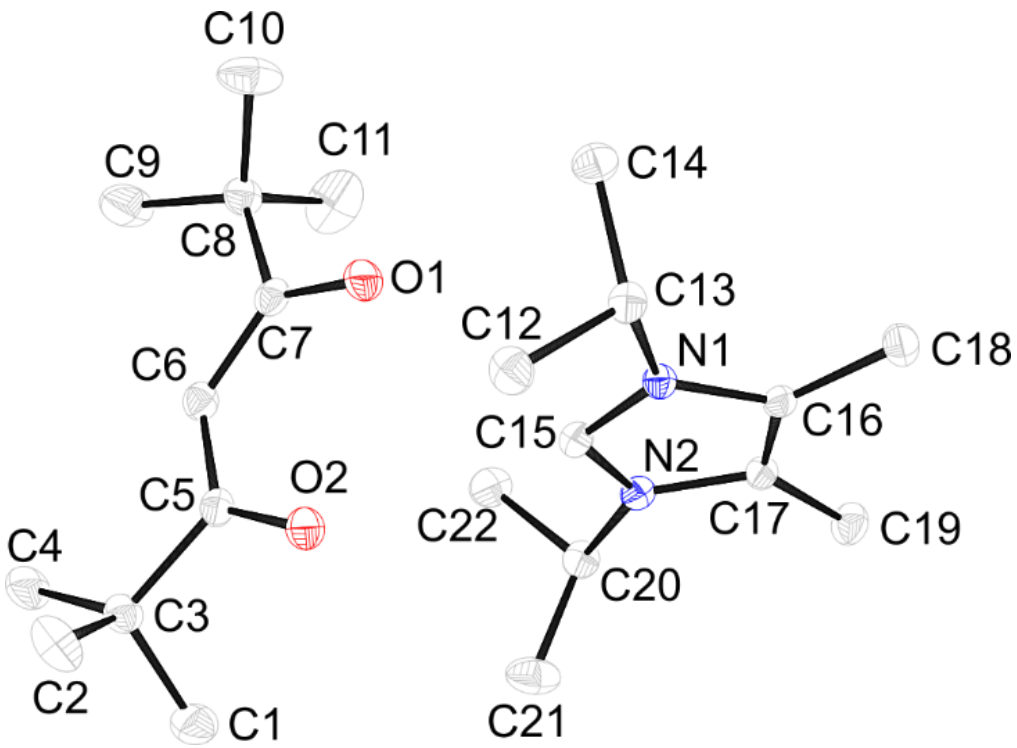

Figure 44. Perspective view of **20** with thermal ellipsoids at the 50% probability level.

The monomeric Ag(*β*-diketonate) crystal structures obtained herein can be compared with data from previously reported Ag(*β*-diketonate) phosphine and NHC adducts. The Ag(β-diketonate)NHC adducts such as Ag(1,3-diphenyl-1,3-propanedionate)(^{Me2}NHC) and Ag(1,3-dimethylacetonate)(^{Me2}NHC) have been reported.[183,205] The Ag-C bond length of Ag(1,3-diphenyl-1,3-propanedionate)(^{Me2}NHC) is 2.085(10) Å.[183] This distance is very similar to the observed Ag-C bond distances of **11**, **13**-**16**, and **18**. The Ag-C bond lengths obtained herein are also similar to the related distances in bis(1,3-dimesitylimidazole-2-ylidene)Ag(I) triflate.[175] Previously reported Ag(1,3-diphenyl-1,3-propanedionate)(^{Me2}NHC) is a dimer in the solid state, and has a Ag-Ag distance of 3.000 Å between two molecules. Complexes **13**, **14**, **15**, **16**, and **18** are monomers with no Ag-Ag interactions in their solid state structures. The formation of monomeric structures may be driven by the steric bulk of the substituents on the carbene and diketonate ligands. Previously reported Ag(*β*-diketonate) phosphine adducts show Ag-P bond lengths that varied from 2.311-2.346 Å.[64,124,130,132] Most of the reported Ag(*β*-diketonate) phosphine complexes are dimers in the solid state that contains Ag-Ag or Ag-O(*β*-diketonate) interactions. There are no Ag-Ag interactions in Ag(fod)(PEt_3) and the Ag-Ag distance is 3.490 Å.[64] However, the *β*-diketonate ligand coordinated to one Ag atom shares one oxygen atom with the second Ag atom. The Ag-O bond distance is 2.319(5) Å. This distance is within the sum of the van der Waals radii for Ag and O (~3.24 Å).[187]

Table 10. Experimental crystallographic data for **11**, **13**, and **14**.

	11	**13**	**14**
formula	$C_{14.8}H_{17.2}Ag_{1.2}F_{7.2}N_{1.6}O_{2.4}$	$C_{22}H_{39}AgN_2O_2$	$C_{19}H_{30}AgF_3N_2O_2$
fw	522.14	471.42	483.32
space group	C2/c	Pbca	$P2_1/n$
a (Å)	49.928(2)	18.2399(9)	8.7875(8)
b (Å)	13.6164(7)	13.8866(7)	18.6589(17)
c (Å)	21.6390(12)	18.5341(8)	13.2918(12)
V (Å^3)	13860.8(13)	4694.5(4)	2153.8(3)
Z	30	8	4
T (K)	100.1	100.1	100.0
λ (Å)	0.71073	0.71073	0.71073
ρ_{calc} (gcm^{-3})	1.877	1.334	1.490
μ (mm^{-1})	1.379	0.876	0.976
R(*F*)[a] (%)	2.71	2.43	2.52
Rw(*F*)[b] (%)	5.56	5.52	5.71

[a] $R(F) = \Sigma||F_o| - |F_c||/\Sigma|F_o|$. [b] $R_w(F^2) = [\Sigma w(F_o^2-F_c^2)^2/\Sigma w(F_o^2)^2]^{1/2}$.

Table 11. Experimental crystallographic data for **15**, **16**, and **18**.

	15	**16**	**18**
formula	$C_{16}H_{23}AgF_6N_2O_2$	$C_{21}H_{32}AgF_7N_2O_2$	$C_{19}H_{32}AgF_3N_2O_2$
fw	497.23	585.35	485.33
space group	$P2_1/c$	$P2_1/c$	P-1
a (Å)	19.2077(15)	11.9608(7)	9.8373(9)
b (Å)	11.5016(9)	9.9586(6)	10.1710(10)
c (Å)	19.6575(16)	20.7907(13)	12.5362(12)
V (Å^3)	3871.4(5)	2457.5(3)	1077.53(18)
Z	8	4	2
T (K)	100	100.0	100
λ (Å)	0.71073	0.71073	0.71073
ρ_{calc} (gcm^{-3})	1.706	1.582	1.496
μ (mm^{-1})	1.110	0.893	0.976
R(*F*)[a] (%)	3.77	2.24	2.82
Rw(*F*)[b] (%)	8.73	5.25	5.87

[a] $R(F) = \Sigma||F_o| - |F_c||/\Sigma|F_o|$. [b] $R_w(F^2) = [\Sigma w(F_o^2-F_c^2)^2/\Sigma w(F_o^2)^2]^{1/2}$.

Table 12. Experimental crystallographic data for **19** and **20**.

	19	**20**
formula	$C_{16}H_{22}F_6N_2O_2$	$C_{22}H_{40}N_2O_2$
fw	388.35	364.56
space group	$P2_12_12_1$	$P2_1/c$
a (Å)	8.6919(5)	13.1822(6)
b (Å)	12.1160(6)	10.0295(4)
c (Å)	17.7694(10)	17.4584(8)
V (Å^3)	1871.31(18)	2245.83(17)
Z	4	4
T (K)	100.1	100.1
λ (Å)	0.71073	0.71073
ρ_{calc} (gcm^{-3})	1.378	1.078
μ (mm^{-1})	0.131	0.068
R(*F*)[a] (%)	4.01	4.17
Rw(*F*)[b] (%)	8.54	9.92

[a] $R(F) = \Sigma||F_o| - |F_c||/\Sigma|F_o|$. [b] $R_w(F^2) = [\Sigma w(F_o^2-F_c^2)^2/\Sigma w(F_o^2)^2]^{1/2}$.

Table 13. Selected bond lengths (Å) and angles (deg) for **11**, **13**, and **14**.

	Ag-O (Å)	Ag-C (Å)	C-Ag-O (°)	O-Ag-O (°)
11	Ag1A-O1A 2.328(2) Ag1A-O2A 2.187(2) Ag2A-O3A 2.350(2) Ag2A-O4A 2.356(2) Ag3A-O5A 2.183(2) Ag3A-O6A 2.341(2)	Ag2A-C1A 2.360(2) Ag2A-C27A 2.381(2) Ag1A-C1A 2.124(2) Ag3A-C27A 2.119(2)	C1A-Ag1A-O1A 113.73(7) C1A0Ag1A-O2A 162.88(7) C1A-Ag2A-O3A 82.24(7) C1A-Ag2A-O4A 110.57(7) C27A-Ag3A-O5A 164.36(7) C27A-Ag3A-O6A 113.13(7) C27A-Ag2A-O3A 112.48(7) C27A-Ag2A-O4A 84.75(7)	O1A-Ag1A-O2A 83.35(6) O3A-Ag2A-O4A 78.94(6) O5A-Ag3A-O6A 82.42(6)
13	Ag1A-O1A 2.199(1) Ag1A-O2A 2.283(1)	Ag1-C12 2.064(2)	C1-Ag1-O1 147.22(6) C1-Ag1-O2 134.00(6)	O1-Ag-O2 78.66(5)
14	Ag1A-O1A 2.269(1) Ag1A-O2A 2.272(1)	Ag1-C1 2.072(2)	C1-Ag1-O1 141.78(5) C1-Ag1O2 140.17(5)	O1-Ag-O2 77.98(4)

Table 14. Selected bond lengths (Å) and angles (deg) for **15**, **16**, and **18**.

	Ag-O (Å)	Ag-C (Å)	C-Ag-O (°)	O-Ag-O (°)
15	Ag1A-O1A 2.277(2) Ag1A-O2A 2.303(3)	Ag1-C10 2.096(3) Ag2-C28 2.094(4)	C1-Ag1-O1 142.0(1) C1-Ag1O2 138.5(1) C28-Ag2-O3 134.9(1) C28-Ag2-O4 145.7(1)	O1-Ag-O2 79.46(9) O3-Ag2-O4 79.28(9)
16	Ag1A-O1A 2.174(1) Ag1A-O2A 2.367(1)	Ag1-C1 2.090(2)	C1-Ag1-O1 159.46(5) C1-Ag1-O2 119.91(5)	O1-Ag-O2 80.46(4)
18	Ag1A-O1A 2.228(1) Ag1A-O2A 2.296(1)	Ag1-C1 2.089(2)	C1-Ag1-O1 146.00(6) C1-Ag1-O2 133.69(6)	O1-Ag-O2 80.19(5)

Thermal Properties. The melting points, thermal decomposition temperatures, and sublimation data for **11-18** are shown in Table 15. The sublimation temperatures of **12-16** and **18** range from 100-124 °C at 0.2 Torr. Complexes **12**, **14**, **16**, and **18** have melting points that are lower than their sublimation temperatures. Therefore, a constant vapor delivery can be obtained from the uniform surface of liquids. Liquid precursors have a constant surface area, and hence constant gas phase precursor concentrations are obtained. However, the surface areas of solid precursors can change depending up loading and solids can create particles. Complexes **11** and **17** decomposed during the sublimation experiments. The decomposition temperatures of **11-18** vary from 141-188 °C. Complexes **15**, **16**, and **18** showed higher decomposition temperatures (180 to 188 °C) than **11-14**, and **17** (141 to 169 °C). The presence of two trifluoromethyl substituents on the diketonate ligand in **15** decreases the electron density on Ag ion, thereby increase the Lewis acidity. Electron-withdrawing ligands prevent the Ag(I) ion by the reduction and stabilize in the complex. Consequently, the highest thermal decomposition temperature in the series was observed for **15**. However, the thermal decomposition temperature of **11** is still lower than **15** due to the weakly coordinated NHCs, as observed in solid state structure. Thermal decomposition may involve dissociation of the NHC ligands. *Tert*-butyl groups enhance the electron density on the diketonate ligands and decrease the thermal stability of Ag(I) in the metal complex. The hfac ligand is less electron rich than the thd ligand, resulting a higher thermal stability in **15** than **17**. The thermal stabilities of these complexes can be compared with reported phosphine adducts. Thermal decomposition temperatures of selected Ag(*β*-diketonate) phosphine adducts are 170 °C for Ag(hfac)(PEt_3), 128 °C for Ag(hfac)(1,5-COD), 140 °C for Ag(fod)(PEt_3), and 200 °C for Ag(hfac)(PMe_3).[206] Complex **15** has higher thermal stability than analogous phosphine and alkene adducts of Ag(hfac)(PEt_3), Ag(fod)(PEt_3), and Ag(hfac)(1,5-COD). Previously reported

Ag(fod)(PEt_3) has lower thermal stability than the analogous precursors of **12** and **16** reported herein.

Table 15. Melting points, thermal decomposition temperatures, and sublimation temperatures for **11**-**18**.

Complex	Melting Point (°C)	Decomposition (°C)	Sublimation Temperature (0.2 Torr)
11	167-169	169	Decomposed
12	87-89	160	119
13	165-168	168	100
14	91-93	143	114
15	138-141	188	105
16	98-101	180	124
17	145-147	141	Decomposed
18	98-102	180	120

TGA determinations were carried out to understand the behavior of **11**-**18** upon heating. TGA plots of **11**-**18** are shown in Figures 45 and 46. TGAs showed that none of these NHC complexes evaporated completely, instead all decomposed at >250 °C to afford non-volatile residues. The TGA plot of **11** showed a two-step weight loss; the first step is due to the elimination of the ^{iPr2}NHC ligands, and the second step is due to the elimination of two hfac ligands. The residual mass (39%) is higher than the percent of Ag in the complex (25%). Non-volatile residues obtained in **13** (24%), **14** (21%), **16** (20%), **17** (23%), and **18** (20%) are equal to the percentage Ag in each complex (**13**, 23%; **14**, 22%; **16**, 18%; **17**, 23%; **18**, 22%). However, non-volatile

residues in **12** (31%) and **15** (27%) are higher than the percent of Ag in the complexes (**12**, 19%; **15**, 22%).

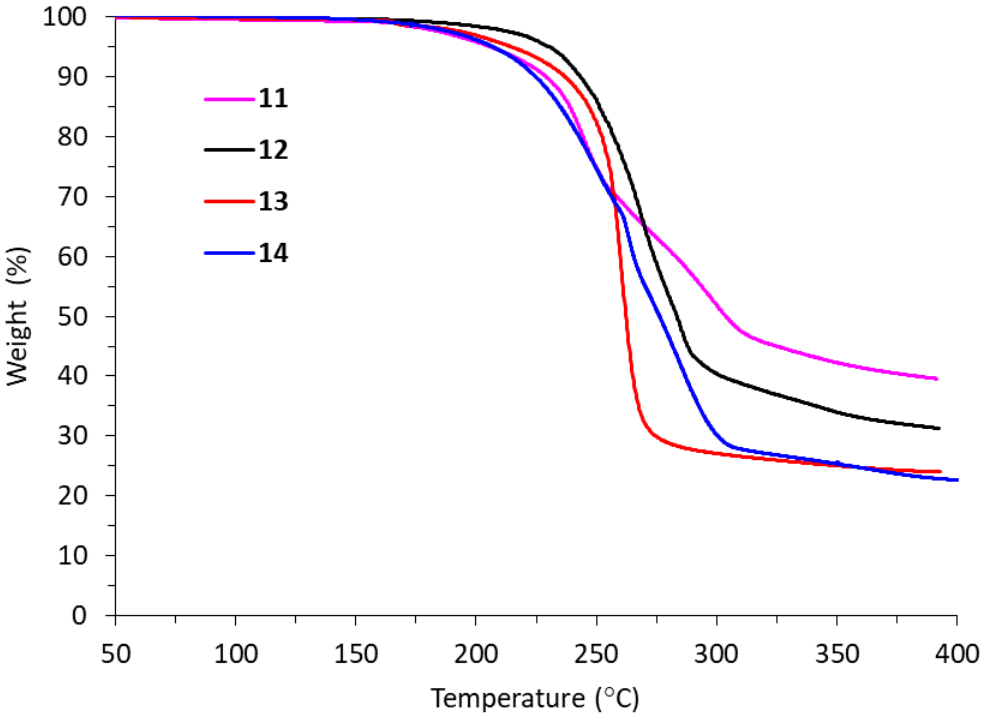

Figure 45. TGA traces of **11-14**.

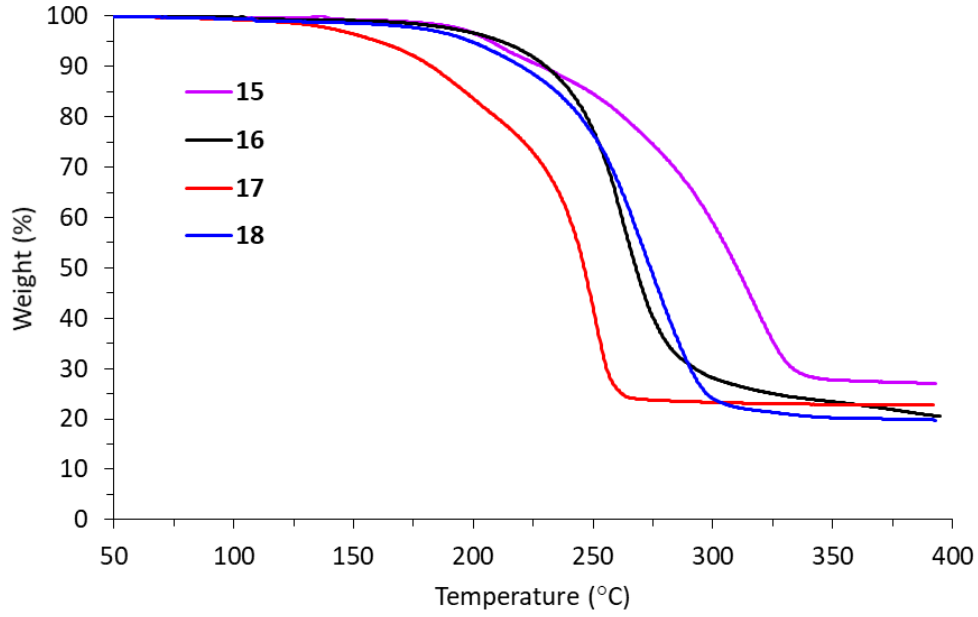

Figure 46. TGA traces of **15-18**.

4.3 Conclusions

The Ag(diketonate)(NHC) adducts reported herein include a trimer (**11**) and monomers (**13**, **14**, **15**, **16**, and **18**). The trimer contains close Ag-Ag interactions, while the monomers have no Ag-Ag interactions. Selected Ag complexes containing *β*-diketonate and NHCs such as Ag(1,3-diphenyl-1,3-propanedionate)(^{Me2}NHC) and Ag(1,3-dimethyl acetonate)(^{Me2}NHC) have been previously reported.[183,205] For instance, Ag(1,3-diphenyl-1,3-propanedionate)(^{Me2}NHC) is a dimer in the solid state. In the dimer, the carbene and the diketonate ligands arrange in a head-to-tail manner with argentophilic interactions. The Ag-Ag distance in Ag(1,3-diphenyl-1,3-propanedionate)(^{Me2}NHC) (3.00 Å)[183] is shorter than twice the van der Waals radius for the Ag atom (3.44 Å).[165] Preparation of Ag(*β*-diketonate) is necessary before treatment with the NHCs, because the one-pot synthesis using Ag_2O, NHC, and diketonate resulted in salts **19** and **20** containing stabilized carbenium ions with diketonate anions in the solid state. Previously reported imidazolium cyclopentadienides[203-204] are comparable to the stabilized carbenium ions with diketonate anions (**19** and **20**) reported herein.

All of the Ag(*β*-diketonate)(NHC) complexes synthesized herein do not evaporate entirely and decompose at >250 °C to afford nonvolatile residues. TGA traces obtained for **11**-**18** were compared with the TGA traces of reported Ag(*β*-diketonate) phosphine adducts.[64] TGA studies of most of the available precursors, including Ag(thd)(PEt_3), Ag(Piv)(PEt_3), Ag(hfac)(PMe_3), and Ag(fod)(PEt_3) revealed the compounds decomposed and left non-volatile residues. Among the NHC complexes, **15** showed the highest thermal stability in the series. The presence of trifluoromethyl substituents decreases the electron density on the *β*-diketonate ligand. The less electron rich hfac ligand in **15** increases the Lewis acidity of Ag(I) in the complex. Therefore, Ag(I) is stabilized by the electron-withdrawing anionic hfac ligand. In contrast to trifluoromethyl

substituents, *tert*-butyl substituents increase the electron density on the *β*-diketonate ligand. Therefore, the thd ligand is more electron rich and decreases the stability of Ag(I) in the complex. In the Ag(*β*-diketonate)(NHC) series, **17** showed the lowest thermal stability, which is consistent with the presence of the electron-rich thd ligand. Liquid precursors are preferred in ALD and CVD because liquid precursors offer a constant vapor pressure, whereas the vapor pressure of solids can change with the surface area of the precursor and the amount of precursor in the reservoir. Among Ag(*β*-diketonate)(NHC) adducts **12**, **14**, **16**, and **18** have melting points that are lower than their sublimation temperatures. Therefore **12**, **14**, **16**, and **18** sublime as liquids.

Ag(*β*-diketonate)(NHC) adducts can be compared with Ag(pz)(NHC) adducts and trimers (**1** and **2**) reported in Chapter 3. Complexes **12**-**16** and **18** have similar volatilities to **1** and **2** and Ag(pz)(NHC) adducts (**3**-**6**, **8**, **9**·Et_2O, and **10**). The thermal stabilities of **11**-**18** are lower than the thermal stabilities of **1**-**8**, **9**·Et_2O, and **10**. However, thermal decomposition temperatures of **11**-**18** are slightly higher or comparable to the reported Ag(*β*-diketonate) phosphine adducts such as Ag(hfac)(PEt_3) (170 °C), Ag(hfac)(1,5-COD) (128 °C), Ag(fod)(PEt_3) (140 °C), and Ag(hfac)(PMe_3) (200 °C).[206]

4.4 Experimental Section

General Considerations. The syntheses and manipulations of Ag complexes were carried out under argon, using ether a glove box or Schlenk line techniques. Hexane and toluene were distilled from sodium, and tetrahydrofuran and diethyl ether were distilled from purple solutions of sodium benzophenone ketyl. The Hpta, Hhfac, and Htta ligands were obtained from Sigma-Aldrich. The Hfod ligand was purchased from TCI chemicals. The Hthd ligand was purchased from Oakwood Chemicals. Silver oxide was purchased from Fischer Scientific. Silver nitrate was purchased from Sigma-Aldrich. Ag(diketonates), $Ag_4(hfac)_4(THF)_2$,[201-202] Ag(fod),[64] and

Ag(thd)[202] were prepared according to the literature procedures. Ag(pta) and Ag(tta) were synthesized using a similar procedure used to synthesized for Ag(fod). The unsaturated carbene ^{iPr2}NHC and saturated carbene ^{tBu2}NHC were prepared using published procedures.[180,184]

^{1}H NMR and ^{13}C{H} NMR spectra were obtained in deuterated benzene-d_6, chloroform-*d*, toluene-d_8, or dimethyl sulfoxide-d_6 as indicated and were referenced to the residual proton and carbon resonances of the solvents. Melting points and decomposition temperatures were determined on a Thermo Scientific Mel-Temp 3.0 digital melting point apparatus. TGA and DTA were carried out with a SDT 2960 TGA/DTA instrument. Infrared spectra were obtained from a SHIMADZU IRTracer-100. CHN microanalyses were performed by Midwest Microlab, Indianapolis, IN.

Preparation of Ag$_3$(hfac)$_3$(^{iPr2}NHC)$_2$ (11). A 100 mL Schlenk flask was charged with a magnetic stir bar, $Ag_4(hfac)_4(THF)_2$ (1.00 g, 0.712 mmol), and THF (30 mL). To this stirred solution at ambient temperature was slowly added a solution of 1,3-diisopropyl-4,5-dimethyl-1H-imidazol-3-ium-2-ide (0.518 g, 2.84 mmol) in THF (20 mL). This solution was stirred at ambient temperature for 1 h. The volatile components were removed under reduced pressure and the resulting pale brown paste was dissolved in diethyl ether (40 mL). The solution was filtered through a 2 cm pad of Celite on a coarse glass frit, and the filtrate was concentrated to about 30 mL under reduced pressure. Hexane (20 mL) was slowly added to form a layer on top. The flask was placed in a 4 °C refrigerator for 24 h to afford **11** as colorless crystals (51%): mp 167-169 °C, dec. 169 °C; ^{1}H NMR (benzene-d_6, 23 °C, δ) 6.30 (s, 2H, C-C***H***-C), 3.98 (septet, J = 7.0 Hz, 4H, N-C***H***$(CH_3)_2$), 1.33 (s, 12H, C-C***H***$_3$), 1.14 (d, J = 7.0 Hz, 24H, N-CH(C***H***$_3)_2$); ^{13}C{^{1}H} NMR (benzene-d_6, 23 °C, ppm) 177.31 (q, CF_3***C***-O, $^{2}J_{CF}$ = 32.0 Hz), 166.29 (s, ***C***-Ag), 126.28 (s, ***C***-CH_3), 118.37 (q, ***C***F$_3$, $^{1}J_{CF}$ = 288.8 Hz), 87.31 (s, ***C***H), 52.86 (s, N-***C***H$(CH_3)_2$), 22.63 (s, N-

CH(***C***H_3)$_2$), 8.84 (s, C-***C***H_3); IR (cm^{-1}) 2983 (w), 1651 (m), 1489 (m), 1373 (m), 1254 (m), 1128 (s), 787 (s), 663 (s).

Anal. Calc for $C_{37}H_{43}Ag_3F_{18}N_4O_6$: C, 34.04; H, 3.32; N, 4.29. Found: C, 34.02; H, 3.32; N, 4.29.

Preparation of Ag(fod)(*iPr2*NHC) (12). In a fashion similar to the preparation of **11**, treatment of Ag(fod) (1.45 g, 3.59 mmol) with 1,3-diisopropyl-4,5-dimethyl-1H-imidazol-3-ium-2-ide (0.650 g, 3.60 mmol) afforded **12** as a colorless crystalline solid (0.776 g, 37%) at -30 °C: mp 87-89 °C, dec. 160 °C; ^{1}H NMR (benzene-d_6, 23 °C, δ) 6.24 (s, 1H, C-C***H***-C), 4.09 (septet, J = 6.6 Hz, 2H, N-C***H***$(CH_3)_2$), 1.40 (s, 6H, C-C***H***$_3$), 1.27 (s, 9H, C(C***H***$_3$)$_3$), 1.24 (d, J = 6.6 Hz , 12H, N-CH(C***H***$_3$)$_2$); ^{13}C{^{1}H} NMR (benzene-d_6, 23 °C, ppm) 205.34 (s, ***C***-O), 174.66 (s, ***C***-Ag), 172.22 (t, ***C***-O), 123.88 (s, ***C***-CH_3), 119.13 (qt, ***C***F_3, $^1J_{CF}$ = 287.6 Hz, $^2J_{CF}$ = 34.3 Hz), 114.28 (m, ***C***F_2), 111.65 (m, ***C***F_2), 90.18 (m, ***C***H), 51.24 (s, N-***C***H$(CH_3)_2$), 42.68 (s, ***C***$(CH_3)_3$), 28.29 (s, C(***C***H_3)$_3$), 23.16 (s, N-CH(***C***H_3)$_2$), 8.86 (s, C-***C***H_3); IR (cm^{-1}) 2978 (m), 1628 (s), 1477 (s), 1323 (w), 1344 (m), 1217 (s), 1113 (s), 1061 (m), 961 (m), 906 (m), 831 (m), 754 (m).

Anal. Calc for $C_{21}H_{30}AgF_7N_2O_2$: C, 43.23; H, 5.18; N, 4.80. Found: C, 43.38; H, 5.20; N, 4.98.

Preparation of Ag(thd)(*iPr2*NHC) (13). In a fashion similar to the preparation of **11**, treatment of Ag(thd) (1.00 g, 3.43 mmol) with 1,3-diisopropyl-4,5-dimethyl-1H-imidazol-3-ium-2-ide (0.618 g, 3.43 mmol) afforded **13** as colorless crystals (0.326 g, 20%) at -30 °C. X-ray quality crystals were grown from hexane by slow cooling at 4 °C: mp 165-168 °C, dec. 168 °C; ^{1}H NMR (benzene-d_6, 23 °C, δ) 6.01 (s, 1H, C-C***H***-C), 4.2 (septet, J = 7.0 Hz, 2H, N-C***H***$(CH_3)_2$), 1.52 (s, 18H, C(C***H***$_3$)$_3$), 1.41 (s, 6H, C-C***H***$_3$), 1.30 (d, J = 7.0 Hz, 12H, N-CH(C***H***$_3$)$_2$); ^{13}C{^{1}H} NMR (benzene-d_6, 23 °C, ppm) 199.47 (s, ***C***-O), 176.83 (s, ***C***-Ag), 123.70 (s, ***C***-CH_3), 87.75 (s, ***C***H),

51.50 (s, N-***C***H(CH_3)$_2$), 42.10 (s, ***C***(CH_3)$_3$), 29.47 (s, C(***C***H_3)$_3$), 23.12 (s, N-CH(***C***H_3)$_2$), 9.04 (s, C-***C***H_3); IR (cm^{-1}) 2955 (m), 1583 (s), 1499 (m), 1406 (s), 1354 (m), 1227 (w), 864 (m), 783 (w), 747 (m).

Anal. Calc for $C_{22}H_{39}AgN_2O_2$: C, 56.05; H, 8.33; N, 5.94. Found: C, 57.07; H, 8.09; N, 6.11.

Preparation of Ag(pta)(*iPr2*NHC) (14). In a fashion similar to the preparation of **11**, treatment of Ag(pta) (1.00 g, 3.30 mmol) with 1,3-diisopropyl-4,5-dimethyl-1H-imidazol-3-ium-2-ide (0.594 g, 3.30 mmol) afforded **14** as colorless crystals (0.760 g, 48%). X-ray quality crystals were grown form hexane at -30 °C: mp 91-93 °C, dec. 143 °C; ^{1}H NMR (benzene-d_6, 23 °C, δ) 6.25 (s, 1H, C-C***H***-C), 4.10 (septet, J = 6.6 Hz, 2H, N-C***H***(CH_3)$_2$), 1.38 (s, 6H, C-C***H***$_3$), 1.28 (s, 9H, C(C***H***$_3$)$_3$), 1.22 (d, J = 6.6 Hz, 12H, N-CH(C***H***$_3$)$_2$); ^{13}C{^{1}H} NMR (benzene-d_6, 23 °C, ppm) 205.54 (s, ***C***-O), 171.77 (s, ***C***-Ag), 171.63 (q, ***C***-CF_3, $^2J_{CF}$ = 29.4 Hz), 123.94 (s, ***C***-CH_3), 120.65 (q, ***C***F_3, $^1J_{CF}$ = 288.8 Hz), 88.53 (s, *C*H), 51.40 (s, N-***C***H(CH_3)$_2$), 42.60 (s, ***C***(CH_3)$_3$), 28.32 (s, C(***C***H_3)$_3$), 23.17 (s, N-CH(***C***H_3)$_2$), 8.91 (s, C-***C***H_3); IR (cm^{-1}) 2970 (w), 1626 (s), 1474 (m), 1362 (w), 1288 (m), 1246 (w), 1167 (s), 1123 (s), 846 (m), 785 (m), 750 (w).

Anal. Calc for $C_{19}H_{30}AgF_3N_2O_2$: C, 47.22; H, 6.26; N, 5.79. Found: C, 47.18; H, 6.31; N, 5.90.

Preparation of Ag(hfac)(*tBu2*NHC) (15). In a fashion similar to the preparation of **11**, treatment of Ag_4(hfac)$_4$(THF)$_2$ (1.00 g, 0.712 mmol) with 1,3-di-*tert*-butylimidazolidine (0.520 g, 2.85 mmol) afforded **15** as colorless crystals (0.456 g, 32%) at -30 °C: mp 138-141 °C, dec. 188 °C; ^{1}H NMR (benzene-d_6, 23 °C, δ) 6.35 (s, 1H, C-C***H***-C), 2.56 (s, 4H, N-C***H***$_2$C***H***$_2$-N*)*, 1.10 (s, 18H, N-(C***H***$_3$)$_3$); ^{13}C{^{1}H} NMR (benzene-d_6, 23 °C, ppm) 202.42 (s, ***C***-Ag), 177.39 (q, ***C***-CF_3, $^2J_{CF}$ = 31.4 Hz), 118.8 (q, ***C***F_3, $^1J_{CF}$ = 289.1 Hz), 87.47 (s, ***C***H), 54.76 (s, N-***C***H_2), 45.32 (s, N-

C$(CH_3)_3$), 30.14 (s, C(***C***$H_3)_3$); IR (cm^{-1}) 2970 (m), 1651 (s), 1500 (s), 1433 (s), 1366 (w), 1250 (s), 1178 (s), 1126 (s), 941 (w), 783 (s).

Anal. Calc for $C_{16}H_{23}AgF_6N_2O_2$: C, 38.65; H, 4.66; N, 5.63. Found: C, 35.04; H, 4.34; N, 4.78.

Preparation of Ag(fod)(*^{tBu2}*NHC) (16). In a fashion similar to the preparation of **11**, treatment of Ag(fod) (1.00 g, 2.48 mmol) with 1,3-di-*tert*-butylimidazolidine (0.452 g, 2.47 mmol) afforded **16** as colorless crystals (0.316 g, 22%): mp 98-101 °C, dec. 180 °C; ^{1}H NMR (benzene-d_6, 23 °C, δ) 6.21 (s, 1H, C-C***H***-C), 2.60 (s, 4H, N-C***H***$_2$C***H***$_2$-N*)*, 1.26 (s, 9H, C(C***H***$_3)_3$), 1.19 (s, 18H, N-(C***H***$_3)_3$); ^{13}C{^{1}H} NMR (benzene-d_6, 23 °C, ppm) 205.51 (s, ***C***-O), 204.33 (s, ***C***-Ag), 172.36 (t, ***C***-O), 123.88 (s, ***C***-CH_3), 119.13 (qt, ***C***F_3, $^1J_{CF}$ = 287.2 Hz, $^2J_{CF}$ = 34.7 Hz), 114.17 (m, ***C***F_2), 111.54 (m, ***C***F_2), 89.90 (m, ***C***H), 54.88 (s, N-***C***H_2), 45.35 (s, N-***C***$(CH_3)_3$), 42.61 (s, ***C***$(CH_3)_3$), 30.19 (s, C(***C***$H_3)_3$), 28.27 (s, N-C(***C***$H_3)_2$); IR (cm^{-1}) 2963 (w), 1632 (s), 1475 (m), 1342 (m), 1217 (s), 1113 (s), 906 (m), 831 (w), 781 (w), 737 (w).

Anal. Calc for $C_{21}H_{32}AgF_7N_2O_2$: C, 43.09; H, 5.51; N, 4.78. Found: C, 43.32; H, 5.39; N, 4.76.

Preparation of Ag(thd)(*^{tBu2}*NHC) (17). In a fashion similar to the preparation of **11**, treatment of Ag(thd) (0.51 g, 1.73 mmol) with 1,3-di-*tert*-butylimidazolidine (0.317 g, 1.73 mmol) for 18 h afforded **17** as a colorless solid (0.170 g, 20%) upon crystallization from diethyl ether/hexane (1:1) at -30 °C: mp 145-147 °C, dec. 141 °C; ^{1}H NMR (benzene-d_6, 23 °C, δ) 5.89 (s, 1H, C-C***H***-C), 2.66 (s, 4H, N-C***H***$_2$C***H***$_2$-N*)*, 1.46 (s, 18H, C(C***H***$_3)_3$), 1.27 (s, 18H, N-(C***H***$_3)_3$); ^{13}C{^{1}H} NMR (benzene-d_6, 23 °C, ppm) 199.73 (s, ***C***-O), 123.88 (s, ***C***-CH_3), 87.34 (s, ***C***H), 54.97 (s, N-***C***H_2), 45.37 (s, N-***C***$(CH_3)_3$), 42.01 (s, ***C***$(CH_3)_3$), 30.32 (s, C(***C***$H_3)_3$), 29.43 (s, N-C(***C***$H_3)_2$);

IR (cm^{-1}) 29861 (m), 1584 (s), 1528 (w), 1474 (w), 1404 (s), 1354 (m), 1271 (m), 1204 (m), 1128 (w), 864 (m), 783 (w), 752 (w).

Anal. Calc for $C_{22}H_{41}AgN_2O_2$: C, 55.81; H, 8.73; N, 5.92. Found: C, 57.14; H, 8.70; N, 6.03.

Preparation of Ag(pta)(^{tBu2}NHC) (18). In a fashion similar to the preparation of **11**, treatment of Ag(pta) (1.00 g, 3.30 mmol) with 1,3-di-*tert*-butylimidazolidine (0.601 g, 3.29 mmol) afforded **18** as colorless crystals (0.650 g, 41%) upon crystallization from hexane at 4 °C: mp 98-102 °C, dec. 180 °C; ^{1}H NMR (benzene-d_6, 23 °C, δ) 6.18 (s, 1H, C-C***H***-C), 2.62 (s, 4H, N-C***H***$_2$C***H***$_2$-N*)*, 1.25 (s, 9H, C(C***H***$_3$)$_3$), 1.04 (s, 18H, N-(C***H***$_3$)$_3$); ^{13}C{^{1}H} NMR (benzene-d_6, 23 °C, ppm) 205.78 (s, ***C***-O), 204.34 (s, ***C***-Ag) 172.02 (q, ***C***-CF_3, $^2J_{CF}$ = 29.4 Hz), 120.5 (q, ***C***F_3, $^1J_{CF}$ = 289.2 Hz), 87.99 (s, ***C***H), 54.88 (s, N-***C***H_2), 45.38 (s, N-***C***$(CH_3)_3$), 42.57 (s, ***C***$(CH_3)_3$), 30.26 (s, C(***C***$H_3)_3$), 28.32 (s, N-C(***C***$H_3)_2$); IR (cm^{-1}) 2968 (m), 1624 (s), 1472 (s), 1364 (m), 1277 (s), 1244 (w), 1163 (s), 112 (s), 845 (m), 785 (m).

Anal. Calc for $C_{19}H_{32}AgF_3N_2O_2$: C, 47.02; H, 6.64; N, 5.77. Found: C, 47.21; H, 6.62; N, 5.77.

Preparation of [^{iPr2}NHC][hfac] (19). A 100-mL Schlenk flask was charged with a magnetic stir bar, Ag_2O (0.500 g, 2.16 mmol), and diethyl ether (20 mL). To this stirred solution at ambient temperature was slowly added a solution of 1,3-diisopropyl-4,5-dimethyl-1H-imidazol-3-ium-2-ide (0.776 g, 4.31 mmol) in diethyl ether (15 mL). To this reaction mixture was slowly added dropwise a solution of Hhfac (0.897 g, 4.31 mmol) in diethyl ether (5 mL). This solution was stirred at ambient temperature for 4 h. Unreacted Ag_2O was removed by filtration. The volatile components were removed under reduced pressure and the resulting orange solid was dissolved in diethyl ether (30 mL). The solution was filtered through a 2 cm pad of Celite on a coarse glass frit,

and the filtrate was concentrated to about 20 mL under reduced pressure. The flask was placed in a -30 °C freezer for 48 h to obtain **19** as pale yellow, X-ray quality crystals (7%): mp 110-112 °C, dec. 240 °C; ^{1}H NMR (benzene-d_6, 23 °C, δ) 10.96 (s, 1H, ***H***), 6.41 (s, 1H, C-C***H***-C), 3.52 (septet, J = 6.6 Hz, 2H, N-C***H***$(CH_3)_2$), 1.23 (d, J = 6.6 Hz, 12H, N-CH(C***H***$_3)_2$),1.17 (s, 6H, C-C***H***$_3$); ^{13}C{^{1}H} NMR (benzene-d_6, 23 °C, ppm) 173.96 (q, CF_3***C***-O, $^{2}J_{CF}$ = 30.1 Hz), 136.87 (s, ***C***-Ag), 124.07 (s, ***C***-CH_3), 119.62 (q, ***C***F_3, $^{1}J_{CF}$ = 292.1 Hz), 84.75 (s, ***C***H), 50.70 (s, N-***C***H$(CH_3)_2$), 21.03 (s, N-CH(***C***$H_3)_2$), 7.40 (s, C-***C***H_3); IR (cm^{-1}) 3122 (w), 3037 (m), 1666 (s), 1550 (s), 1529 (s), 1444 (m), 1244 (s), 1168 (m), 1112 (s), 937 (m), 785 (s).

Anal. Calc for $C_{16}H_{22}F_6N_2O_2$: C, 49.48; H, 5.71; N, 7.21. Found: C, 49.52; H, 5.64; N, 7.24.

Preparation of [*^{iPr2}*NHC][thd] (20). In a fashion similar to the preparation of **19**, treatment of Ag_2O (0.509 g, 2.19 mmol) with 1,3-diisopropyl-4,5-dimethyl-1H-imidazol-3-ium-2-ide (0.786 g, 4.36 mmol) and Hthd (0.795 g, 4.31 mmol) afforded **20** as pale yellow, X-ray quality crystals (49%): mp 167-170 °C, dec. 209 °C; ^{1}H NMR (benzene-d_6, 23 °C, δ) 13.09 (s, 1H, ***H***), 5.94 (s, 1H, C-C***H***-C), 3.75 (septet, J = 6.6 Hz, 2H, N-C***H***$(CH_3)_2$), 1.59 (s, 18H, C(C***H***$_3)_3$, 1.43 (d, J = 6.6 Hz, 12H, N-CH(C***H***$_3)_2$),1.20 (s, 6H, C-C***H***$_3$); ^{13}C{^{1}H} NMR (benzene-d_6, 23 °C, ppm) 194.64 (s, ***C***-O), 142.65 (s, ***C***-Ag), 122.97 (s, ***C***-CH_3), 84.60 (s, ***C***H), 50.72 (s, N-***C***H$(CH_3)_2$), 41.38 (s, ***C***$(CH_3)_3$), 29.90 (s, C(***C***$H_3)_3$), 22.23 (s, N-CH(***C***$H_3)_2$), 7.64 (s, C-***C***H_3); IR (cm^{-1}) 2939 (m), 2358 (w), 1595 (s), 1421(s), 1352 (s), 1260 (s), 1180 (s), 1114 (s), 856 (m), 727 (s).

Anal. Calc for $C_{22}H_{40}N_2O_2$: C, 72.48; H, 11.06; N, 7.68. Found: C, 72.28; H, 11.03; N, 7.74.

CHAPTER 5
CONCLUSIONS AND FUTURE DIRECTIONS

This dissertation focuses on the syntheses, characterization, and precursor property evaluation of trimeric Ag pyrazolates and several new Ag precursors. Treatment of silver oxide with bis(trifluoromethyl)pyrazole and (3-*tert*-butyl-5-perfluoropropyl)pyrazole afforded **1** and **2**, respectively. Trimers **1** and **2** were treated with four different types of NHCs to synthesize Ag(pz)(NHC) adducts (**3**-**8**, **9**·Et_2O, and **10**). Ag(*β*-diketonate)(NHC) adducts **11**-**18** were prepared using Ag(*β*-diketonate) and NHC ligands. These complexes were characterized by ^{1}H and ^{13}C NMR spectroscopy, infrared spectroscopy, CHN elemental analyses, melting point and thermal decomposition experiments, TGA, and single crystal X-ray diffraction analysis.

Complex **1** was assessed as a promising ALD precursor with high thermal stability, volatility, and reactivity towards several reducing agents. Complex **1** was used with 1,1-dimethylhydrazine to deposit silver metal films on SiO_2 substrates at 180 °C with a growth rate of 0.82 Å/cycle (Chapter 2). A plot of growth rate versus substrate temperature showed an ALD window of 170 to 220 °C. Saturative self-limited growth was demonstrated for both **1** and 1,1-dimethylhydrazine at 180 °C. The as-deposited films were crystalline Ag metal. Due to the island type growth, SEM thickness measurements, as well as XRF Ag concentration measurements, were obtained to confirm ALD type growth. XRF measurements showed that the thermal ALD process has a nucleation delay of about 125 cycles. Nucleation delay is a common problem in noble metal film depositions.[34] Ag atoms migrate on the substrate surface even at room temperature to find another energetically favorable nucleation site, thereby make Ag islands with gaps. Consequently, the use of noble metal substrates such as Ru or Au may provide a strong bond between silver atoms and the substrate surface, which could minimize the mobility of Ag atoms. This approach may

lead to the formation of a continuous film rather than nanoparticles. In this thermal ALD study, thicker films consist of particles with different sizes, which resulted from coalescence and continued nucleation. Therefore, by increasing the number of deposition cycles may continue the nucleation on SiO_2 substrates and may deposit continuous Ag thin film. Deposition experiments with **2** have not been carried out to date. However, **2** also offers good volatility (120 °C/0.2 Torr) and high thermal stability (245 °C).

Monomeric precursors are preferred in ALD because they offer high volatility due to lower molecular weights. Chapter 3 explored the use of **1** and **2** as starting materials to synthesize monomeric silver pyrazolates. Complexes **1** and **2** reacted with NHCs to afford **3**-**8**, **9**·Et_2O, and **10** as colorless crystalline solids. Complexes crystallized as dimers (**3**-**5**), monomers (**8** and **10**) and a tetramer (**9**·Et_2O). Close Ag-Ag interactions observed in dimers and Ag-Ag distances varied from 3.030-3.391 Å. These distances are shorter than twice the van der Waals radius for the Ag atom (3.44 Å),[165] and thus, argentophilic interactions were observed. Remarkably, the trimeric pyrazolates **1** and **2** and the NHC adducts **3**-**6**, **8**, **9**·Et_2O, and **10** sublimed in a similar temperature range. Possibly, the trimers sublime as monomers or dimers. Thermal decomposition temperatures and TGA plots of **3**-**8**, **9**·Et_2O, and **10** suggest that the presence of electron-withdrawing substituents on both positions of the pyrazolate rings affords more thermal stability to Ag(pz)(NHC) complexes. Electron-withdrawing trifluoromethyl groups pull electron density away from the metal center and are poorer reducing agents for the Ag ion, thereby increasing the thermal stability of the complexes. Among the **3**-**8**, **9**·Et_2O, and **10**, only **4** has higher thermal stability than the parent trimer. As an improvement over trimers, **3**-**6**, **8**, and **9**·Et_2O have melting points that are lower than the sublimation temperatures and are thus delivered from the liquid state.

Liquid precursors have constant surface area and high vapor pressures. Therefore constant vapor delivery from the liquid state can be obtained throughout the deposition process.

Chapter 4 discussed the use of NHCs to synthesize monomeric silver diketonate complexes. The Ag-carbene bond lengths are compared with Ag-phosphine bond lengths in order to explain the strong coordination of NHCs. Single crystal X-ray structure determinations showed that **13-16** and **18** are monomers while **11** is a trimer. Argentophilic interactions were not observed in any monomers reported herein. As discussed in section 1.4.2, most of the known silver precursors contain an anionic *β*-diketonate and a neutral phosphine or alkene donor ligand. The use of saturated or unsaturated carbenes has no significant effect on the volatilities of the complexes. However, the Ag-$C_{(carbene)}$ bond distances (2.096-2.0644 Å) are not significantly different in **11**-**18**. Among the Ag(diketonate)(NHC) complexes that were prepared, **15** showed the highest thermal stability, which is still lower than the thermal stabilities of the trimers **1** and **2** and NHC adducts **3**-**8**, **9**·Et_2O, and **10**. The presence of a diketonate ligand with two electron-withdrawing trifluoromethyl substituents and saturated carbene may enhance the stability of **15**.

Similar NHC based-Ag(pyrazolate) and Ag(diketonate) precursors have not been reported prior to the work completed in this thesis. The structural diversity of **3**-**5**, **8**, **9•**(Et_2O), and **10** and **11**, **13**-**16**, and **18** complexes was explored. The presence of bulky substituents on the pyrazolate or diketonate carbon atoms minimizes the argentophilic interactions. Interestingly, **1**-**6**, **8**, **9**·Et_2O, **10, 12**-**16,** and **18** showed similar volatilities at 0.2 Torr. The presence of electron-withdrawing substituents in the ligands enhanced the stability of the resultant metal complexes. However, trimers **1** and **2** have higher thermal stabilities than **3**-**8**, **9**·Et_2O, and **10**-**18**.

REFERENCES

1. Jindal, R. *IEEE Trans. Electron Devices* **2001**, *48*, 2453-2454.
2. Moore, G. E. *Electronics* **1965**, 114-117.
3. International Technology Roadmap for Semiconductors http://www.itrs.net/.
4. Leskelä, M.; Ritala, M. *Angew. Chem. Int. Ed.* **2003**, *42*, 5548-5554.
5. Knisley, T. J.; Kalutarage, L. C.; Winter, C. H. *Coord. Chem. Rev.* **2013**, *257*, 3222-3231.
6. Johnson, R. W.; Hultqvist, A.; Bent, S. F. *Mater. Today* **2014**, *17*, 236-246.
7. Hsia, S. L.; Tan, T. Y.; Smith, P.; McGuire, G. E. *J. Appl. Phys.* **1992**, *72*, 1864-1873.
8. Lindsay, R.; Lauwers, A.; De Potter, M.; Roelandts, N.; Vrancken, C.; Maex, K. *Microelectron. Eng.* **2001**, *55*, 157-162.
9. Li, Z.; Gordon, R. G.; Pallem, V.; Li, H.; Shenai, D. V. *Chem. Mater.* **2010**, *22*, 3060-3066.
10. Kwo, J.; Hong, M.; Kortan, A. R.; Queeney, K. T.; Chabal, Y. J.; Mannaerts, J. P.; Boone, T.; Krajewski, J. J.; Sergent, A. M.; Rosamilia, J. M. *Appl. Phys. Lett.* **2000**, *77*, 130-132.
11. Leskelä, M.; Ritala, M. *J. Solid State Chem.* **2003**, *171*, 170-174.
12. Wilk, G. D.; Wallace, R. M.; Anthony, J. *J. Appl. Phys.* **2001**, *89*, 5243-5275.
13. Kim, H. *Surf. Coat. Technol.* **2006**, *200*, 3104-3111.
14. Roule, A.; Amuntencei, M.; Deronzier, E.; Haumesser, P. H.; Da Silva, S.; Avale, X.; Pollet, O.; Baskaran, R.; Passemard, G. *Microelectron. Eng.* **2007**, *84*, 2610-2614.
15. Kelsey, J. E.; Goldberg, C.; Nuesca, G.; Peterson, G.; Kaloyeros, A. E.; Arkles, B. *J. Vac. Sci. Technol. B* **1999**, *17*, 1101-1104.
16. Sim, H. S.; Kim, S.-I.; Kim, Y. T. *J. Vac. Sci. Technol. B* **2003**, *21*, 1411-1414.
17. Lee, B. H.; Yong, K. *J. Vac. Sci. Technol. B* **2004**, *22*, 2375-2379.

18. McElwee-White, L. *Dalton Trans.* **2006**, 5327-5333.

19. Won, Y. S.; Kim, Y. S.; Anderson, T. J.; Reitfort, L. L.; Ghiviriga, I.; McElwee-White, L. *J. Am. Chem. Soc.* **2006**, *128*, 13781-13788.

20. Dezelah, C. L.; El-Kadri, O. M.; Kukli, K.; Arstila, K.; Baird, R. J.; Lu, J.; Niinistö, L.; Winter, C. H. *J. Mater. Chem.* **2007**, *17*, 1109-1116.

21. Wang, S.-Q. *MRS Bull.* **1994**, *19*, 30-40.

22. Kim, H. *J. Vac. Sci. Technol. B* **2003**, *21*, 2231-2261.

23. Usui, T.; Nasu, H.; Takahashi, S.; Shimizu, N.; Nishikawa, T.; Yoshimaru, M.; Shibata, H.; Wada, M.; Koike, J. *IEEE Trans. Electron. Dev.* **2006**, *53*, 2492-2499.

24. Haneda, M.; Iijima, J.; Koike, J. *J. Appl. Phys. Lett.* **2007**, *90*, 252107.

25. Chu, J. P.; Lin, C. H; John, V. S. *Appl. Phys. Lett.* **2007**, *91*, 132109.

26. Barmak, K.; Cabral Jr, C.; Rodbell, K. P.; Harper, J. M. E. *J. Vac. Sci. Technol. B* **2006**, *24*, 2485-2498.

27. Koike, J.; Wada, M. *Appl. Phys. Lett.* **2005**, *87*, 041911.

28. Kalutarage, L. C.; Clendenning, S. B.; Winter, C. H. *ECS Trans.* **2014**, *64*, 147-157.

29. Rossnagel, S. M. *J. Vac. Sci. Technol. A* **2003**, *21*, S74-S87.

30. Gladfelter, W. L. *Chem. Mater.* **1993**, *5*, 1372-1388.

31. Gates, S. M. *Chem. Rev.* **1996**, *96*, 1519-1532.

32. Doppelt, P. *Coord. Chem. Rev.* **1998**, *178*, 1785-1809.

33. Hatanpää, T.; Ritala, M.; Leskelä, M. *Coord. Chem. Rev.* **2013**, *257*, 3297-3322.

34. Koponen, S. E.; Gordon, P. G.; Barry, S. T. *Polyhedron* **2016**, *108*, 59-66.

35. Van Bui, H.; Grillo, F.; Van Ommen, J. R. *Chem. Commun.* **2017**, *53*, 45-71.

36. Barry, S. T.; Teplyakov, A. V.; Zaera, F. *Acc. Chem. Res.* **2018**, *51*, 800-809.

37. George, S. M. *Chem. Rev.* **2010**, *110*, 111-131.

38. Martin, P. M. *Handbook of deposition technologies for films and coatings: science, applications and technology;* Elsevier Inc.: 2009.

39. Rossnagel, S. M.; Sherman, A.; Turner, F. *J. Vac. Sci. Technol. B* **2000**, *18*, 2016-2020.

40. Pierson, H. O. *Handbook of Chemical Vapor Deposition (CVD);* Noyes Publications/William Andrew Publishing: NY, 1999.

41. Zaima, S.; Furuta, T.; Yasuda, Y.; Iida, M. *J. Electrochem. Soc.* **1990**, *137*, 1297.

42. Varhue, W. J.; Andry, P. S.; Rogers, J. L.; Adams, E.; Kontra, R.; Lovioe, M. *Solid State Technol.* **1996**, *39*, 163-168.

43. Creighton, J. R.; Parmeter, J. E. *Crit. Rev. Solid State Mater. Sci.* **1993**, *18*, 175-237.

44. Puurunen, R. L. *Chem. Vap. Dep.* **2014**, *20*, 332-344.

45. Suntola, T.; Hyvarinen, J. *J. Annu. Rev. Mater. Res.* **1985**, *15*, 177-195.

46. Knez, M.; Nielsch, K.; Niinistö, L. *Adv. Mater.* **2007**, *19*, 3425-3438.

47. Leskelä, M.; Ritala, M. *Thin Solid Films* **2002**, *409*, 138-146.

48. Niinistö, L.; Nieminen, M.; Päiväsaari, J.; Niinistö, J.; Putkonen, M.; Nieminen, M. *Phys. Status Solidi A* **2004**, *201*, 1443-1452.

49. Puurunen, R. L. *J. Appl. Phys.* **2005**, *97*, 9.

50. Hultqvist, A.; Edoff, M.; Törndahl, T. *Prog. Photovoltaics Res. Appl.* **2011**, *19*, 478-481.

51. Kosola, A.; Putkonen, M.; Johansson, L.-S.; Niinistö, L. *Appl. Surf. Sci.* **2003**, *211*, 102-112.

52. Wang, H.; Wang, J.-J.; Gordon, R.; Lehn, J.-S. M.; Li, H.; Hong, D.; Shenai, D. V. *Electrochem. Solid-State Lett.* **2009**, *12*, G13-G15.

53. Miikkulainen, V.; Leskelä, M.; Ritala, M.; Puurunen, R. L. *J. Appl. Phys.* **2013**, *113*, 2.

54. Profijt, H. B.; Potts, S. E.; Van De Sanden, M. C. M.; Kessels, W. M. M. *J. Vac. Sci. Technol. A* **2011**, *29*, 050801.

55. Kim, H.; Rossnagel, S. M. *J. Vac. Sci. Technol. A* **2002**, *20*, 802-808.

56. Kim, H.; Rossnagel, S. M. *Thin Solid Films* **2003**, *441*, 311-316.

57. Sedai, B.; Heeg, M. J.; Winter, C. H. *J. Organomet. Chem.* **2008**, *693*, 3495-3503.

58. Sedai, B.; Heeg, M. J.; Winter, C. H. *Organometallics* **2009**, *28*, 1032-1038.

59. Kalutarage, L. C.; Heeg, M. J.; Martin, P. D.; Saly, M. J.; Kuiper, D. S.; Winter, C. H. *Inorg. Chem.* **2013**, *52*, 1182-1184.

60. Zaera, F. *J. Phys. Chem. Lett.* **2012**, *3*, 1301-1309.

61. Kim, J.; Iivonen, T.; Hämäläinen, J.; Kemell, M.; Meinander, K.; Mizohata, K.; Wang, L.; Räisänen, J.; Beranek, R.; Leskelä, M.; Devi, A. *Chem. Mater.* **2017**, *29*, 5796-5805.

62. Klesko, J. P.; Kerrigan, M. M.; Winter, C. H. *Chem. Mater.* **2016**, *28*, 700-703.

63. Kerrigan, M. M.; Klesko, J. P.; Winter, C. H. *Chem. Mater.* **2017**, *29*, 7458-7466.

64. Kariniemi, M.; Niinistö, J.; Hatanpää, T.; Kemell, M.; Sajavaara, T.; Ritala, M.; Leskelä, M. *Chem. Mater.* **2011**, *23*, 2901-2907.

65. Kim, H. *Thin Solid Films* **2011**, *519*, 6639-6644.

66. Kalutarage, L. C.; Martin, P. D.; Heeg, M. J.; Winter, C. H. *J. Am. Chem. Soc.* **2013**, *135*, 12588-12591.

67. Van, T. T.; Chang, J. P. *Surf. Sci.* **2005**, *596*, 1-11.

68. Elam, J. W.; Baker, D. A.; Hryn, A. J.; Martinson, A. B. F.; Pellin, M. J.; Hupp, J. T. *J Vac. Sci. Technol. A* **2008**, *26*, 244-252.

69. Edelstein, D.; Uzoh, C.; Jr, C. C.; DeHaven, P.; Buchwalter, P.; Simon, A.; Cooney, E.; Malholtra, S.; Klaus, D.; Rathore, H.; Ararwala, B.; Nguyen, D. In *A High Performance*

Liner for CopperDamascene Interconnects, Proc. of the IEEE International Interconnect Technology Conference, Burlingame, CA, Burlingame, CA, June 4-6, 2001.

70. Suntola, T. *Thin Solid Films* **1992**, 84−89.

71. Mårtensson, P.; Carlsson, J. O. *Chem. Vap. Deposition* **1997**, *3*, 45-50.

72. Juppo, M.; Ritala, M.; Leskelä, M. *J. Vac. Sci. Technol. A* **1997**, *15*, 2330-2333.

73. Solanki, R.; Pathangey, B. *Electrochem. Solid-State Lett.* **2000**, *3*, 479.

74. Lim, B. S.; Rahtu, A.; Gordon, R. G. *Nat. Mater.* **2003**, *2*, 749-754.

75. Lee, B. H.; Hwang, J. K.; Nam, J. W.; Lee, S. U.; Kim, J. T.; Koo, S. M.; Baunemann, A.; Fischer, R. A.; Sung, M. M. *Angew. Chem. Int. Ed.* **2009**, *48*, 4536-4539.

76. Vidjayacoumar, B.; Emslie, D. J. H.; Clendenning, S. B.; Blackwell, J. M.; Britten, J. F.; Rheingold, A. *Chem. Mater.* **2010**, *22*, 4844-4853.

77. Knisley, T. J.; Ariyasena, T. C.; Sajavaara, T.; Saly, M. J.; Winter, C. H. *Chem. Mater.* **2011**, *23*, 4417-4419.

78. Kalutarage, L. C.; Clendenning, S. B.; Winter, C. H. *Chem. Mater.* **2014**, *26*, 3731-3738.

79. Väyrynen, K.; Mizohata, K.; Räisänen, J.; Peeters, D.; Devi, A.; Ritala, M.; Leskelä, M. *Chem. Mater.* **2017**, *29*, 6502-6510.

80. Hagen, D. J.; Connolly, J.; Povey, I. M.; Rushworth, S.; Pemble, M. E. *Adv. Mater. Interfaces* **2017**, *4*, 1700274.

81. ThoughtCo. Table of electrical resistivity and conductivity, flow of current through materials by Anne Marie Helmenstine, https://www.thoughtco.com/table-of-electrical-resistivity-conductivity608499. (accessed Mar. 4, 2020).

82. Manepalli, R.; Stepniak, F.; Bidstrup-Allen, S. A.; Kohl, P. A. *IEEE Trans. Adv. Pack.* **1999**, *22*, 4-8.

83. Gall, D. *J. App. Phys.* **2016**, *119*, 085101.

84. Hauder, M.; Gstöttner, J.; Hansch, W.; Schmitt-Landsiedel, D. *Appl. Phys. Lett.* **2001**, *78*, 838-840.

85. Gao, L.; Härter, P.; Linsmeier, C.; Wiltner, A.; Emling, R.; Schmitt-Landsiedel, D. *Microelectron. Eng.* **2005**, *82*, 296-300.

86. Burda, C.; Chen, X.; Narayanan, R.; El-Sayed, M. A. *Chem. Rev.* **2005**, *105*, 1025-1102.

87. Ozbay, E. *Science* **2006**, *311*, 189-193.

88. Jeanmaire, D. L.; Van Duyne, R. P. *J. Electroanal. Chem. Interfacial Electrochem.* **1977**, *84*, 1-20.

89. Whitney, A. V.; Elam, J. W.; Zou, S.; Zinovev, A. V.; Stair, P. C.; Schatz, G. C.; Van Duyne, R. P. *J. Phys. Chem. B* **2005**, *109*, 20522-20528.

90. Willets, K. A.; Van Duyne, R. P. *Annu. Rev. Phys. Chem.* **2007**, *58*, 267-297.

91. Butler, M. A.; Ricco, A. J. *Appl. Phys. Lett.* **1988**, *53*, 1471-1473.

92. Huang, X.; El-Sayed, M. A. *J. Adv. Res.* **2010**, *1*, 13-28.

93. Weber, M. J.; Mackus, A. J. M.; Verheijen, M. A.; van der Marel, C.; Kessels, W. M. M. *Chem. Mater.* **2012**, *24*, 2973-2977.

94. Rumble, J. R. *Handbook of Chemistry and Physics;* CRS Press; FL: 2018.

95. Niskanen, A.; Hatanpää, T.; Arstila, K.; Leskelä, M.; Ritala, M. *Chem. Vap. Deposition* **2007**, *13*, 408-413.

96. Amusan, A. A.; Kalkofen, B.; Gargouri, H.; Wandel, K.; Pinnow, C.; Lisker, M.; Burte, E. P. *J. Vac. Sci. Technol. A* **2016**, *34*, 01A126.

97. Boysen, N.; Hasselmann, T.; Karle, S.; Rogalla, D.; Theirich, D.; Winter, M.; Riedl, T.; Devi, A. *Angew. Chem. Int. Ed.* **2018**, *57*, 16224-16227.

98. Chalker, P. R.; Romani, S.; Marshall, P. A.; Rosseinsky, M. J.; Rushworth, S.; Williams, P. A. *Nanotechnology* **2010**, *21*, 405602.

99. Masango, S. S.; Peng, L.; Marks, L. D.; Van Duyne, R. P.; Stair, P. C. *J. Phys. Chem. C* **2014**, *118*, 17655-17661.

100. Golrokhi, Z.; Chalker, S.; Sutcliffe, C. J.; Potter, R. J. *Appl. Surf. Sci.* **2016**, *364*, 789-797.

101. Golrokhi, Z.; Marshall, P. A.; Romani, S.; Rushworth, S.; Chalker, P. R.; Potter, R. J. *Appl. Surf. Sci.* **2017**, *399*, 123-131.

102. Mäkelä, M.; Hatanpää, T.; Mizohata, K.; Meinander, K.; Niinistö, J.; Räisänen, J.; Ritala, M.; Leskelä, M. *Chem. Mater.* **2017**, 2040-2045.

103. Baum, T. H.; Jones, C. R. *Appl. Phys. Lett.* **1985**, *47*, 538-540.

104. Messelhäuser, J.; Flint, E. B.; Suhr, H. *Appl. Phys. A* **1992**, *55*, 196-202.

105. Banaszak Holl, M. M.; Seidler, P. F.; Kowalczyk, S. P.; McFeely, F. R. *Inorg. Chem.* **1994**, *33*, 510-517.

106. Hampden-Smith, M. J.; Kodas, T. T. *Chem. Vap. Deposition* **1995**, *1*, 8-23.

107. Bessonov, A. A.; Morozova, N. B.; Gelfond, N. V.; Semyannikov, P. P.; Trubin, S. V.; Shevtsov, Y. V.; Shubin, Y. V.; Igumenov, I. K. *Surf. Coat. Technol.* **2007**, *201*, 9099-9103.

108. Griffiths, M. B. E.; Pallister, P. J.; Mandia, D. J.; Barry, S. T. *Chem. Mater.* **2016**, *28*, 44-46.

109. Mäkelä, M.; Hatanpää T; Mizohata, K.; Räisänen, J.; Ritala, M.; Leskelä, M. *Chem. Mater.* **2017**, *29*, 6130-6136.

110. Daele, M. V.; Griffiths, M. B. E.; Raza, A.; Minjauw, M. M.; Solano, E.; Feng, J.-Y.; Ramachandran, R. K.; Clemmen, S. P.; Baets, R.; Barry, S. T.; Detavernier, C.; Dendooven, J. *ACS Appl. Mater. Interfaces* **2019**, *11*, 37229-37238.

111. Holliday, R.; Goodman, P. *IEEE Rev.* **2002**, *48*, 15−19.

112. Caldwell, J. D.; Glembocki, O. J.; Bezares, F. J.; Kariniemi, M. I.; Niinistö, J. T.; Hatanpää, T. T.; Rendell, R. W.; Ukaegbu, M.; Ritala, M. K.; Prokes, S. M. *Opt. Express* **2011**, *19*, 26056-26064.

113. Mäkelä, M.; Hatanpää, T.; Ritala, M.; Leskelä, M.; Mizohata, K.; Meinander, K.; Räisänen, J. *J. Vac. Sci. Technol. A* **2017**, *35*, 01B112.

114. Greenwood, N. N.; Earnshaw, A. *Chemistry of the Elements;* 2nd ed.; Reed Educational and Professional Publishing Ltd: MA, 1997.

115. Chi, Y.; Lay, E.; Chou, T. Y.; Song, Y. H.; Carty, A. J. *Chem. Vap. Deposition* **2005**, *11*, 206-212.

116. Im, H.; Lindquist, N. C.; Lesuffleur, A.; Oh, S.-H. *ACS Nano* **2010**, *4*, 947-954.

117. Cleveland, E. R.; Glembocki, O.; Prokes, S. M. In *Plasma enhanced atomic layer deposition of silver thin films for applications in plasmonics and surface enhanced Raman scattering*, Proc. SPIE 8467 Nanoepitaxy: Materials and Devices IV, International Society for Optics and Photonics: 2012; p 84670H.

118. Barnes, W. L.; Dereux, A.; Ebbesen, T. W. *Nature* **2003**, *424*, 824-830.

119. Prokes, S. M.; Glembocki, O. J.; Rendell, R. W.; Ancona, M. G. *Appl. Phys. Lett.* **2007**, *90*, 093105.

120. Prokes, S. M.; Alexson, D. A.; Glembocki, O. J.; Park, H. D.; Rendell, R. W. *Appl. Phys. Lett.* **2009**, *94*, 093105.

121. De Vries, J. W. C. *Thin Solid Films* **1988**, *167*, 25-32.

122. Liu, H.; Wang, B.; Leong, E. S. P.; Yang, P.; Zong, Y.; Si, G.; Teng, J.; Maier, S. A. *ACS Nano* **2010**, *4*, 3139-3146.

123. Serghini-Monim, S.; Yuan, Z.; Griffiths, K.; Norton, P. R.; Puddephatt, R. J. *J. Phys. Chem.* **1995**, *99*, 9230-9235.

124. Yuan, Z.; Dryden, N. H.; Vittal, J. J.; Puddephatt, R. J. *Chem. Mater.* **1995**, *7*, 1696-1702.

125. Gao, L.; Härter, P.; Linsmeier, C.; Gstöttner, J.; Emling, R.; Schmitt-Landsiedel, D. *Mater. Sci. Semicond. Process.* **2004**, *7*, 331-335.

126. Chi, K. M.; Lu, Y. H. *Chem. Vap. Deposition* **2001**, *7*, 117-120.

127. Zanotto, L.; Benetollo, F.; Natali, M.; Rossetto, G.; Zanella, P.; Kaciulis, S.; Mezzi, A. *Chem. Vap. Deposition* **2004**, *10*, 207-213.

128. Piszczek, P.; Szłyk, E.; Chaberski, M.; Taeschner, C.; Leonhardt, A.; Bała, W.; Bartkiewicz, K. *Chem. Vap. Deposition* **2005**, *11*, 53-59.

129. Bahlawane, N.; Premkumar, P. A.; Brechling, A.; Reiss, G.; Kohse-Hoeinghaus, K. *Chem. Vap. Deposition* **2007**, *13*, 401-407.

130. Dryden, N. H.; Vittal, J. J.; Puddephatt, R. J. *Chem. Mater.* **1993**, *5*, 765-766.

131. Yuan, Z.; Dryden, N. H.; Li, X.; Vittal, J. J.; Puddephatt, R. J. *J. Mater. Chem.* **1995**, *5*, 303-307.

132. Edwards, D. A.; Harker, R. M.; Mahon, M. F.; Molloy, K. C. *J. Mater.Chem* **1999**, *9*, 1771-1780.

133. Szłyk, E.; Piszczek, P.; Łakomska, I.; Grodzicki, A.; Szatkowski, J.; Błaszczyk, T. *Chem. Vap. Deposition* **2000**, *6*, 105-108.

134. Edwards, D. A.; Harker, R. M.; Mahon, M. F.; Molloy, K. C. *Inorg. Chim. Acta* **2002**, *328*, 134-146.

135. Edwards, D. A.; Mahon, M. F.; Molloy, K. C.; Ogrodnik, V. *Inorg. Chim. Acta* **2003**, *349*, 37-44.

136. Edwards, D. A.; Mahon, M. F.; Molloy, K. C.; Ogrodnik, V. *J. Mater. Chem.* **2003**, *13*, 563-570.

137. Haase, T.; Kohse-Höinghaus, K.; Atakan, B.; Schmidt, H.; Lang, H. *Chem. Vap. Deposition* **2003**, *9*, 144-148.

138. Schmidt, H.; Shen, Y.; Leschke, M.; Haase, T.; Kohse-Höinghaus, K.; Lang, H. *J. Organomet. Chem.* **2003**, *669*, 25-31.

139. Chi, Y.; Yu, H.-L.; Ching, W.-L.; Liu, C.-S.; Chen, Y.-L.; Chou, T.-Y.; Peng, S.-M.; Lee, G.-H. *J. Mater. Chem.* **2002**, *12*, 1363-1369.

140. Song, Y. H.; Chen, Y. L.; Chi, Y.; Liu, C. S.; Ching, W. L.; Kai, J. J.; Chen, R. S.; Huang, Y. S.; Carty, A. J. *Chem. Vap. Deposition* **2003**, *9*, 162-169.

141. Dias, H. V. R.; Polach, S. A.; Wang, Z. *J. Fluorine Chem.* **2000**, *103*, 163-169.

142. Dias, H. V. R.; Gamage, C. S. P.; Keltner, J.; Diyabalanage, H. V. K.; Omari, I.; Eyobo, Y.; Dias, N. R.; Roehr, N.; McKinney, L.; Poth, T. *Inorg. Chem.* **2007**, *46*, 2979-2987.

143. Garcia, M. A.; Garcia-Heras, M.; Cano, E.; Bastidas, J. M.; Villegas, M. A.; Montero, E.; Llopis, J.; Sada, C.; De Marchi, G.; Battaglin, G.; Mazzoldi, P. *J. Appl. Phys.* **2004**, *96*, 3737-3741.

144. Sheng, J. *Int. J. Hydrogen Energy* **2009**, *34*, 2471-2474.

145. Durucan, C.; Akkopru, B. *J. Biomed. Mater. Res. Part B* **2010**, *93*, 448-458.

146. Lai, Y.; Zhuang, H.; Xie, K.; Gong, D.; Tang, Y.; Sun, L.; Lin, C.; Chen, Z. *New J. Chem.* **2010**, *34*, 1335-1340.

147. Sumesh, E.; Bootharaju, M. S.; Pradeep, A. T. *J. Hazard. Mater.* **2011**, *189*, 450-457.

148. Ferraris, M.; Ferraris, S.; Miola, M.; Perero, S.; Balagna, C.; Verne, E.; Gautier, G.; Manfredotti, C.; Battiato, A.; Vittone, E.; Speranza, G.; Bogdanovic, I. *J. Nanopart. Res.* **2012**, *14*, 1287.

149. Kang, J.-G.; Sohn, Y. *J. Mater. Sci.* **2012**, *47*, 824-832.

150. Kumar, P.; Mathpal, M. C.; Tripathi, A. K.; Prakash, J.; Agarwal, A.; Ahmad, M. M.; Swart, H. C. *Phys. Chem. Chem. Phys.* **2015**, *17*, 8596-8603.

151. Mathpal, M. C.; Kumar, P.; Kumar, S.; Tripathi, A. K.; Singh, M. K.; Prakash, J.; Agarwal, A. *RSC Adv.* **2015**, *5*, 12555-12562.

152. Ingo, G. M.; Riccucci, C.; Pascucci, M.; Messina, E.; Giuliani, C.; Fierro, G.; Di Carlo, G. *Appl. Surf. Sci.* **2018**, *446*, 279-286.

153. Lopez-Salido, I.; Lim, D. C.; Kim, Y. D. *Surf. Sci.* **2005**, *588*, 6-18.

154. Prieto, P.; Nistor, V.; Nouneh, K.; Oyama, M.; Abd-Lefdil, M.; Díaz, R. *Appl. Surf. Sci.* **2012**, *258*, 8807-8813.

155. Bastidas, D. M.; Cano, E.; González, A. G.; Fajardo, S.; Lleras-Pérez, R.; Campo-Montero, E.; Belzunce-Varela, F. J.; Bastidas, J. M. *Corros. Sci.* **2008**, *50*, 1785-1788.

156. Nohira, H.; Tsai, W.; Besling, W.; Young, E.; Pétry, J.; Conard, T.; Vandervorst, W.; De Gendt, S.; Heyns, M.; Maes, J. *J. Non-Cryst. Solids* **2002**, *303*, 83-87.

157. Shchukarev, A. V.; Korolkov, D. V. *Cent. Eur. J. Chem.* **2004**, *2*, 347-362.

158. Yamada, S.; Ishida, T.; Nogami, T. *Dalton Trans.* **2004**, 898-903.

159. Dodge, M. W.; Wacholtz, W. F.; Mague, J. T. *J. Chem. Crystallogr.* **2005**, *35*, 5-12.

160. Kishimura, A.; Yamashita, T.; Aida, T. *J. Am. Chem. Soc.* **2005**, *127*, 179-183.

161. Dias, H. R.; Diyabalanage, H. V. *Polyhedron* **2006**, *25*, 1655-1661.

162. Yang, G.; Raptis, R. G. *Inorg. Chim. Acta.* **2007**, *360*, 2503-2506.

163. Schmidbaur, H.; Schier, A. *Angew. Chem. Int. Ed.* **2015**, *54*, 746-784.

164. Jansen, M. *Angew. Chem. Int. Ed. Engl.* **1987**, *26*, 1098-1110.

165. Bondi, A. V. *J. Phys. Chem.* **1964**, *68*, 441-451.

166. Bourissou, D.; Guerret, O.; Gabbai, F. P.; Bertrand, G. *Chem. Rev.* **2000**, *100*, 39-92.

167. Herrmann, W. A. *Angew. Chem. Int. Ed.* **2002**, *41*, 1290-1309.

168. Khramov, D. M.; Lynch, V. M.; Bielawski, C. W. *Organometallics* **2007**, *26*, 6042-6049.

169. Herrmann, W. A.; Koecher, C. *Angew. Chem. Int. Ed.* **1997**, *36*, 2162-2187.

170. Tomioka, H. *Acc. Chem. Res.* **1997**, *30*, 315-321.

171. Hermann, W.; Weskamp, T.; Bohm, V. P. *Advances in Organometallic Chemistry;* Academic Press: CA, 2001; pp 1-71.

172. Garrison, J. C.; Youngs, W. J. *Chem. Rev.* **2005**, *105*, 3978-4008.

173. Nemcsok, D.; Wichmann, K.; Frenking, G. *Organometallics* **2004**, *23*, 3640-3646.

174. Jazzar, R.; Soleilhavoup, M.; Bertrand, G. *Chem. Rev.* **2020**.

175. Arduengo III, A. J.; Dias, H. V. R.; Calabrese, J. C.; Davidson, F. *Organometallics* **1993**, *12*, 3405-3409.

176. Zhou, Y.; Chen, W. *Organometallics* **2007**, *26*, 2742-2746.

177. Zhou, Y.; Zhang, X.; Chen, W.; Qiu, H. *J. Organomet. Chem.* **2008**, *693*, 205-215.

178. Resch, S. G.; Dechert, S.; Meyer, F. *Z. Anorg. Allg. Chem.* **2019**, *645*, 605-612.

179. Coyle, J. P.; Sirianni, E. R.; Korobkov, I.; Yap, G. P. A.; Dey, G.; Barry, S. T. *Organometallics* **2017**, *36*, 2800-2810.

180. Kuhn, N.; Kratz, T. *Synthesis* **1993**, *6*, 561-562.

181. Arentsen, K.; Caddick, S.; Cloke, F. G. N. *Tetrahedron* **2005**, *61*, 9710-9715.

182. Wang, H. M. J.; Lin, I. J. B. *Organometallics* **1998**, *17*, 972-975.

183. Chung, M.-C. *Bull. Korean Chem. Soc.* **2002**, *23*, 921-923.

184. Hu, X.; Castro-Rodriguez, I.; Olsen, K.; Meyer, K. *Organometallics* **2004**, *23*, 755-764.

185. Tapu, D.; Dixon, D. A.; Roe, C. *Chem. Rev.* **2009**, *109*, 3385-3407.

186. Garner, M. E.; Niu, W.; Chen, X.; Ghiviriga, I.; Abboud, K. A.; Tan, W.; Veige, A. S. *Dalton Trans.* **2015**, *44*, 1914-1923.

187. Mantina, M.; Chamberlin, A. C.; Valero, R.; Cramer, C. J.; Truhlar, D. G. *J. Phys. Chem. A* **2009**, *113*, 5806-5812.

188. Pinter, B.; Broeckaert, L.; Turek, J.; Růžička, A.; De Proft, F. *Chem. Eur. J.* **2014**, *20*, 734-744.

189. Liu, B.; Liu, B.; Zhou, Y.; Chen, W. *Organometallics* **2010**, *29*, 1457-1464.

190. De Fremont, P.; Scott, N. M.; Stevens, E. D.; Ramnial, T.; Lightbody, O. C.; Macdonald, C. L.; Clyburne, J. A.; Abernethy, C. D.; Nolan, S. P. *Organometallics* **2005**, *24*, 6301-6309.

191. Okayama, T.; Watanabe, T.; Hatayama, Y.; Ishihara, S.; Yamaguchi, Y. *Inorg. Chim. Acta* **2016**, *448*, 1-6.

192. Ardizzoia, G. A.; La Monica, G.; Maspero, A.; Moret, M.; Masciocchi, N. *Inorg. Chem.* **1997**, *36*, 2321-2328.

193. Omary, M. A.; Rawashdeh-Omary, M. A.; Diyabalanage, H. V.; Dias, H. R. *Inorg. Chem.* **2003**, *42*, 8612-8614.

194. Kandel, S.; Stenger-Smith, J.; Chakraborty, I.; Raptis, R. G. *Polyhedron* **2018**, *154*, 390-397.

195. Dias, H. R.; Diyabalanage, H.; Jayaratna, N. B.; Shaw, D.; Hettiarachchi, C. V.; Parasar, D. *Eur. J. Inorg. Chem.* **2019**, 3638-3644.

196. Titov, A. A.; Filippov, O. A.; Smol'yakov, A. F.; Baranova, K. F.; Titova, E. M.; Averin, A. A.; Shubina, E. S. *Eur. J. Inorg. Chem.* **2019**, 821-827.

197. Emashova, S. K.; Titov, A. A.; Filippov, O. A.; Smol'yakov, A. F.; Titova, E. M.; Epstein, L. M.; Shubina, E. S. *Eur. J. Inorg. Chem.* **2019**, 4855-4861.

198. Maspero, A.; Giovenzana, G. B.; Monticelli, D.; Tagliapietra, S.; Palmisano, G.; Penoni, A. *J. Fluorine Chem.* **2012**, *139*, 53-57.

199. Zelenin, K. N.; Tugusheva, A. R.; Yakimovich, S. I.; Alekseev, V. V.; Zerova, E. V. *Chem. Heterocycl. Compd.* **2002**, *38*, 668-676.

200. Xu, C.; Corbitt, T. S.; Hampden-Smith, M. J.; Kodas, T. T.; Duesler, E. N. *J. Chem. Soc., Dalton Trans.* **1994**, 2841-2849.

201. Evans, W. J.; Giarikos, D. G.; Josell, D.; Ziller, J. W. *Inorg. Chem.* **2003**, *42*, 8255-8261.

202. Welch, J. T.; Ngo, S. C.; Banger, K. K. Silver precursors for CVD processes. U. S. patent 6, 613, 924 B1, September 2, 2003.

203. Wang, Y.; Xie, Y.; Threlkeld, H. L.; Wei, P.; Schaefer III, H. F.; Robinson, G. H. *Organometallics* **2019**, *38*, 4578-4584.

204. Bischoff, I. A.; Müller, C.; Huch, V.; Zimmer, M.; Schäfer, A. *Eur. J. Inorg. Chem.* **2019**, 1941−1944.

205. Jung, M. C.; Daejun-shi Organometallic Precursor for Forming Metal Pattern. Europen patent 1, 293, 508 A1, March 19, 2003.

206. Mäkelä, M. *Studies on Atomic Layer Deposition of Gold and Silver Thin Films*. University of Helsinki, 2018.

ABSTRACT
THERMAL ATOMIC LAYER DEPOSITION OF SILVER METAL FILMS: SYNTHESIS AND CHARACTERIZATION OF THERMALLY STABLE SILVER METAL PRECURSORS

by

HARSHANI JAYABAHU ARACHCHILAGE

August 2020

Advisor: Professor Charles H. Winter

Major: Chemistry (Inorganic)

Degree: Doctor of Philosophy

Traditional film deposition techniques such as PVD and CVD are widely used in the microelectronics industry. However, the lack of thickness control and conformality requirements limit these techniques for current and future applications. By contrast, ALD offers the deposition of ultra-thin conformal films with accurate thickness control due to the self-limiting growth behavior. Ag metal has the lowest resistivity (1.59 μΩ cm) of all metals and has applications in plasmonic devices. Growth by thermal atomic layer deposition (ALD) has been hampered by the low thermal stabilities of virtually all Ag precursors. The synthesis of highly thermally stable Ag metal precursors is very challenging due to the positive electrochemical potential of the Ag(I) ion. The focus of this dissertation is given to the development of thermal ALD processes using highly thermally stable precursors and synthesis and characterization of thermally stable silver precursors. Trimeric silver pyrazolates were synthesized and characterized. These precursors are highly thermally stable, volatile, and reactive towards several reducing agents, which are the key properties that ALD precursors should have. The deposition of the silver metal thin films was attempted using $[Ag(3,5\text{-}CF_3)_2Pz]_3$ and 1,1-dimethylhydrazine. Both the metal precursor and the reducing agent showed self-limited growth at 180 °C. Rather than a continuous film, silver

nanoparticle growth was observed on the SiO_2 substrate instead. New Ag pyrazolate and diketonate complexes were synthesized using saturated and unsaturated NHCs. Solid state structures of NHC-based Ag pyrazolates showed great diversity, including monomers, dimers, and a tetramer. Dimers have close Ag-Ag contacts, consistent with argentophilic interactions. These new Ag pyrazolate complexes are volatile between 110 and 140 °C at 0.2 Torr, and thermally decompose at temperatures between 160 and 293 °C. However, TGA traces and thermal decomposition temperatures suggest that trimers $[Ag(3,5\text{-}CF_3)pz]_3$ and $[Ag(3\text{-}tBu,5\text{-}CF_2CF_2CF_3)pz]_3$ still have better thermal stability than the NHC complexes. Most of the Ag(diketonate)(NHC) complexes are monomers with no close Ag-Ag contacts. The Ag diketonate complexes have volatilities that range from 100-124 °C at 0.2 Torr, and thermal decomposition temperatures that range from 141-188 °C. Carefully chosen anionic ligands with electron-withdrawing substituents are required to achieve the highest possible stabilities of the metal complex.

AUTOBIOGRAPHICAL STATEMENT

HARSHANI JAYABAHU ARACHCHILAGE

Education

Ph.D., Inorganic Chemistry, Wayne State University, Detroit, Michigan (2015-2020)
Advisor: Professor Charles H. Winter
M.S., Chemistry, Sam Houston State University, Huntsville, Texas (2013-2015)
Advisor: Professor Richard E. Norman
B.Sc., Chemistry Special, University of Kelaniya, Kelaniya, Sri Lanka (2005-2009)
Advisor: Professor Janitha A. Liyanage

Honors and Awards (selected)

Best Student Poster Award, 19th International Conference on Atomic Layer Deposition, 2019
Thomas C. Rumble University Graduate Fellowship, Wayne State University, 2019 - 2020
Outstanding Teaching Award, Wayne State University, 2018

Publications

1) **Arachchilage J. H.**; Suescun, L; Ward, C. L.; Winter, C. H. "Volatile and Thermally Stable Silver Pyrazolate Complexes Containing N-Heterocyclic Carbene Ligands"-*manuscript in preparation.*

2) **Arachchilage J. H.**; Ward, C. L.; Winter, C. H. "Synthesis and Characterization of Thermally Stable and Volatile N-Heterocyclic Carbene Silver Diketonate Precursors"-*manuscript in preparation.*

3) **Arachchilage J. H.**; Winter, C. H. "Thermal ALD Process to Deposit Silver Metal using Silver Pyrazolate Precursor and Dimethylhydrazine"-*manuscript in preparation.*